SANDIA REPORT

SAND2004-0555
Unlimited Release
Printed March 2004

Low Work Function Material Development for the Microminiature Thermionic Converter

Donald B. King, Kevin R. Zavadil, Dwight R. Jennison,
Corbett C. Battaile & Albert C. Marshall

Prepared by
Sandia National Laboratories
Albuquerque, New Mexico 87185 and Livermore, California 94550

Sandia is a multiprogram laboratory operated by Sandia Corporation,
a Lockheed Martin Company, for the United States Department of Energy's
National Nuclear Security Administration under Contract DE-AC04-94AL85000.

Issued by Sandia National Laboratories, operated for the United States Department of Energy by Sandia Corporation.

Available to DOE and DOE contractors from
U.S. Department of Energy
Office of Scientific and Technical Information
P.O. Box 62
Oak Ridge, TN 37831

Telephone: (865)576-8401
Facsimile: (865)576-5728
E-Mail: reports@adonis.osti.gov
Online ordering: http://www.doe.gov/bridge

Available to the public from
U.S. Department of Commerce
National Technical Information Service
5285 Port Royal Rd
Springfield, VA 22161

Telephone: (800)553-6847
Facsimile: (703)605-6900
E-Mail: orders@ntis.fedworld.gov
Online order: http://www.ntis.gov/help/ordermethods.asp?loc=7-4-0#online

SAND2004-0555
Unlimited Release
Printed March 2004

Low Work Function Material Development for the Microminiature Thermionic Converter

Donald B. King
Advanced Nuclear Concepts Department

Kevin R. Zavadil
Corrosion, Electrochemistry and Cleaning Department

Dwight R. Jennison
Surface & Interface Science Department

Corbett C. Battaile
Materials & Process Modeling & Computation Department

Albert C. Marshall
National Security Studies Department

Sandia National Laboratories
P.O. Box 5800
Albuquerque, New Mexico 87185-1136

Abstract

Thermionic energy conversion in a miniature format shows potential as a viable, high efficiency, micro to macro-scale power source. A microminiature thermionic converter (MTC) with inter-electrode spacings on the order of microns has been prototyped and evaluated at Sandia. The remaining enabling technology is the development of low work function materials and processes that can be integrated into these converters to increase power production at modest temperatures (800 – 1300 K). The electrode materials are not well understood and the electrode thermionic properties are highly sensitive to manufacturing processes. Advanced theoretical, modeling, and fabrication capabilities are required to achieve optimum performance for MTC diodes. This report describes the modeling and fabrication efforts performed to develop micro dispenser cathodes for use in the MTC.

Intentionally Left Blank

Acknowledgments

The authors would like to thank Drs. David P. Adams and J.A. Heidi Ruffner for the deposition of the modulated thin films. Acknowlegdment is extended to J.A. Tony Ohlhausen for the SIMS work, Bonnie McKenzie for the SEM and FIB work, and Wayne Buttry for the scanning Auger analysis.

Contents

Figures

Tables

1. Introduction

Thermionic conversion of thermal energy to electrical energy has been studied since the late nineteenth century, but practical devices were not demonstrated until the mid twentieth century. Edison (1884) first studied thermionic emission in 1883 but Schlicter (1915) did not propose its use for conversion of heat to electricity until 1915. Although analytical work on thermionic converters continued during the 1920s, experimental converters were not reported on until 1941. The Russians, Gurtovy and Kovalenko (1941), published data that demonstrated the use of a cesium vapor diode to convert heat into electrical energy. Practical thermionic conversion was demonstrated in 1957 by Hernqvist (1957) in which efficiencies of 5 to 10% were reached with power densities of 3 to 10 W/cm2. Modern thermionic converters have not improved in performance since the 1950s.

Figure 1 illustrates the components and processes of a typical thermionic converter. A heat source elevates the temperature of the emitter (typically, between 1500 - 2200 K). Electrons are then thermally emitted into the space (the interelectrode gap, IEG) between the emitter electrode and collector electrode. The electrodes are operated in a vacuum or low pressure vapor (a few torr). The collector electrode is cooled by a heat sink and kept at a low temperature relative to the collector. The electrons travel across the IEG toward the collector electrode and condense on the collector. The electrons then return to the emitter through the electrical leads and load that connect the collector to the emitter. The thermionic conversion efficiency is given by the ratio of the electrical energy output to the total heat input.
Thermionic conversion depends on emission of electrons from a hot surface. Valence electrons at room temperature within a metal are free to move within the atomic lattice, but very few can escape from the metal surface. The electrons are prevented from escaping by the electrostatic image force between the electron and the metal surface. The heat of the emitting surface gives the electrons sufficient energy to overcome the electrostatic image force. The energy required to leave the metal surface is referred to as the material work function, ϕ, expressed in electron volts (eV).

The current density, J, at which electrons leave the metal surface is given by the Richardson-Dushmann equation:

$$J = AT_E^2 \exp(-[\psi-\mu_E]/kT_E), \quad (1)$$

where A is the Richardson constant (in $A/m^2/K^2$), T_E is the emitter temperature (in K), k is the Boltzmann constant (in eV/K), μ_E is the emitter Fermi energy level (in eV), and ψ is the maximum energy (in eV) experienced by an electron in transit. Figure 2 illustrates the energy barrier levels that an electron must overcome as required by equation (1) in a two-electrode thermionic converter. Electrons leave the emitter surface and travel to the collector surface. Operating the collector at lower temperatures minimizes electron emission from the collector to emitter. The maximum motive force depends on (1) the sum of the emitter work function (ϕ_E) and the electron induced space charge, ΔV_{sc}, or (2) the sum of the diode operating voltage (V_d), the collector work function (ϕ_c), and ΔV_{sc}.

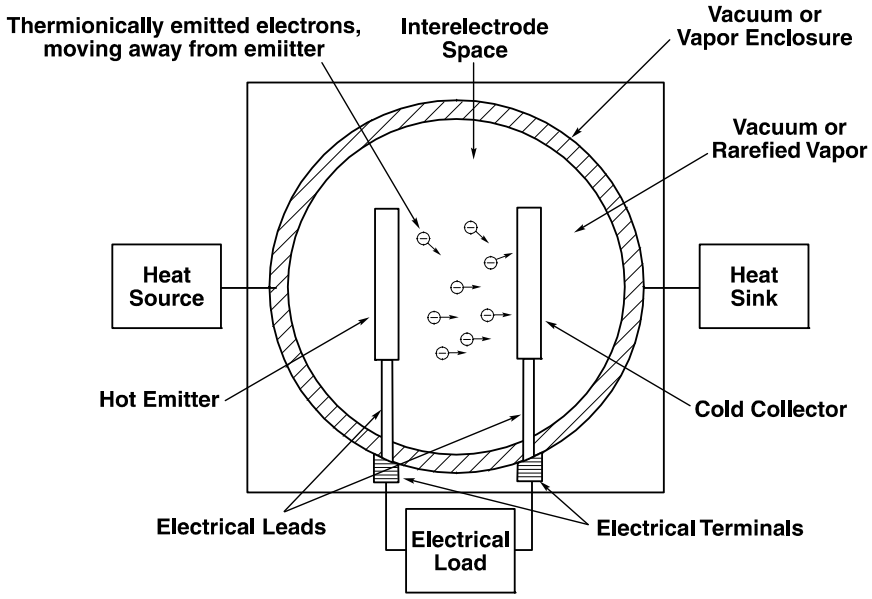

Figure 1. Thermionic Converter Elements and Processes (Hatsopoulos et al., 1979).

Large emission current densities are achieved by coating the emitter surface with a low work function material and operating that emitter at as high a temperature as possible. Very high temperature operation may cause any material to evaporate rapidly and limit emitter lifetime. Low work function materials can have relatively high evaporation rates and must be operated at lower temperatures. Materials with low evaporation rates usually have high work functions. Choosing the correct electrode coating is half the battle in designing thermionic converters. Once the electrons are successfully emitted, their continued travel to the collector must be ensured. Electrons emitted from the emitter produce a space charge (ΔV_{sc}) in the interelectrodegap (IEG). For large currents, the buildup of charge will act to repel further emission of electrons and limit the efficiency of the converter.

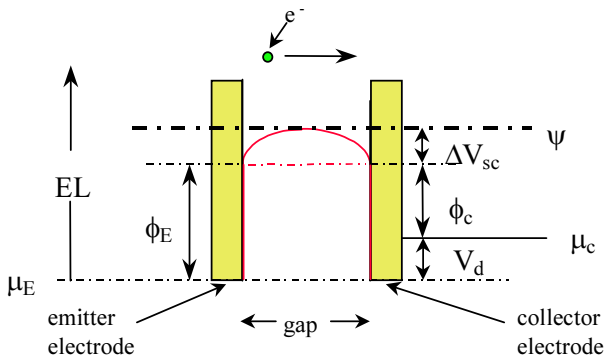

Figure 2. Energy Levels Experienced by Electrons During Transition.

Figure 3 illustrates the diode current-voltage characteristics (for a diode in which the emitter work function is greater than the collector work function). If no space charge existed, the ideal diode current density would increase linearly (in retarding mode) and then saturate at a diode

voltage equal to the difference of the emitter work function and collector work function. Since space charge does exist, the actual diode current is smaller than the ideal current; the point of departure from the ideal diode current is called the critical point. The Richardson-Dushmann equation does not consider the effect of high electric fields at the cathode. When an electric field of sufficient magnitude is applied to the cathode, emission current greater than the saturation current is observed (referred to as the saturation point). The electric field decreases the total energy barrier that the emitted electron experiences. This increase in current above the saturation value is referred to as the Schottky effect or mode. We must also note that diodes with emitter work functions less than the collector work functions will exhibit the same voltage-current characteristic but the current-voltage trace will occur to the left of the origin. The saturation current will begin at the diode voltage that corresponds to the difference of the emitter work function and collector work function.

Two options have been considered to limit space charge effects in the IEG: thermionic converters filled with ionized gas and thermionic converters with small IEG spacing. Cesium vapor is the gas most commonly used because of its low ionization energy (3.89 eV). Cesium has a dual role in thermionic converters: (1) space charge neutralization and (2) electrode work function modification. In the latter case, cesium atoms adsorb onto the emitter and collector surfaces. The adsorption of the atoms onto the electrode surfaces results in a decrease of the emitter and collector work functions, allowing greater electron emission from the hot emitter.

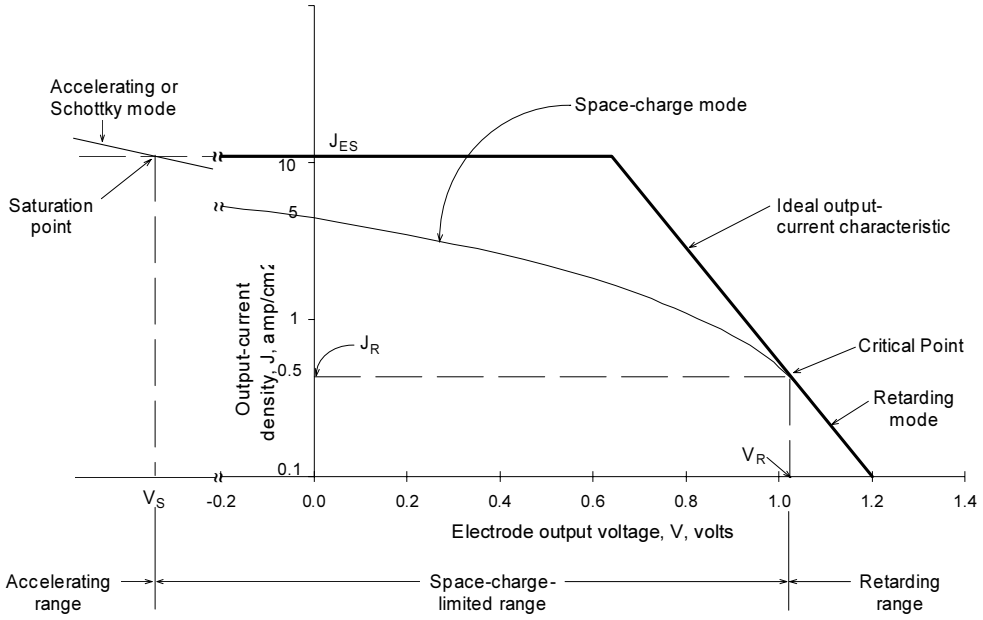

Figure 3. Diode Current-Voltage Characteristic.

Space charge neutralization occurs via two mechanisms: (1) surface ionization and (2) volumetric ionization. Surface ionization occurs when a cesium atom comes into thermal contact with the emitter. Volumetric ionization occurs when an emitted electron inelastically collides with a Cs atom (causing an electron loss from the atom's outer shell) in the IEG generating a positive ion with a substantially lower velocity than the electrons. In both cases, the ionized Cs neutralizes the local space charge. The work function and space charge minimization increases

the converter power output. However, at the cesium pressures necessary to substantially affect the electrode work functions, an excessive amount of collisions (more than that needed for ionization) occurs between the emitted electrons and cesium atoms, resulting in a loss of conversion efficiency. Therefore, the cesium vapor pressure must be controlled so that the work function reduction and space charge reduction effects outweigh the electron-cesium collision effect.

An example of an operational thermionic converter is found on the Russian TOPAZ-II space reactor. These converters operate at emitter temperatures of 1700 K and collector temperatures of 600 K with a cesium pressure in the IEG of just under one torr. Typical current densities achieved are < 4 A/cm^2 at output voltages of approximately 0.5 V. These converters operate at an efficiency of approximately 6%. The control of cesium pressure in the IEG is critical to operating these thermionic converters at their optimum efficiency.

1.1 MTC Description

The microminiature thermionic converter (MTC) diode is an innovative design using advanced thermionic electrode materials to convert heat into electricity. The current MTC prototype is a planar, two electrode vacuum diode. Commercial electronic integrated circuit (IC) fabrication techniques allow the MTC to be produced as one unit with micron sized electrode gap features (a micron sized gap between the electrodes plays a key role in obtaining higher energy conversion efficiencies). In addition, the IC fabrication technique would allow thousands of MTCs to be fabricated as one large conversion unit. This scale of fabrication may allow various MTC units to be fabricated with power outputs ranging from milliwatts to hundreds of watts and at very low cost. The use of variable work function thermionic electrodes (1 - 2 eV) would allow the creation of MTCs tailored to function efficiently for several heat sources and in low (550-1000 C) temperature regimes. In summary, the successful use of MTCs with small electrode spacing and variable electrode work functions would allow: 1) the conversion of heat energy to relatively large electrical power densities (up to 10s of W/cm^2) at relatively high conversion efficiencies (up to 25%), and 2) operation of converters tailored to function for the different heat sources and their temperature regimes. The heat required for this direct conversion process is fuel independent; any heat source (combustion, solar, advanced nuclear reactors, radioisotopes, waste heat) can be used. Possible applications include micro-robotics, space-based power, mobile and remote electrical power sources, and commercial power production.

Past work has successfully demonstrated a prototype MTC; however, performance has been less than predicted due to poor thermionic emission from unoptimized cathode materials (King 1999). The most critical element for MTC success is to develop high performance cathodes that are highly electron emissive. However, newly identified, potentially high performance electrode materials are not well understood and have never been used in a thermionic converter device. Advanced theoretical and modeling capabilities are required to achieve optimum performance for MTC diodes. The work reviewed in this report has attempted to advance the development of emitter materials through combined theoretical modeling and experimentation.

High performance electrodes must exhibit a low work function, ϕ, uniformly over the electrode surface. The electron source community has identified several promising materials that can

uniformly reduce ϕ through the use of surface adsorbates and/or bandgap modification. An example is the macro-scale dispenser cathode that uses a metal/ barium oxide matrix with a metal capping layer capable of producing a low work function at the surface. Cortenraad (1999) has shown that an O-Ba dipole chain is most likely responsible for surface work function lowering. Calculation by Müller (1997) and measurements by Zagwijn (1997) show that a minimum work function of 1.4 eV is possible for a O-Ba complex on tungsten. Gärtner (1997) has shown that a high field work function of 1.16 eV on a hybrid metal/oxide surface is possible. Despite demonstrating suitably low work functions for MTC applications, the required uniformity on the electrode surface has not been achieved; this nonuniformity results in degraded electron emission at the MTC operating conditions.

Historically, minimal combined theoretical/empirical effort has been applied to understanding how to achieve the optimum surface complex required for a low uniform work function. The principle problem is that no one to date has developed a Ba supply model that incorporates Ba transport through the film bulk to the surface, Ba surface diffusion and resulting surface complexes, and Ba desorption from the surface. Furthermore, the exact configuration and composition of surface complexes leading to stable low work function electrodes has not been established. We have developed a complete transport model for a thin film, mixed metal/oxide micro-dispenser cathode. In addition, we used these models to guide development of a micro-dispenser cathode. Our general approach could also be applicable to other promising low electron affinity (LEA) material systems, including metal semiconductor composites (MSC) and compositionally graded $Al_xGa_{1-x}N$ ($0<x<0.75$). For both the micro-dispenser oxides and alternative electrode materials, improvements suggested by the models could be fabricated into films and measured performance could be used to test our understanding and predictive capabilities. Successful completion of this work could result in high performance electrode materials suitable for thermionic energy conversion. Furthermore, the validated models and understanding achieved will represent in itself a major advance in thermionic conversion technology.

MTCs offer a simpler solution to thermionic energy conversion. A gas need not be introduced into the IEG to reduce the space charge effects resulting from the large current flow from the emitter to the collector. The small IEG size itself reduces the density of electrons in the gap (and their resulting current-limiting space charge). Historically, the close-spaced converter has been difficult to manufacture for large-scale operation due to the close tolerances (several microns or even submicron interelectrode gap size) needed for efficient operation. Large-scale production and operation of these close-spaced converters is now possible using integrated circuit (IC) fabrication techniques. Spacing on the order of 0.25 to 1 micron can now be produced and maintained over relatively large emission areas.

Planar microminiature thermionic diodes are fabricated using conventional IC fabrication techniques. All elements of the diode (emitter, collector, and insulating spacer between the electrodes) are made with standard sputter and chemical vapor deposition (CVD) techniques and etch techniques used by the semiconductor industry. The CVD techniques allow us to reliably, reproducibly, and accurately grow extremely thin layers of metals (for the electrodes) and oxides (for the spacers). An overview of the fabrication and assembly sequence of the first prototype vacuum thermionic converter is illustrated in Figure 4. The prototype is fabricated

from two insulating substrates as shown in Figure 4a. The substrates may have different thicknesses and may be different materials. For the prototype, the emitter substrate is a circular sapphire substrate with a 25 mm diameter and a 1 mm thickness. The collector is made of quartz with a thickness of 5 mm and a cross sectional area of approximately 12 mm by 7 mm.

The gap depth will be formed in the collector substrate and will form a trough running the length of the shorter cross sectional dimension mentioned above. The gap depth is shown in Figure 4b. The total depth must accommodate the thicknesses of the emitter and collector electrodes as well as any thermal expansion at operational temperatures.

The emitter and collector metal electrodes and bond pads are then deposited onto the surfaces of each wafer, as shown in Figure 4c. Figure 5 presents a picture of the sapphire wafer with metal electrodes and bond pads. The I-beam shaped structure is the emitter electrode metal base. The squares on either side of the I-beam are the collector bond pads. The collector electrode metal is deposited over the entire trough of the collector wafer, as shown in Figure 6. Small wing tabs extend from the trough onto the shoulders of the collector wafer and form the electrical connection to the collector bond pads on the emitter wafer.

The low work function barium-calcium-strontium tricarbonate material is then deposited onto the metal electrode bases of the emitter and collector as shown in Figure 4d. Figure 7 illustrates the tricarbonate material as deposited on the emitter metal electrode surface.

The prototype diode is typically heated by thermal radiative energy supplied by external heaters to the wafer backside. However, electrical heaters can also be integrated into the prototype converter diode to heat the emitter structure by thermal conduction from resistive heating. An integrated heater deposited onto the backside of the sapphire emitter wafer is shown in Figure 8.

The prototype thermionic converter diode fabrication and assembly is completed by bonding the collector wafer to the emitter wafer. Figure 9 illustrates an assembled prototype thermionic converter diode.

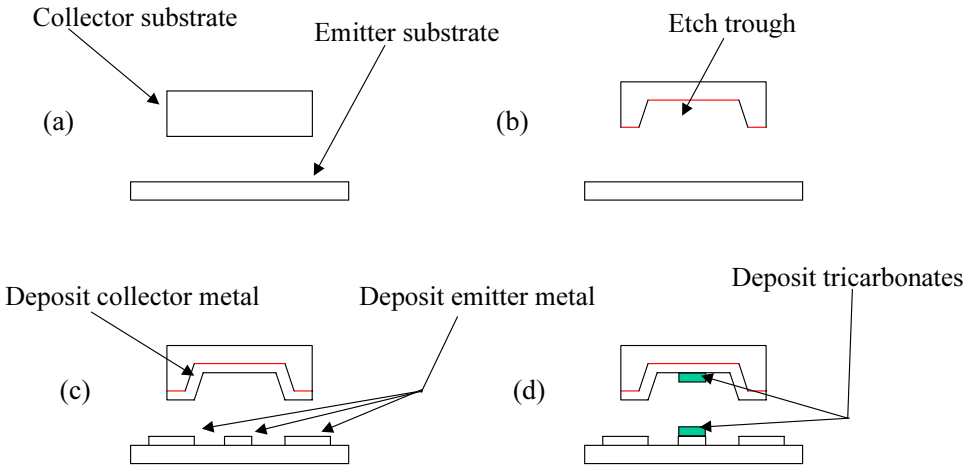

Figure 4. Overview of prototype thermionic converter fabrication sequence

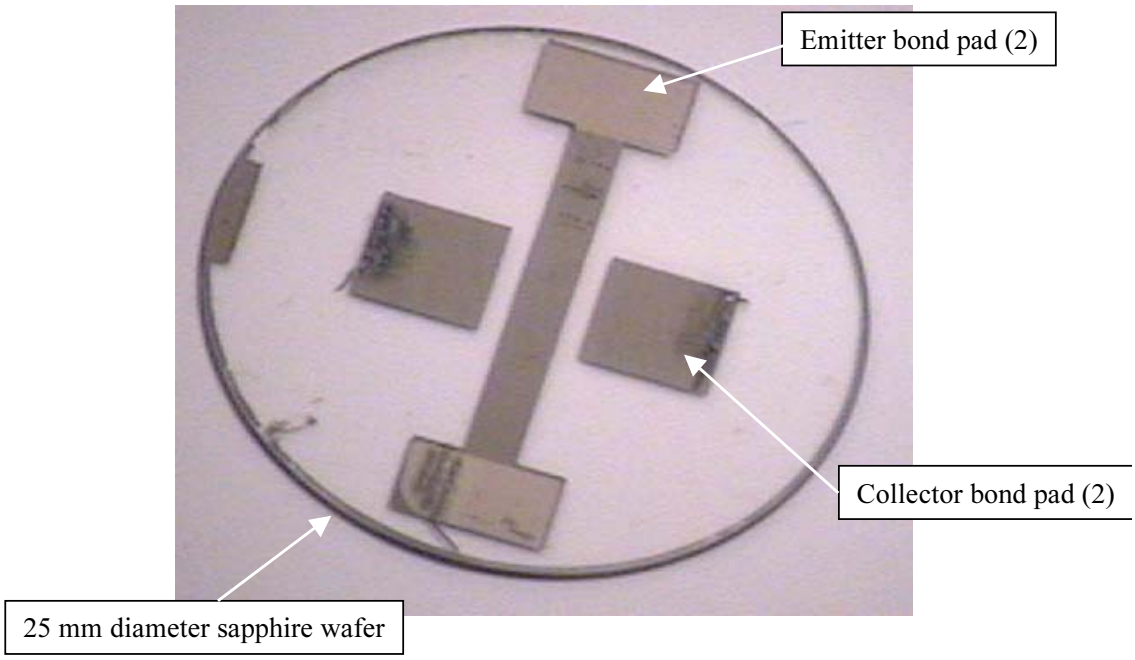

Figure 5. Emitter wafer with deposited metal electrodes and bond pads.

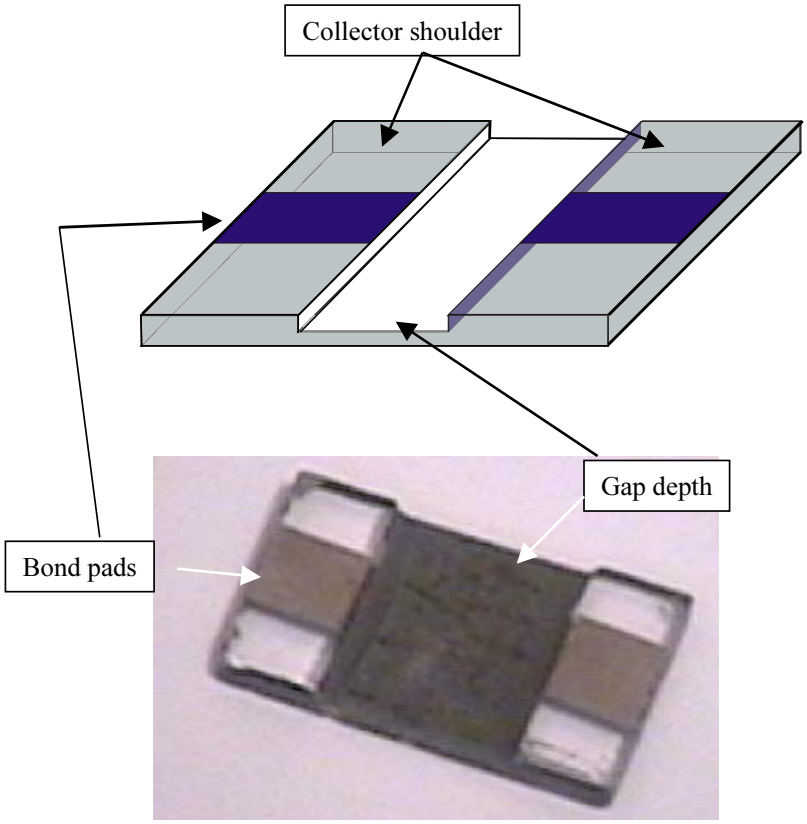

Figure 6. Collector wafer with etched trough that forms the gap depth. The collector electrode metal is deposited in the trough, and the bond pads are deposited on the collector shoulders.

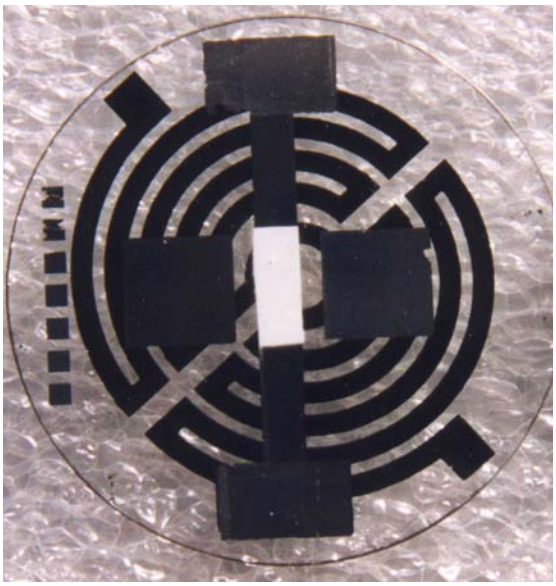

Figure 7. Low work function material deposited onto emitter metal electrode.

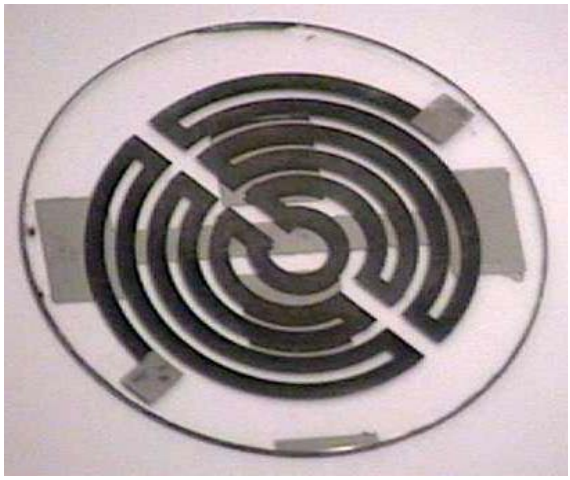

Figure 8. Integrated back-side emitter wafer heater.

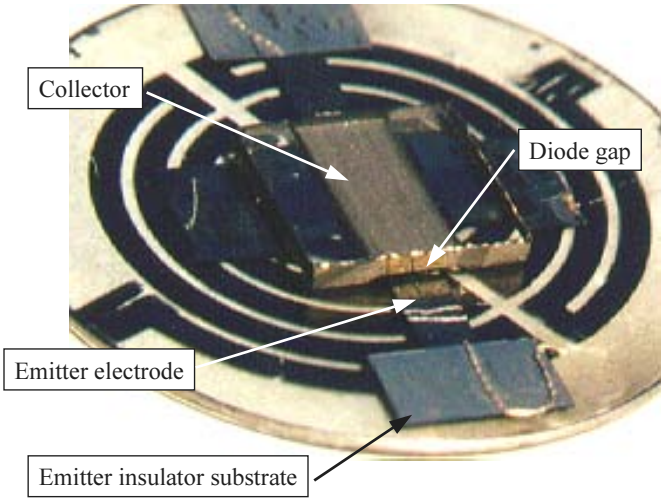

Figure 9. Assembled prototype thermionic converter diode.

1.2 Project plan.

The focus of this work has been the development of improved understanding of low work function materials to enable the fabrication of advanced thermionic emitter materials. Preliminary models were developed to understand the mechanisms that generate a uniform and low work function across the emitter surface. Based on the mechanisms suggested by the models, advanced films were fabricated. Experiments were conducted to measure work function and Ba distribution. Experimental results were incorporated into upgraded models. The models and tests were also used to confirm the advanced theory concepts of diode operation such as space charge, patch effects, and electron reflection.

1.2.1 Application of Local Structure and Percolation Theory

Little is known concerning the local electronic structure and other properties of alkaline-earth oxide surfaces and the interfaces of oxide films and metals. Stress, due to the surface and/or a lattice mismatch, may play a substantial role in structure determination and must be understood. We conducted first principles density functional calculations on candidate oxide surfaces to obtain bandgap, structure, and work function information. Comparisons were made with known oxides to determine the source of low work functions. These results guided film fabrication and evaluation efforts. The role of excess Ba was studied both in the bulk oxide and at its surface. Our goal was to develop a model that will aid in predicting surface morphology evolution within a candidate oxide system. Percolation theory was applied to determine the net rate of Ba transport to the surface. Experimental determination of void structure in these films was used as input for these calculations. Monte Carlo calculations were conducted to determine net flux to the surface taking into consideration the diffusion of Ba along internal void surfaces and through remnant grain boundaries in the bulk film.

1.2.2 Tailored Film Fabrication

The key to optimizing an oxide cathode is controlling the surface adsorbate concentration and the resulting complexes that form. Control can be established by incorporating chemistry in the oxide responsible for adsorbate (i.e., Ba) supply, structure in the bulk oxide for adsorbate transport, and a surface structure that favors lateral adsorbate transport and suitable complex lifetimes. We worked with modelers in Organizations 1100 and 1800 to deposit tailored oxide films with this level of control functionality incorporated. Tailored oxide films were deposited using rf sputtering because of the flexibility in generating multi-component films. Initial candidate films included compositionally modulated structures of a transition metal and a barium-containing oxide. Heating such a film produces metal coalescence, barium reduction and eventual Ba transport to the surface (Zavadil 1999). These films preserve their surface structure within given thermal limits and can be capped using a selective metal or oxide that supports Ba diffusion and minimizes desorption. Density functional theory calculations were used to direct surface termination choices. Bulk film constituents were selected based on thermally generated film porosity and free Ba production. Monte Carlo theory was applied to resulting film structures to identify optimum bulk structure for bulk Ba transport. Film constituent and deposition conditions (substrate temperature, plasma energy, etc.) were varied to achieve the target

structures. We utilized this interplay between computation and experimentation to identify film strategies.

1.2.3 Application of Advanced Theory

Advanced thermionic theory (Marshall 1998) was applied to improve the interpretation of Schottky emission data. The first stage focused on local variation in surface potential or "patch effects" to determine the extent of ϕ uniformity. A model was developed to take into account how patch effects impact emission density. Inclusion of patch effects provides a better estimate of both work function and transmission coefficient. In turn, these better estimates can be used to guide film fabrication and local electronic structure calculations at the system level. The second stage determined how patch effects impact electron reflection at the emitter surface. The new theory allowed reflection effects to be included as transmission coefficients. Transmission coefficients can be calculated by determining electron scattering kernels and energy distributions within the emitting material. Electron reflection leads to a longer residence time of electrons within the gap and increases the space charge effect in the gap. The space charge affects the maximum electrical potential as well as local potentials near the surface. The third stage of theory application used calculated reflection coefficients, temperature dependent work functions and space charge fields to determine net diode system current.

1.2.4 Emission Property Characterization

Structure/property relationships were established by investigating film emission properties. Work function and Richardson constant values were measured for input to the new theory. We measured field-dependent current density at variable temperature and extracted work function and transmission coefficient values.

2. Emitter Materials Development and Fabrication

In this chapter of the report, we discuss the lessons learned in our attempts to develop low work function thermionic cathodes for micro-thermionic converter applications. Our focus has been placed almost exclusively on thin film concepts that can be integrated into devices fabricated using conventional semiconductor wafer-level processes. Emphasis was placed at an early stage on a micro-dispenser type cathode that mimics the commercial electron source sector's macroscopic dispenser cathode. What we have learned from our efforts and what is demonstrated in this section of the report is that where it is possible to generate a moderate operating temperature dispenser film, key technical challenges remain to be overcome. Specifically, we will show that these films are susceptible to surface contamination effects, capacity losses, and thermal/time evolving microstructural changes all of which limit the utility of these films. With the exception of emission capacity, these limitations are no different than what are faced with conventional dispenser-style sources.

2.1 Commercial Dispenser Cathode Properties

Current commercial dispenser cathodes are all based on the design of a porous tungsten body (or pellet) that is impregnated with a Ba-based multi-component oxide (Beck 1958, Thomas 1990, Gärtner 1997). Surface layers are often sputtered deposited onto the impregnated and machined surface of the dispenser body to tailor the emission properties for specific temperature ranges, environments and applications (see Figure 10). The composition of the impregnate oxide is also varied to meet specific emission requirements, but the basic composition is essentially a ternary oxide that contains BaO, CaO and Al_2O_3 in varying proportions. The phase diagrams for this family have been published and preferred compositions coincide with near eutectic compositions of the aluminates. Favored compositions tend to be 4:1:1 and 5:3:2 $BaO:CaO:Al_2O_3$, although other compositions are used. The basic thermochemistry that results when the impregnated body is heated has been the subject of a number of studies (for example, see Magnus 1997). Tungsten is known to reduce both BaO and CaO to form the free alkaline earth metal species (reduced product) and an alkaline earth tungstate phase (oxidized product). This redox (reduction/oxidation) chemistry at elevated temperature becomes the route for supplying Ba and O to the outer metal surface. It is the combination of these two ionizable species that results in the development of a surface dipole that lowers the effective surface work function or the barrier for electron emission into vacuum (Muller 1997, Zagwijn 1997). The efficiency of thermionic emission is directly related to this work function, as well as other surface properties (Herring 1949). The data of Figure 10 provide some guidelines for target material systems where practical low work function values are achievable (Cattelino 1997).

An idea of a target film microstructure comes from characterization of a commercial electron source heated to operational temperatures. Figure 11 shows a series of electron and ion images generated on an electron microscope in both plan and cross-section views of a Type M cathode (HeatWave Labs Inc, Watsonville, CA) heated to 1240 K for a cumulative period of 16 hours. This temperature and time combination was sufficient to activate the cathode producing electron emission of 10 $mA \cdot cm^{-2}$ at an accelerating field of 10^5 $V \cdot m^{-1}$. The sputter deposited 0.3 μm thick Os/Ru overcoat is apparent in the secondary electron, cross-sectional image of Figure 11a. This

coating shows the remnant columnar grain structure typical of sputtered deposits in this thickness range. The coating also possesses a distribution of voids both at the sputter alloy – tungsten interface and along the vertical grain boundaries in the deposit. The source of these voids appears to be the alloying reaction and differences in diffusivity of Os and Ru (Kirkendall voiding). These voids create a porous matrix through which Ba and O would be expected to diffusively transport. A high areal density of these voids would then act essentially as a dispersion matrix for the lateral surface diffusion of Ba and O onto the emitting alloy surface.

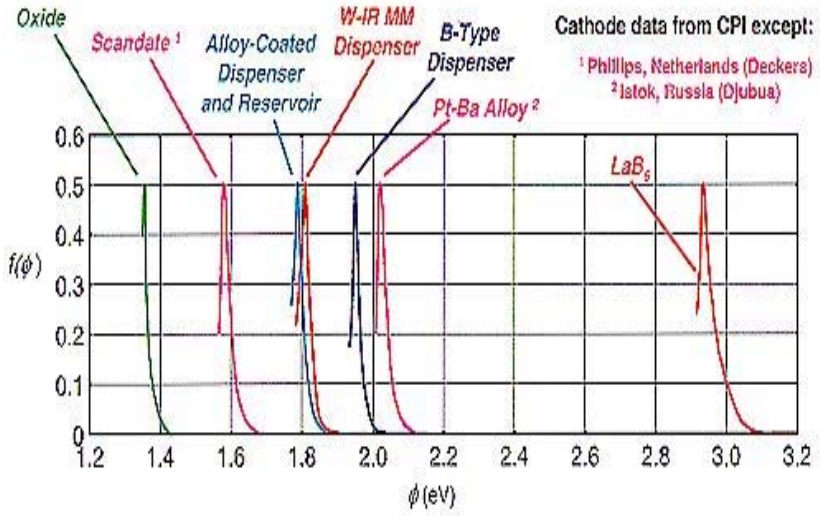

Figure 10. High field measurements of work function distribution for a range of commercial thermionic cathode types (see Cattelino 1997).

This dispersing role that a sputtered capping layer plays is more evident when considering the microstructure of the W pellet that serves as the substrate and Ba/O reservoir. W cathode pellets are typically sintered from 4 to 6 micron diameter particles and generally contain less than 20% porosity. After impregnation, excess oxide must be removed from the pellet surface and, as in the case of the cathode studied, removal by mechanical polishing is used. Remnant polishing marks are visible in plan view electron micrographs of the surface, as seen in Figure 11b. Micron-size or larger pores, appearing as dark features in the image, intersect the surface at relatively low densities. These larger pores are elongated in the polishing direction due to surface deformation. The sub-surface impact of polishing can be seen in the cross-section electron and ion generated views as seen in Figure 11c and d. In these images, we find that an approximate 1 micron layer of deformation damage is retained after the short-term activating thermal treatment. The focused ion beam milling used to generate these cross-sections was oriented perpendicular to the polishing direction. We observe vertically compressed grains that most likely have a longer axis along the out-of-plane or polishing direction. The ion beam image tends to highlight some of the grains preferentially due to orientation and ion channeling. We note that the deformation layer does not exhibit a significant degree of porosity itself. However, porosity is evident in the W pellet below this deformation layer with several 0.5 to 1 micron cross-sectional diameter oxide filled pores (dark regions for electrons, light regions for ions). The low density of pores that extend through this damage layer as seen in both cross-section and plan view microscopic images suggests a strong role for redistribution of transported Ba and O by the sputtered alloy surface layer.

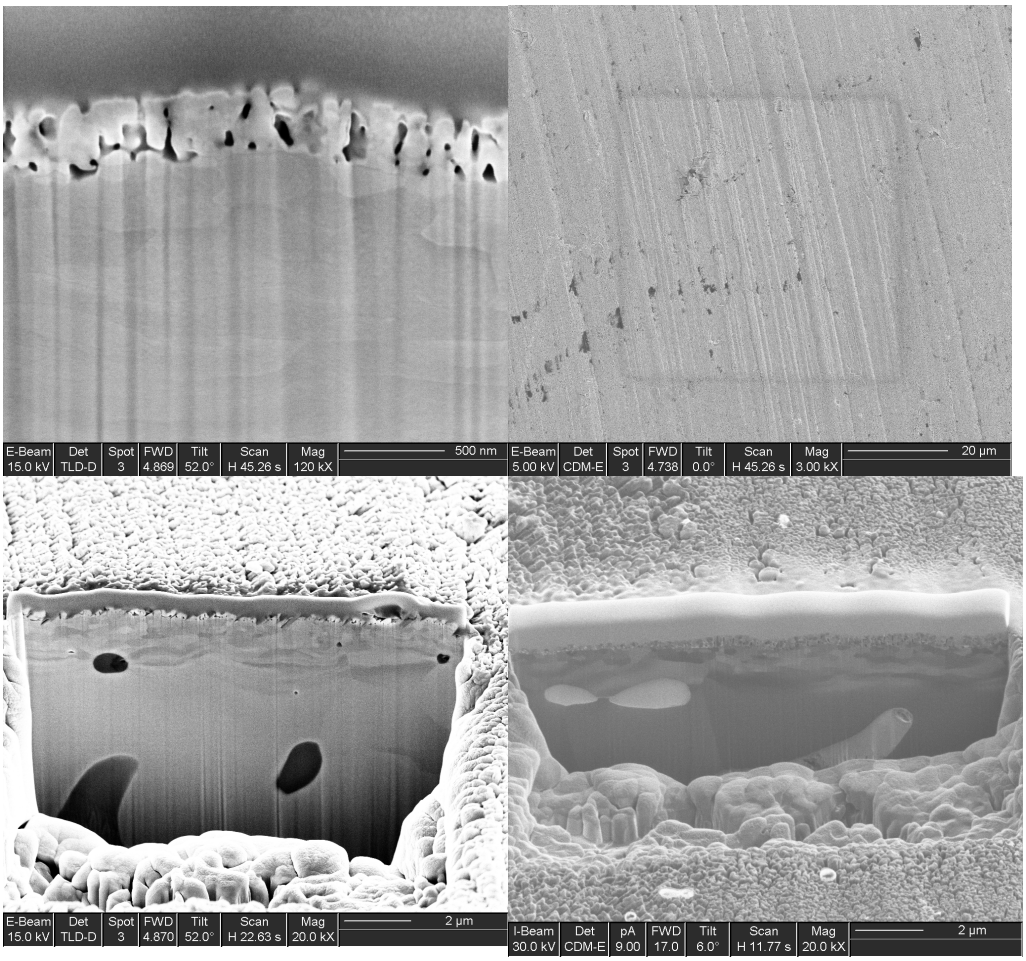

Figure 11. Cross-section (15 keV Ga^+ ion milling) and plan view electron and ion microscopic images of a HeatWave Labs Inc. commercial M-style cathode after annealing to 1220 K for 16 hours - a) electron image (15 keV) of the 0.3 micron Os/Ru sputter deposited capping layer, b) electron image (5 keV) of a region of interest subjected to prior SIMS analysis (square pattern in image center), c) electron image showing the 1 micron thick deformation layer from polishing and oxide-filled pores in the tungsten pellet (dark regions) and d) ion image (30 keV) also showing the 1 micron thick deformation layer from polishing and oxide-filled pores in the tungsten pellet (light regions).

Direct evidence for effective Ba and O transport dispersion through this layer can be found using local compositional probes. Figure 12 shows the results of a secondary ion mass spectrometry depth profile as a three-dimensional display. The data was generated with a 25 keV Ga^+ source focused to approximately 0.25 micron. Individual mass spectra were acquired in a 256x256 array and then analyzed using Sandia's AXSIA (Kotula 2003) multivariate curve resolution software. This analysis package uses an alternating least squares algorithm to represent the chemical variance in all of the data in as few phases (either discrete chemical compositions or mixtures of compositions) as is statistically meaningful. The results of this complete analysis show that a phase comprised predominately of BaO (green) is distributed across the surface. Immediately underneath this layer is a surface metal oxide phase with strong contributions from Os, Ru and W. With additional sputtering, the surface metal oxide phase is strongly attenuated due to a lower secondary ion yield in the absence of the oxygen anion. Only the BaO dominated phase is

left in what appear to be pores extending 0.2 micron into the cathode surface. These pores correspond to the larger pores seen in the electron micrograph of Figure 11b. The upper left corner of the indicated SIMS analysis region in Figure 11b corresponds to the lower left corner in the projected 3-D phase map of Figure 12. So, despite the inefficiently distributed reservoirs (pores) of oxide, Ba and O appear to be effectively transported and redistributed across the cathode surface. It is this basic set of structural features, including: 1) a reservoir of Ba and O, 2) a metallic body to provide a local reductant and electrical conductivity, and 3) a modified metallic surface for electron emission, that we seek to create in a thin film technology for the purpose of generating dispenser cathodes for miniaturized applications.

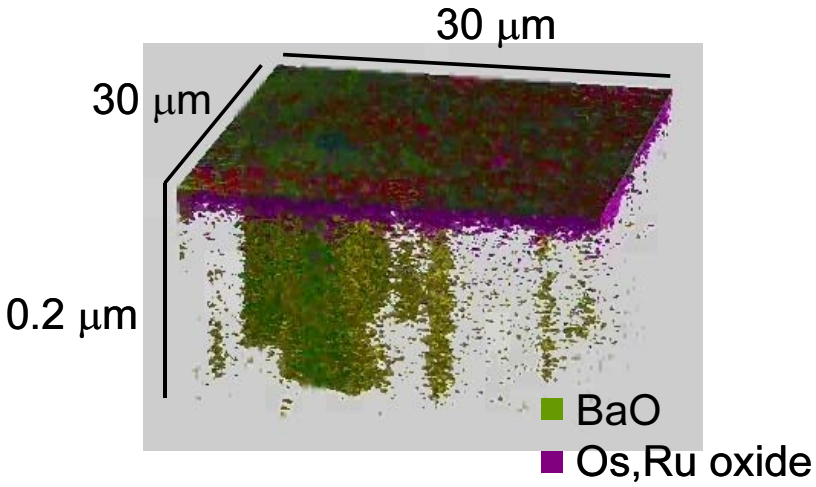

Figure 12. Three dimensional depth profile of an annealed M-style cathode (HeatWave Labs Inc.) using Sandia's AXSIA multivariate analysis software.

2.2 Thin Film Dispenser Cathodes

Early studies showed that one reasonable strategy for producing a thin film dispenser cathode involved the deposition of a compositionally modulated film (Zavadil 2001, Zavadil 1999). This original work involved the deposition of modulated tri-layer structures that contained W, BaSrCaO (47.5:47.5:5 mole ratio), and Sc_2O_3 onto Ta electrodes. Figure 13 shows a set of grazing incident angle (2º) x-ray diffraction spectra generated on a Siemens diffractometer equipped with a heating stage. This film was heated for approximately one hour at each of the temperatures indicated. The data shows the formation of a tungstate phase at 2-θ of 28.5º at a temperature of 900 K. This product signals the reaction between closely spaced W and BaSrCaO resulting in the oxidation of W to form the tungstate and reduction of Ba^{2+} to produce free Ba^{o}. Diode tests shows these films become electron emissive above 900 K. Cross-section electron microscopy shows evidence for void formation in the film with annealing. The thermal reduction/oxidation chemistry with W produces moving reaction fronts. Voids form due to differing density phase formation and consumption, specific volume differences and/or stress generated at reaction fronts. This combination of W oxidation, electron emission and void formation were deemed as favorable indications that further optimization of these types of films could lead to acceptable emission characteristics.

Several changes in our film fabrication strategy were implemented to better facilitate emitter optimization. We chose to use the ternary oxide $BaO:CaO:Al_2O_3$ in a 4:1:1 mole fraction as our candidate oxide with the intent of maximizing the Ba content in the resulting films. Previous experiments had taught us that keeping the W interlayer thickness well below 100 nm prevented the possibility of columnar grain growth over the range of substrate temperature and Ar sputtering pressure available on the deposition system. It is essential to avoid columnar growth of W grains because of the hygroscopic nature of the oxide. We have found that W layers at 50 nm or less are sufficiently non-transmissive to atmospheric moisture that oxide and film stability can be assured for prolonged periods of atmospheric storage.

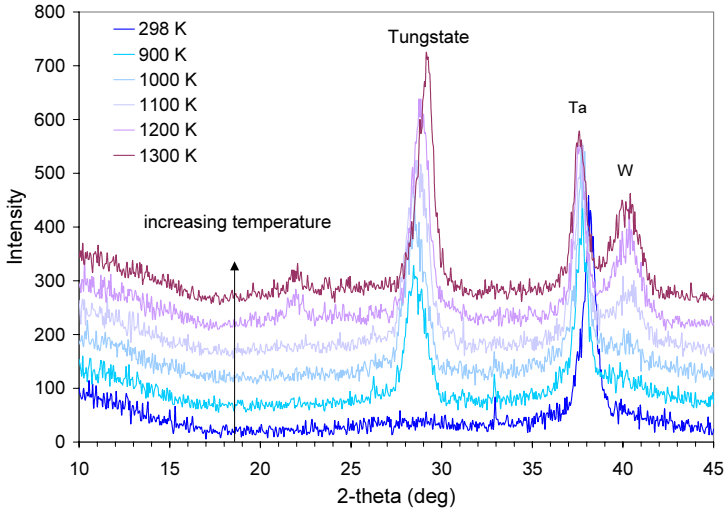

Figure 13. Real-time grazing incident angle (2º) x-ray diffraction spectra as a function of annealing temperature for a compositionally modulated film comprised of 47.5:47.5:5 mole fraction BaO:SrO:CaO and W.

Additional materials selection for these modulated emitter films were largely guided by the expectation of low temperature operation (on the order of 600-800K). King 1999 had previously shown that Pt films on quartz substrates proved stable electrodes for subsequent deposition and comparable temperature operation of Ba,Sr,CaCO3 cathode films. We designed a shadow mask set for depositing a Pt-based electrode structure with imbedded thermocouple (Pt/PtRh) for integrated temperature measurements. In addition, techniques were developed for welding 75 μm diameter Pd wires to the Pt electrode surfaces for electrically addressing the emitter (voltage biasing and current collection). Pt is by no means an ideal material for MTC temperature operation, but represented a reasonable starting point for the prototype work completed in this project.

2.3 Achieving Desired Microstructure

Thin film dispenser cathodes are formed by the modulated deposition of a ternary oxide and tungsten (Zavadil 1993). The resulting film structure is shown in the electron micrograph of Figure 14. This film is comprised of 33 sequential 4:1:1 mole fraction $BaO:CaO:Al_2O_3$ and W bi-layers. Figure 14 shows a backscattered electron image of an as-deposited film where the

thickness ratio of oxide to W is 2:1. This cross-section sample was produced by fracture of emitter, electrode (500 nm W, 500 nm Pt and 200 nm Ta, film-to-substrate), and substrate (polycrystalline AlN) assembly. The W show up as the bright layers due to a higher backscatter coefficient based on it larger atomic mass. The outer-most layer of this modulated structure is a 3 nm Re/2 nm Sc_2O_3 bi-layer. This layer is not discernable in the micrograph, but is detectable using surface electron spectroscopy. The vertical discontinuity evident in the film just right of image center lies directly above a grain boundary in the underlying AlN substrate. These substrates are not optically flat and, as shown in succeeding surfaces images, contain remnant grain pull-out depressions from the polishing process. It is unknown whether the array of defects generated by these structures contributes to material transport in the film at elevated temperatures.

Annealing of a compositionally modulated W/oxide film produces large-scale changes in the film microstructure. Figure 15a and b show cross-section and plan views of a modulated film after heating to 1150 K for 28 hours. This film is also a 33 bilayer structure with a 1:2 oxide to W ratio and deposited onto an optical quality sapphire substrate. A 25 nm W and 25 nm Ir layers were deposited onto the last oxide layer to serve as a capping emission surface. An underlying electrode structure of 400 nm W, 500 nm Pt and 100 nm Ti (ordered film-to-substrate) was used. These images are of secondary electron emission (as opposed to backscattered) and the cross-section was produced by focused ion milling. Annealing to electron emission activation temperatures produces voids centered in the dark or oxide bands of the film signaling the onset of thermal reduction/oxidation chemistry. Of note is a disproportionate void size and density in the first oxide layer below the metal terminated surface. The Ir/W capping layer appears as the outermost bright layer, measures 40 to 60 nm thick in this image, and appears continuous. The uniform field about this layer is sacrificial Pt that is deposited over the region to be ion milled. This larger first layer void size and density phenomena may reflect the ease of material transport through the outer metal layer. These short transport distances appear to contribute to the short times and low temperatures necessary for detecting first electron emission. A faster response of the cathode is a clear advantage for micro-devices where power limitations and thermal limits may exist and prevent accelerated activation protocols.

The microscopy also shows that the metal surface layer stays in tact during early stages of film annealing. As noted in the discussion of Figure 15a, the cross-section view shows the Ir/W layer to be continuous. Figure Figure 15b shows a plan view image of the annealed Ir/W surface layer in close proximity to where the ion milled cross-section preparation was conducted. The surface layer clearly remains in tact showing a range of grain sizes from 20 to 100 nm in diameter. Auger electron spectroscopy shows the presence of both W and IR at the surface with annealing up to 1150 K. We would anticipate temperatures to be too low for effective alloying of these substantially higher melting point materials, although Auger electron spectroscopy with annealing showed some progressive development in the underlying W(MNN) spectral intensity. It is possible that mass transport of Ba and O through the terminating layer may be driving these changes. A low density of pores penetrating this surface plane is also observed with diameters in the 20 to 50 nm range. Other locations on this and similar surfaces where equally as likely to show the presence or absence of voids. These pores may align themselves with voids in the underlying oxide forming through vias to assist in Ba transport to the surface. Comparison of relative Auger electron spectroscopic Ba(MNN) intensity with literature values for commercial

cathodes argue for the presence of approximate monolayer Ba coverage over $1x10^{-3}$ cm^2 analysis areas (Zvadil 2003). So, either the pores or a combination of these features and grain boundaries are the path for Ba and O transport to the emitter surface.

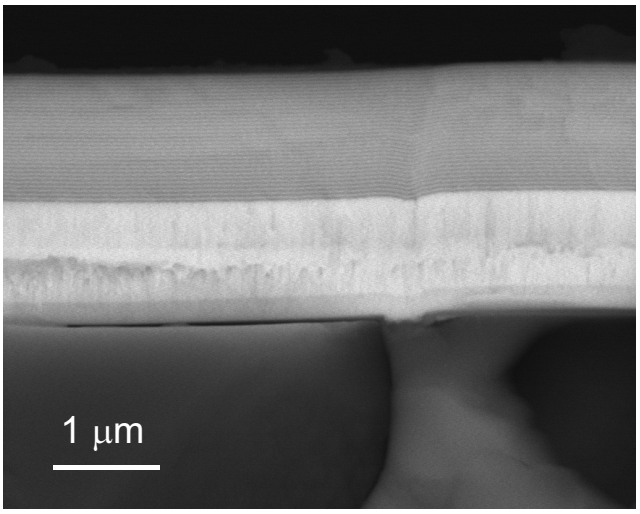

Figure 14. Backscattered electron micrograph of a fractured cross-section for a sputter deposited compositionally modulated $BaO:CaO:Al_2O_3$ /W film. The alternating bright layers in the upper portion of the image are 10 nm thick W while the darker layers are 20 nm thick 4:1:1 mole fraction $BaO:CaO:Al_2O_3$. The bright columnar structure at the image center is a W/Pt/Ta stack sitting on a polished AlN substrate.

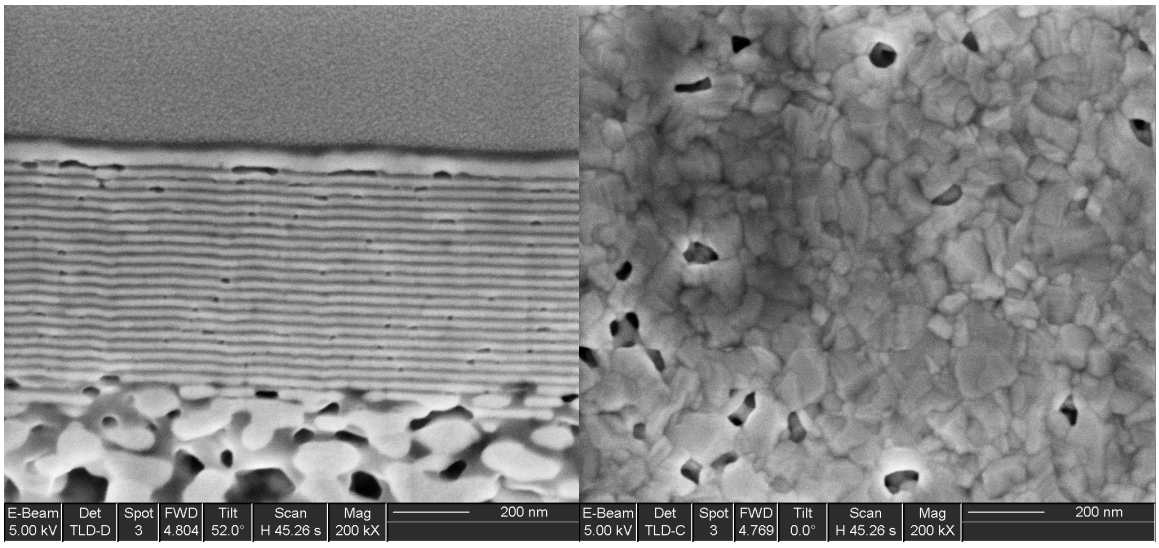

Figure 15. Electron microscopy of a thin film cathode annealed to 1150 K for 28 hours: a) secondary electron image of an ion milled cross-section of the film and b) secondary electron image of the surface showing retention of the 50 nm Ir/W metal capping layer. This film is a 33 bilayer stack of 10 nm oxide/20 nm W film on a W/Pt/Ti electrode on sapphire.

Film annealing also produces a tendency for extensive W layer coalescence. Evidence for this is seen in the lower third of the film in Figure 15a. Here we see W grains that have grown to

dimensions of 100 nm or greater along their major axis, surrounded by the darker appearing oxide phase. Larger size voids are also apparent throughout this same region. The fact that this process initiates in the lower portion of the film argues that some physical or chemical aspect of the interface is driving the W coalescence. A more complete view of potential causes of coalescence can be obtained by analyzing the combined response of the metal electrode structure and the oxide/W bilayers. As seen in Figure 16a, coalescence is limited to the bilayer region. The point at which W particle formation and growth is evident is the original first oxide layer – 400 nm W barrier electrode layer. Where we observe void formation and non-columnar grains in the Pt electrode structure below this layer, the W barrier electrode layer appears to have maintained its as-deposited columnar microstructure. Monte Carlo modeling by Battaille, as described in the next chapter of this report, indicates that in a chemical system where a coarsening or ripening process is favorable there is no a priori reason for any preferred location for this process to initiate. This combination of results suggests that there is a chemical cause for this coalescence process.

The most likely candidate for driving coalescence appears to be Ti used as a surface adhesion layer for the Pt electrode. We have successfully used W/Pt/Ta tri-layer structures (on AlN) heated to temperatures as high as 1300 K for tens of hours and not observed significant microstructural changes in the Pt and W layers. These near-term results argue that an intrinsic instability between Pt and refractory metals like W and Ta are not cathode film limiting.

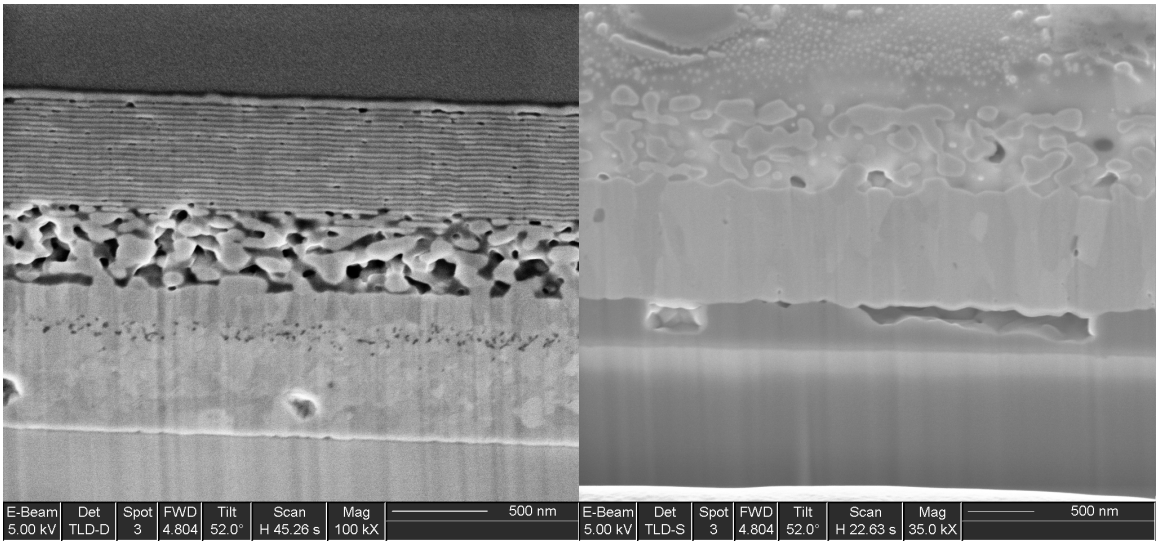

Figure 16. Cross-section electron micrographs of two compositionally modulated cathode films deposited onto a base electrode containing Pt and Ti as an film adhesion promoter showing the potential effects of Ti diffusion on W coalescence: a) a Ir/W terminated film comprised of 33 bi-layers of BaO:CaO:Al_2O_3 (10 nm) – W (20 nm) deposited on a W/Pt/Ti electrode on sapphire heated to 1120 K for 28 hours and b) a Re/Sc_2O_3 terminated film comprised of 33 bi-layers of BaO:CaO:Al_2O_3 (20 nm) – W (10 nm) deposited on a W/Pt/Ti electrode on quartz heated up to 1173 K for 1000 hours.

The potential activity of a chemical initiator for coalescence could be cathode source limiting. Figure 16b shows the result of a 1000 hour anneal of a modulated film deposited onto a quartz

substrate using a Ti-bonded Pt layer underneath a 400 nm W barrier layer. This specific film was comprised of 33 bi-layers of 20 nm oxide and 10 nm W with a Re/Sc_2O_3 capping layer. No remnant of the original bi-layer structure remains after extended annealing. The remaining W has fully coalesced and the oxide appears to define the outer surface plane. So a metal terminated cathode has been transformed to an oxide terminated cathode and one would expect a significant change in emission properties as a result. This transformation could be problematic from the perspective of maintaining a uniform, minimum surface work function. The transformation to a mixed oxide/metal surface would be expected to produce domains of two different work functions. If the difference is sufficiently large (several tenths of an eV), the higher work function regions will dominate electron emission at low applied fields. This effect could be overcome by applying a sufficiently larger accelerating field in the diode or triode device to overcome local field effects at the surface. However, for energy conversion purposes where field is defined as the work function difference between emitter and collector, the high work function will dominate. Further transformation of the surface to an oxide would simply pin the emitter properties (work function and emission coefficient) to the oxide values.

Strategies may exist for minimizing W particle growth. An example is shown in the cross-section image of Figure 17. This film is formed by depositing 33 layers comprised of 20 nm oxide/10 nm W bilayers, where the oxide was deposited in a $3x10^{-3}$ torr background pressure of CO_2. The goal in this deposition was to stabilize the oxide layers via carbonate formation against moisture ingress during lithographic processing and to provide a secondary activator for Ba^o production in the form of C. This film was annealed to 1300 K for 3 hours after extended annealing (30 hour) at a lower temperature (1050 K). The image shows a much smaller scale W coalescence with individual layer break-up and void formation. Surface spectroscopy shows that the original 3 nm Re terminating layer remains continuous at 1300 K. Surface composition of these annealed films using scanning Auger spectroscopy (30 nm diameter incident electron beam) show that the Re surface film remains continuous. We attribute this surface layer stability to the presence of C is some chemical form in the film and potentially a pinning effect for W grain growth. We also find that small islands of Ba and O start to appear on the surface with annealing indicating a route for mass transport does exist. However, the electron emission properties of this type of film do not compare favorably to films deposited in the absence of CO_2 arguing that optimization will be required to produce viable emitters using this concept.

The roles of these chemical additives in the form of Ti and C are still speculative. They may suggest more interesting ideas on controlling morphology. A ripening additive or accelerant could be added in just the right quantity and in specific locations in the film to provide a method for controlled release, mixing, or mass transport to tailor the emission properties of the cathode. If this accelerant becomes bound in a product phase and essentially deactivated, its effect may be short lived to provide a specific function at a specific time.

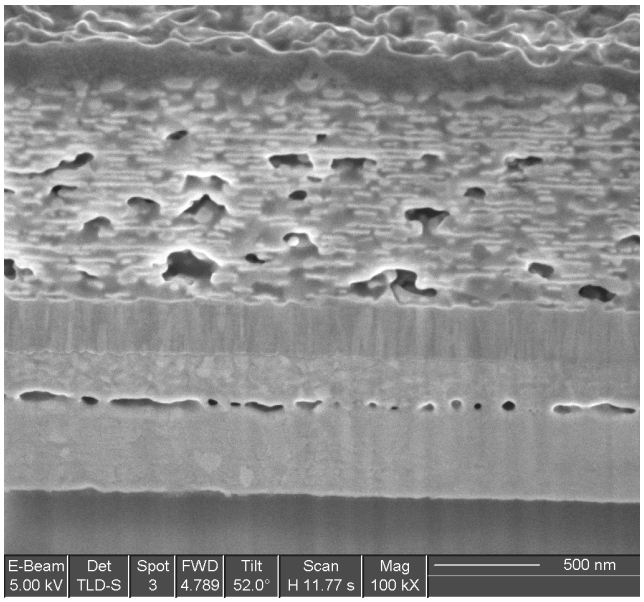

Figure 17. Compositionally modulated film heated to 1300 K with the ternary oxide deposited in CO_2 showing the typical signs of oxide/W redox chemistry along with a possible chemical pinning for W coalescence.

2.4 Film Surface and Emission Properties

The advantage of a modulated structure is the potential for low temperature activation and stable emission. Activation can be tracked by monitoring the current output of an emitter under bias in a simple diode configuration as a function of anneal temperature or by monitoring the surface chemical change also as a function of anneal temperature. Figure 18 shows the results of surface chemical analysis (Auger electron spectroscopy) over the initial annealing process for a compositionally modulated film terminated with a 3.5 nm Re and 2.5 nm Sc_2O_3 layer. The results show that Ba and O first start to populate the Re surface at a temperature somewhere between 825 and 875 K. Diode emission tests results show the first appearance of emission current (nominally 10 $\mu A \cdot cm^{-2}$ at voltages just into saturation) in this same temperature range. The fact that Ba and O are detectable at room temperature is in part a result of sampling depth sensitivity (electron inelastic mean free path), the thinness of the Re overlayer, and the possibility of O on the Re surface with air exposure after original film deposition. The first increase in Ba and O signals is the indicator for mass transport to the surface. Also worth noting, is the fact that the OVV lineshape was used for quantifying Re and, due to the overlap of this spectral series with the W(OVV), we detect essentially a composite refractory metal signal in this experiment. Irrespective of the relative Re and W near surface composition, we do learn that this thin surface film is retained up to temperatures of 1050 K. The oscillation in this signal appears to be due to the adsorption of CO on the surface during annealing as evidenced by an out-of-phase oscillating C(KVV) Auger signal. Emission current from these thin film cathodes does not stabilize until longer periods of isothermal annealing have been conducted. Presumably, stable emission is impacted by a combination of the film surface evolving to a stable chemical and physical structure as well as significant outgassing of the emitter structure.

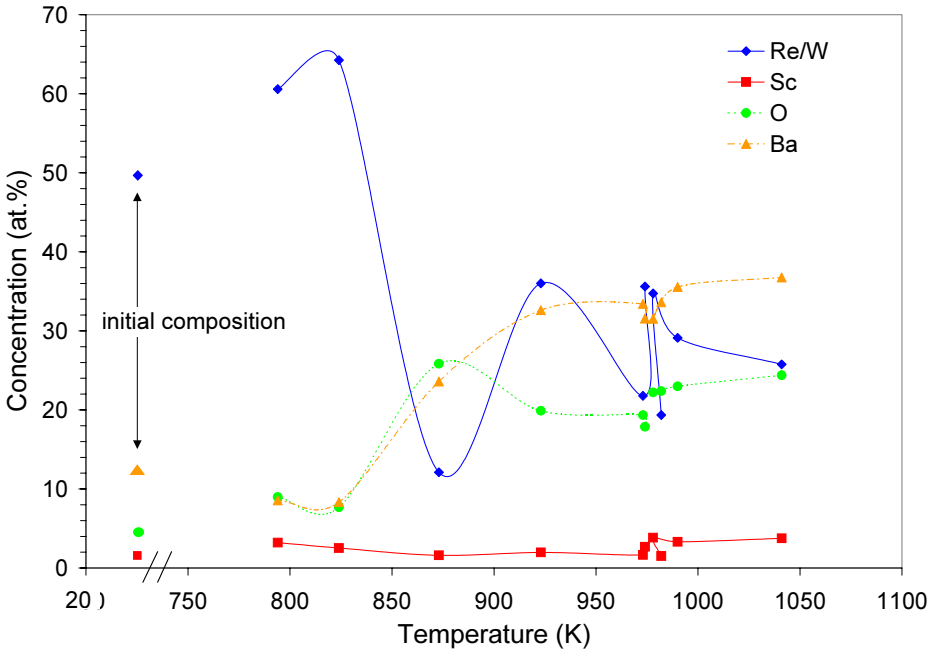

Figure 18. Variation in surface composition of a Re/Sc_2O_3 terminated cathode film as a function of annealing temperature. Activation temperature is indicated by first significant increase in surface Ba and O signals.

An emission current measurement is made to characterize the properties of the cathode film. This measurement is made in a simple diode configuration where a clean Mo collector (Argon sputtered in vacuum) is positioned anywhere from 20 to 100 μm away from the emitter surface. The collector is designed to just geometrically overlap the emitter while preserving conductance around the diode gap perimeter for the effective pumping of outgassing species. The collector potential can be swept or pulsed relative to the grounded emitter to measure forward and reverse bias currents. An example of the temperature dependent emission current density is shown in Figure 19 for a stabilized Ir/W terminated film. Of note is that fact that current density rapidly rises at a minimal forward bias potential and exhibits a sharp transition to a saturated value. The observed saturation condition is an attribute of small diode gaps where space charge effects due to high emitter electron densities immediately outside the cathode surface are less likely to develop. The rapid transition to saturation is a characteristic of an emitter with a reasonably uniform work function. The fact that emission current occurs below a zero applied voltage is due to the fact that Ba eventually adsorbs onto the Mo collector and lowers its work function. This phenomenon is in fact the principle of an energy converter where only thermal energy need be input to the emitter and the temperature difference between the two matched electrodes would drive current flow through a micron scale gap. We have found that current densities of 10 $mA \cdot cm^{-2}$ can be generated at 1200 K under these true zero applied field conditions, indicating that with optimized emitter design, moderate temperature energy conversion in a micro-device is achievable.

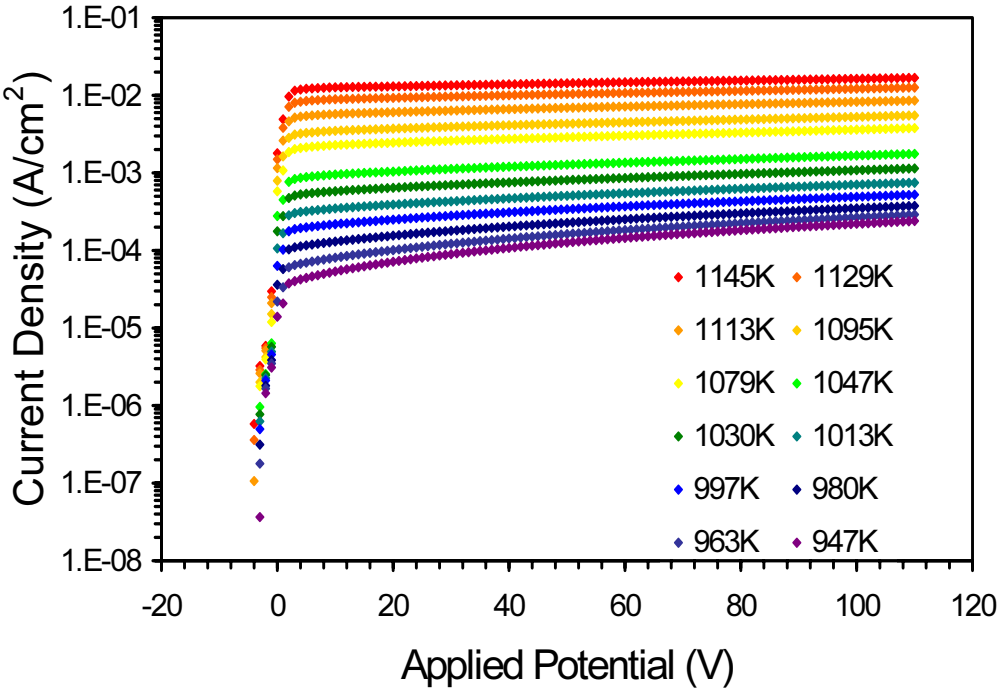

Figure 19. Variation in emission current density vs. forward bias potential as a function of temperature for a diode comprised of a Ir/W terminated film emitter and a Mo collector separated by 100 μm.

A comparison of a Sandia micro-dispenser cathode with commercial cathodes highlights this difference in work function uniformity as shown in Figure 20. In this figure, the emission current is normalized so that a direct comparison can be made for the respective emission profiles. We find that the HeatWave M-style (or top layer) cathode shows the sharpest transition while a HeatWave scandate cathode shows the most gradual approach to saturation. A Re/Sc_2O_3 terminated μ-dispenser film shows an intermediate behavior. This comparison makes qualitative sense based on the idea of complete Os/Ru coverage of the M-style cathode surface as previously demonstrated and a W/oxide pore surface anticipated for the uncoated scandate cathode. The intermediate behavior of the μ-dispenser film is consistent with the observed metallic termination at moderate operational temperatures as shown in the previous Auger data. Our data shows that it is possible to produce stable emission in the 10 $mA \cdot cm^{-2}$ range for a dispenser cathode based on a compositional modulate thin film design that will operate at moderate temperatures (< 900° K) for short periods of time.

This emission data can be further analyzed to extract surface property data. The variation in emission current with temperature can be subjected to Schottky analysis as described previously in Section 2.3. Figure 21 shows the resulting Schottky plots for two Sandia μ-dispenser cathodes and a HeatWave scandate cathode. We note that these Arrhenius-style plots yield a reasonably linear relationship between emission current and temperature where the slope is proportional to the work function (ϕ) and the ordinate intercept is proportional to the apparent emission coefficient (A*). The theoretical limit for this coefficient is 120 $A \cdot cm^{-2} \cdot K^{-2}$. For the emission

stabilized at the maximum temperature plotted, our results show values of 2.4 eV and 39 A·cm^{-2}·K^{-2}, 2.2 eV and 5 A·cm^{-2}·K^{-2}, and 2.6 eV and an A* > 120 A·cm^{-2}·K^{-2}, for the commercial scandate, the Sandia Re capped film, and the Sandia Ir/W capped film, respectively.

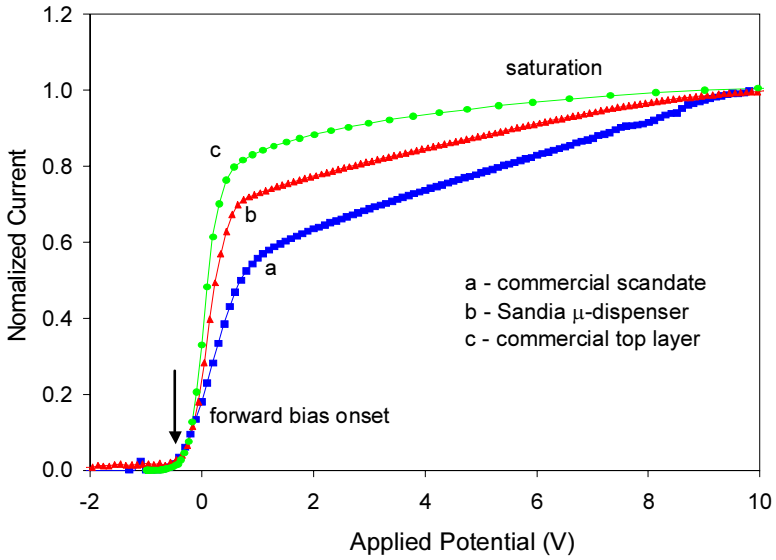

Figure 20. Comparison of forward bias emission current profiles for a two commercial cathodes and a Sandia m-dispenser cathode showing the effect of a continuous metal layer on the profile lineshape.

The origin of the anomalously high apparent emission coefficient for the Ir film is not known. Occasionally analysis of emission current will produce non-physical values. It is possible that emission properties are changing over this temperature range in a sufficiently consistent fashion with temperature so as to be masked in the Schottky plot but impact the results. If the higher temperature data for this cathode is used with a reasonable value of A* of 5 A·cm^{-2}·K^{-2}, the resulting work function becomes lies within the range of 1.9 to 2.0 eV. This value places this cathode in a reasonable work function range relative to the high field measurements made on commercial M-style cathodes (see Figure 10). Irrespective of exact values of emission properties, we find favorable short-term emission properties for these thin film emitters compared to their macro-sized commercial counterparts.

The emission characteristics for these films can be maintained for moderate periods of time. For example, we have been able to consistently measure 10 mA·cm^{-2} current densities for cathodes operated discontinuously for periods of 10 to 12 hours at 1150 to 1200 K for a cumulative period of one to two weeks. During this period we may only see 10 to 20 % variation in the output current under given applied field conditions. These results suggest significant capacity and/or limited loss of Ba through desorption during this time. We find that adsorption of select contaminants tends to have a more detrimental effect on emission characteristics over this time frame. Sulfur appears to be one particularly efficient, ubiquitous contaminant responsible for reducing emission current and that is readily detectable using Auger electron spectroscopy.

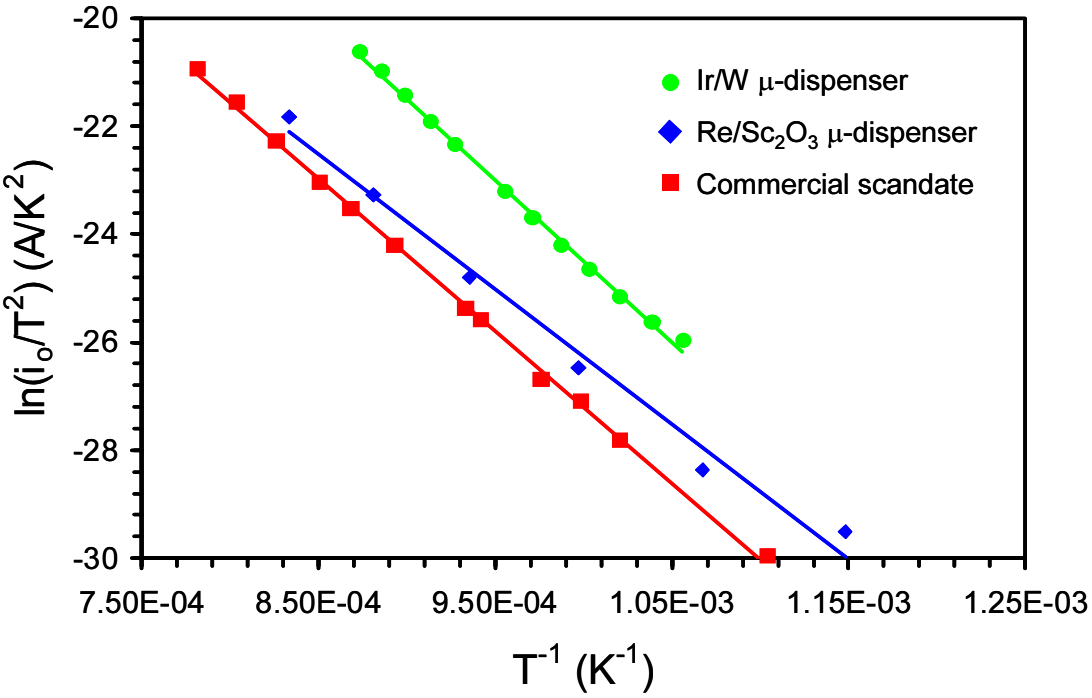

Figure 21. Comparison of the Schottky analysis for the temperature-dependent emission of several Sandia μ-dispenser cathodes and a commercial macro-dispenser cathode.

Experiments show that a minute exposure of the forward biased diode to 10^{-7} torr Ar is an effective method of bombarding the emitter surface with a 10^{15} ion·cm^{-2} fluence of low energy ions sufficient to remove the sulfur. Emission current densities require several minutes after this gentle sputtering process to recover to pre-contaminant levels. The source of sulfur could be any number of metal components used in mounting our cathode coupons. We have focused on using arc cast Mo that has been H_2 annealed for the thermal fixture in direct contact with the heated coupon. Stainless steel screws are also H_2 annealed. Other components in thermal contact with emitter coupon are foils and spring contacts made of high purity Ta and W. The relative ease with which the emitter surface can become contaminated drives home the point that a dynamic surface with some degree for recovering its physical and chemical state is what is required for stable, optimized emission. This susceptibility toward contaminants clearly places constraints on the packaging and hermeticity requirements of a micro-device using this type of emitter.

Emitter lifetime is limited for long-term operation of these μ-dispenser cathodes under conditions where W coalescence is unconstrained. Figure 22 shows a series of elemental maps generated by scanning Auger spectroscopy for a Re/Sc_2O_3 terminated film after 1000 hours of operation. The bulk microstructure of this film was previously shown in Figure 16b and exhibited complete transformation of the original 10 nm W layers into W particles with cross-section greater than 100 nm. Secondary electron images show that the emitter surface is comprised of grains with dimensions of several hundred nanometer up to 2 micron. The Auger images show that these grains are comprised of principally CaO, BaO and Al_2O_3. Ca signals are enhanced around grain perimeters indicating that it preferentially segregates at the grain

boundaries. The images also show an alternating enrichment in either Ca or Al for ensembles of individual grains. Ba content appears slightly enhanced in the Al_2O_3 enriched grains. We find no measurable Re or Sc signals, the constituents of the original 5 nm surface layer. Nor do we find evidence of W or any of the substrate electrode components. Defocused electron beam excitation, compared to the 30 nm incident beam diameter used to generate the images of Figure 22, also showed the absence of W and Re. These results show that over a long enough period of time this emitter has been transformed to essentially an oxide cathode. Of interest is the fact that this film continued to exhibit emission although at levels below our nominal 10% normal variation observed for near term film operation. This film could still be operated in essentially a DC mode without significant detriment to saturation current densities presumably due to its thinness and the presence of W contributing to sufficient electrical conductivity to support carrier transport.

2.5 Conclusions from Materials Development for μ-Dispenser Cathodes

We demonstrate that a dispenser style cathode can be generated in thin film form by modulated deposition of a Ba-containing ternary oxide and W. These films generate free Ba at their surfaces upon annealing and exhibit relatively uniform work function values of nominally 2.0 eV. The modified metal terminating layer governs near-term emission properties of the films. Moderate temperature, low field emission characteristics are comparable to commercial macro-dispenser style cathodes. Microstructural evolution can occur with film annealing, resulting in W coalescence and continued particle growth. The cause of this coalescence appears to be mobile additives, like Ti, used in the electrode structure on which the film is deposited. If coalescence continues unchecked, these films transition from a metal to an oxide terminated surface. Emission properties then become more characteristic of classic oxide emitters, however, without the constraints of significant electrical resistivity still allowing for direct current operation. Based on our findings, we have described possible methods for controlling and taking advantage microstructural evolution in these films to the benefit of optimizing emitter performance. Key technical challenges remain in order to implement this type of emitter or emitters based on other materials classes and structures. Our work emphasizes that the preservation or regeneration of the surface dipole composition and structure is essential in achieving optimum low temperature and long-term operation. This criterion places significant stringent requirements on the packaging and resulting hermeticity of envisioned micro-devices.

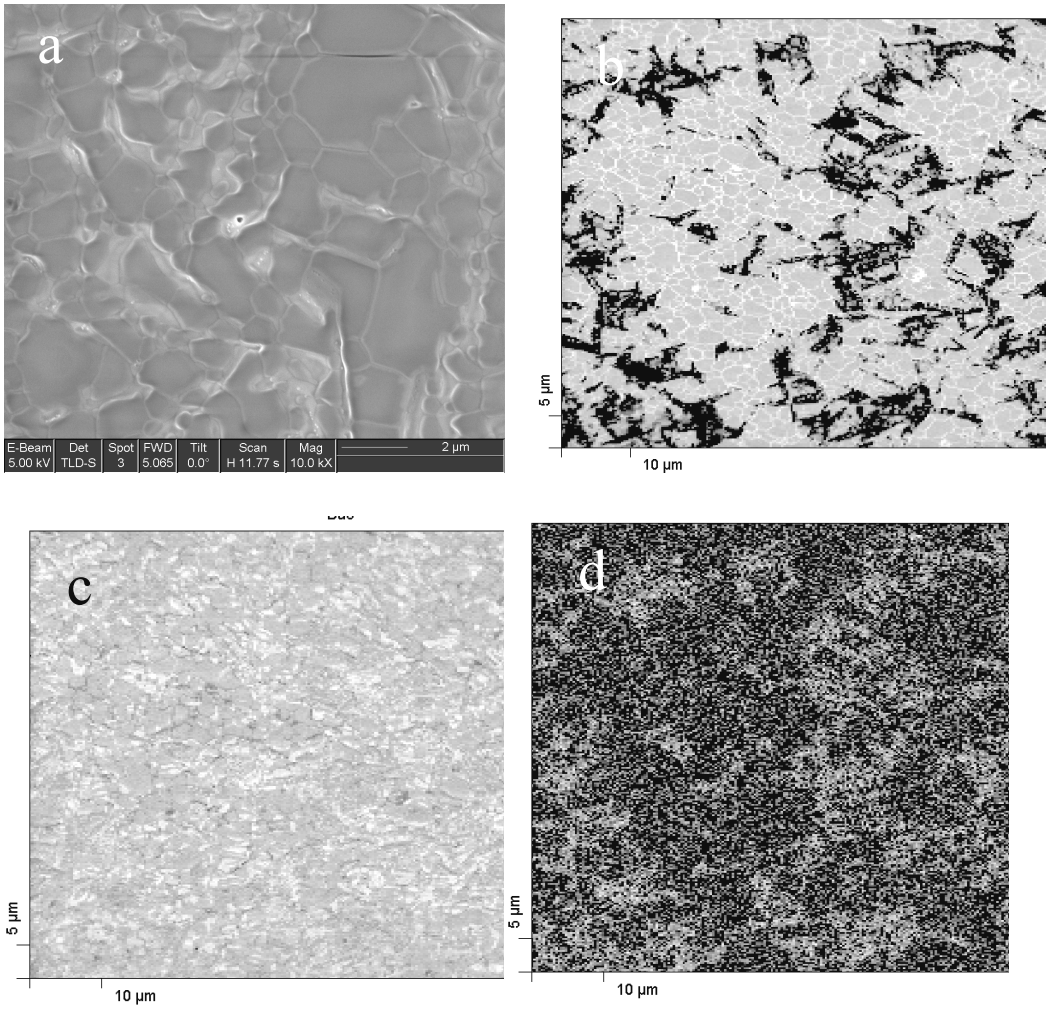

Figure 22. Secondary electron (a) and Ca (b) Ba (c) an Al Auger (d) images of a 1000 hour, 1220 K annealed 35 layer, 20 nm oxide/10 nm W film on a W/Pt/Ta electrode on quartz.

3. Microstructure Based Modeling

In a thin film material where reduction of the work function occurs by the formation of surface structures from species that diffuse from the bulk, it is important to understand how the film's microstructure evolves with time, and how that affects the diffusion of the pertinent species to the surface. Microstructure-based modeling work in this project has therefore focused on two areas: coarsening and diffusion in idealized two-phase materials. Since no specific quantitative data are available for the coarsening of tungsten / oxide materials or the diffusion of Barium through these materials, we focus on establishing qualitative insight into these phenomena by correlating experimental observations with generalized model predictions.

3.1 Microstructural Evolution

3.1.1 Two-Phase Microstructures

In order to simulate the evolution of a two-phase layered microstructure, we use a Monte Carlo (MC) approach that evolves the phases to minimize the total interfacial area (and thus the system's energy) while preserving the volumes of each phase. The microstructure is discretized onto a grid, and each point on the grid carries an integer tag that identifies it phase. The interfacial energies between all the different phases (two for the present purpose) are tabulated and input to the simulation. At each time step in the simulation, a grid point, also called a "lattice site," is chosen at random. The adjacent sites are examined, and if any are of a different phase than the chosen point, then one of these differing neighbors is also chosen at random. Based on the interfacial energies, a calculation is performed to determine the energy change that would occur if the phase identities of the two chosen sites were exchanged. The exchange is implemented if

$$\xi < P\Delta t, \tag{1}$$

where ξ is a random number between zero (inclusive) and one (exclusive), Δt is the simulation time increment, and P is a probability equal to

$$P = \begin{cases} 1 & \Delta E \le 0 \\ \exp\left(\dfrac{\Delta E}{T}\right) & \Delta E > 0 \end{cases}, \tag{2}$$

where ΔE is the change in energy due to exchanging the chosen sites and T is the simulation temperature. If $\xi \ge P\Delta t$, then the exchange is rejected. The temperature is chosen to allow energy-increasing exchanges so that the system can escape local energy minima in configurational space. The energy of a particular configuration is simply the sum of the energies of all the interfaces between sites of different phases.

In this study, the microstructural evolution simulations begin with a perfectly layered, three dimensional structure of alternating phases, like the one depicted in Figure 23. The three dimensional grid is periodic in all three directions, and each site has eighteen neighboring points comprised of the closest and second closest neighbors. The simulations progress as described above, using the Monte Carlo algorithm to evolve the layered two-phase microstructure.

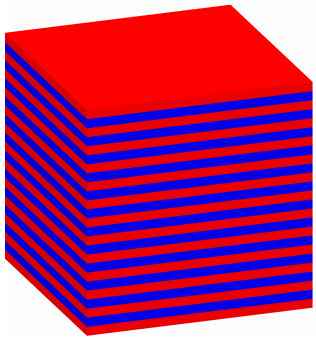

Figure 23. An example of the layered two-phase microstructure used as an initial configuration for the coarsening simulations.

Figure 24 contains the evolution of a microstructure on a grid with 100x100x100 sites, the interfacial energy between the two phases set to one, a time increment of $\Delta t = 1$, and a temperature of $T = 2$. In order to understand the behavior of the microstructure in Figure 24, it is useful to examine an idealized two-dimensional example. Consider the two-phase system in Figure 25, which contains a strip of one phase embedded in another. Because the initial structure contains only a perfectly flat strip, the first exchange in the system can only occur via the swapping of two grid points at an interface. Thus the initial configuration, at the top of the figure, can only undergo one type of site exchange as shown. This exchange is relatively high-energy, but once it occurs, the red site that has exchanged out of the strip can diffuse easily along the interface between the plate and matrix. This interfacial diffusion leads to the relatively long transient in Figure 24, wherein the microstructure does not change appreciably at the beginning of the simulation. However, as evident in Figure 25, once the continuity of the strip has been broken, it becomes much easier for sites at the gap to diffuse away from the line of the strip. Furthermore, the energy of the system is reduced as the broken ends of the strip "ball up" to minimize the interfacial length. In Figure 25, where the plates are several sites thick, breaking the continuity of a plate requires much more than merely the migration of a single site. Nonetheless, the plates in Figure 25 do eventually form holes simply by random chance, and this facilitates the decomposition of the plates at those locations to form the complex structures that emerge during the course of the simulation.

3.1.2 Surfactant Effects

Experimental observations suggest that many of the layered structures fabricated for this study coarsen directionally, i.e. from the substrate toward the free surface. One hypothesis is that a diffusing species, perhaps titanium, facilitates coarsening as it migrates from the film / substrate interface toward the film's surface. To investigate this hypothesis, we constructed coupled

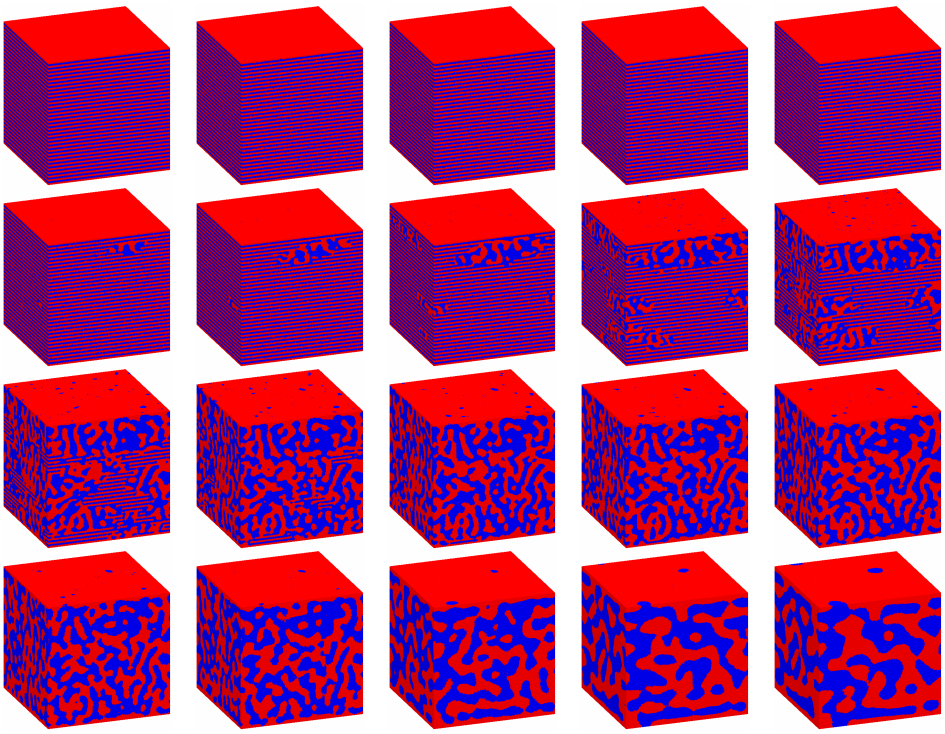

Figure 24. A time progression from a simulation of microstructure coarsening in a layered two-phase material. The simulation grid has 100x100x100 points, the interfacial energy between the two phases is one, the time increment is $\Delta t = 1$, and the temperature is $T = 2$. The images, starting from top left and progressing to the right, are from simulation times of 0, 2000, 4000, 6000, 8000, 10000, 12000, 14000, 16000, 18000, 20000, 22000, 24000, 26000, 28000, 30000, 40000, 100000, 200000, and 300000.

simulations of coarsening and diffusion wherein the concentration of the diffusing surfactant species affects the local rate of coarsening by modifying the interfacial energy.

To accomplish this, we use the same Monte Carlo algorithm described above, but with the interfacial energy dependent on the local value of a concentration field. In this modified approach, the energy of the interface between sites i and j is

$$E_{ij} = \left(2 - \frac{C_i + C_j}{2}\right) E_o \tag{3}$$

where C_i is the concentration at the location of site i and E_o is the interfacial energy in the absence of the surfactant. Thus, regions of high concentration have lower interfacial energies than regions of low concentration.

While the coarsening of the microstructure depends on the local concentration, the evolution of the concentration field is handled independently of the coarsening. The concentration is initially zero everywhere, except on the x-y plane of sites at the center of the computational domain. This plane starts with and maintains a constant concentration of unity, producing a “sheet” source at the center of the microstructure. (This placement avoids the introduction of artifacts associated with the boundaries of the computational domain.) As the simulation progresses, the surfactant

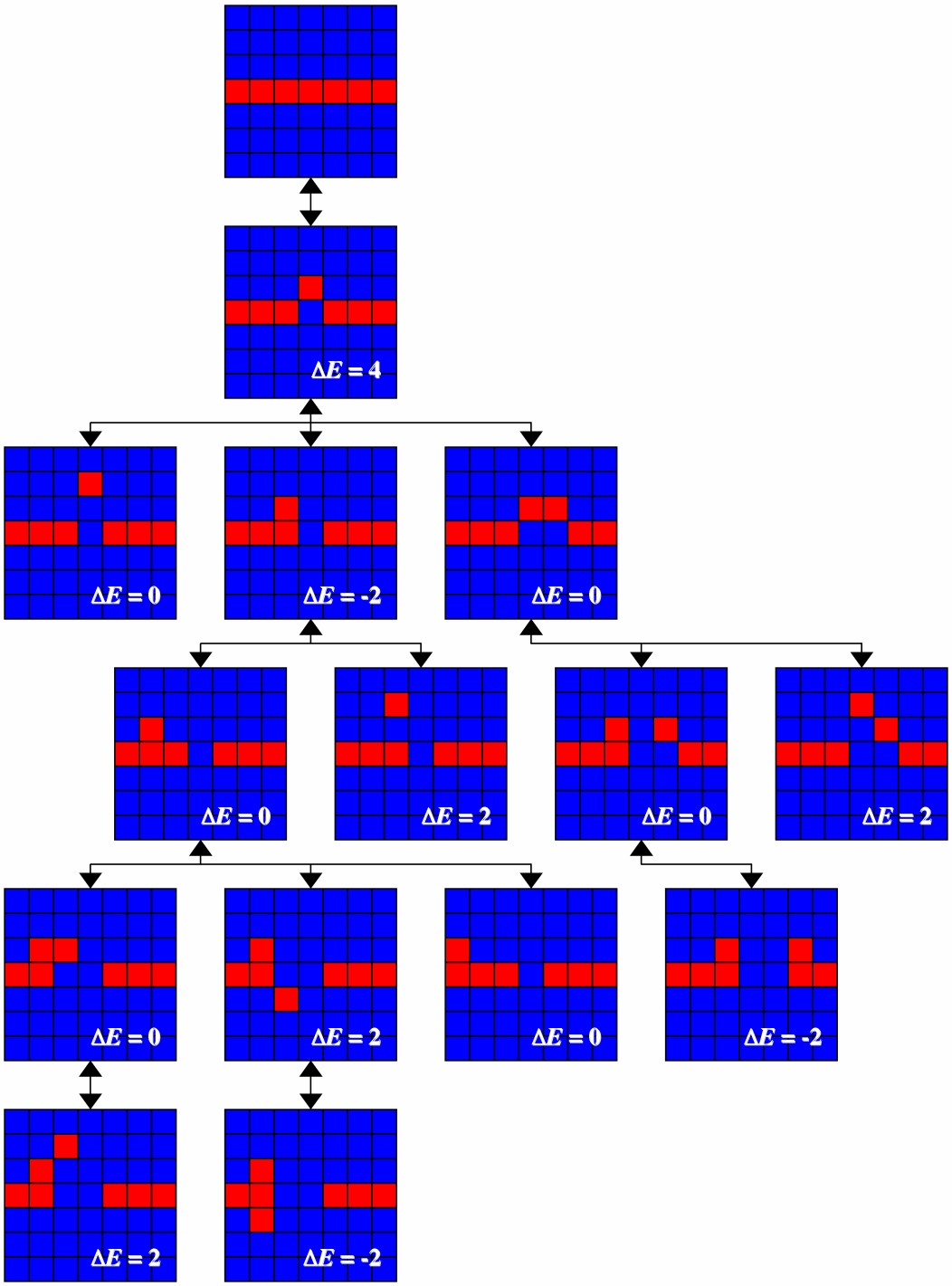

Figure 25. Examples of site exchange paths in a two-dimensional system containing a strip of one phase embedded in a matrix of another. The energy change involved in reaching each configuration is written in white text at the lower right of each frame.

diffuses (independent of the microstructure) away from the source. Simultaneously, the microstructure coarsens in a manner that depends on the concentration field. The evolution of the concentration field is performed via the Gauss-Seidel algorithm applied to simple Fickian diffusion, with a single concentration update for every 25N site exchanges, where N is the total number of sites.

Figure 26 contains the evolution of a microstructure on an grid with 200x200x200 sites, the surfactant-free interfacial energy between the two phases set to one, a time increment of $\Delta t = 0.5$, and a temperature of $T = 3$. Figure 27 shows the associated concentration field as it evolves with time. As the concentration of the surfactant species starts to spread from the midplane source in Figure 27, the interfacial energy in that region decreases below unity according to Eq 3, and thus the rate of heterophase site exchanges increases. This leads to dissolution of the plates near the middle of the computational domain, as shown in Figure 26. In the rest of the microstructure (top and bottom), where the surfactant concentration remains zero, the interfacial energy stays at its initial value of unity, and no appreciable microstructural evolution is observed. As the plates break apart near the surfactant source, they do not merge with the surrounding plates in the same manner of Figure 24. Instead, because only the plates near the middle of the microstructure can evolve quickly, they dissolve and collapse to form a thicker plate near the midplane. As the surfactant continues to diffuse, more plates dissolve and collapse onto the large middle plate. This process continues until the diffusion length between the thick central plate and the surrounding plates becomes prohibitively large and the surfactant has penetrated a large portion of the microstructure, at which time the plates near the top and bottom begin to agglomerate as in Figure 24.

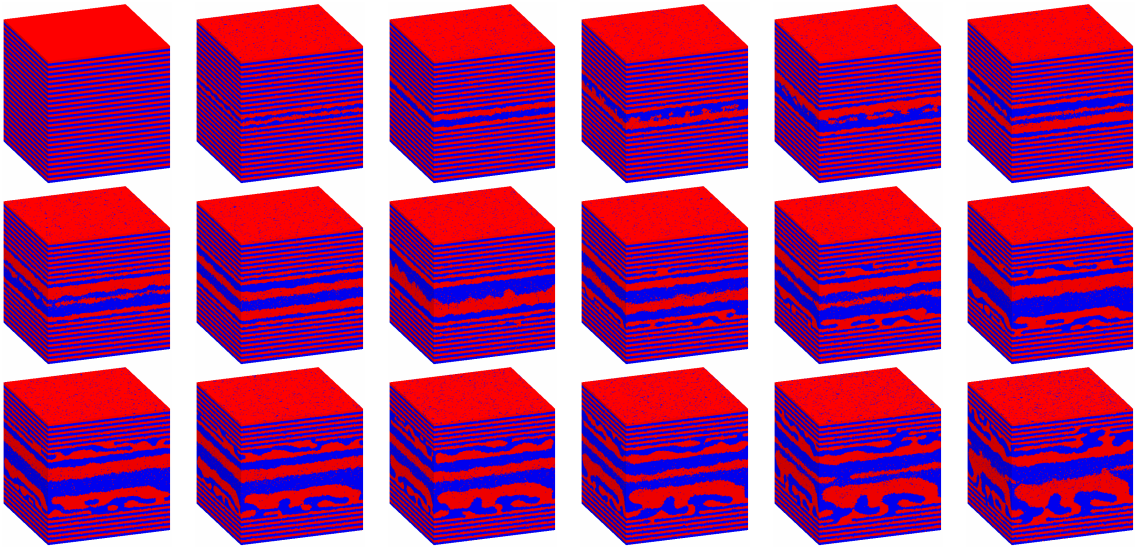

Figure 26. A time progression from a simulation of microstructure coarsening in a layered two-phase material with a diffusing surfactant. The simulation grid has 200x200x200 points, the interfacial energy between the two phases is one, the time increment is $\Delta t = 0.5$, and the temperature is $T = 3$. The images, starting from top left and progressing to the right, are from simulation times of 0, 100, 200, 400, 600, 1000, 1400, 1800, 2200, 2400, 2600, 2800, 3000, 3300, 3600, 3900, 4200, and 4500.

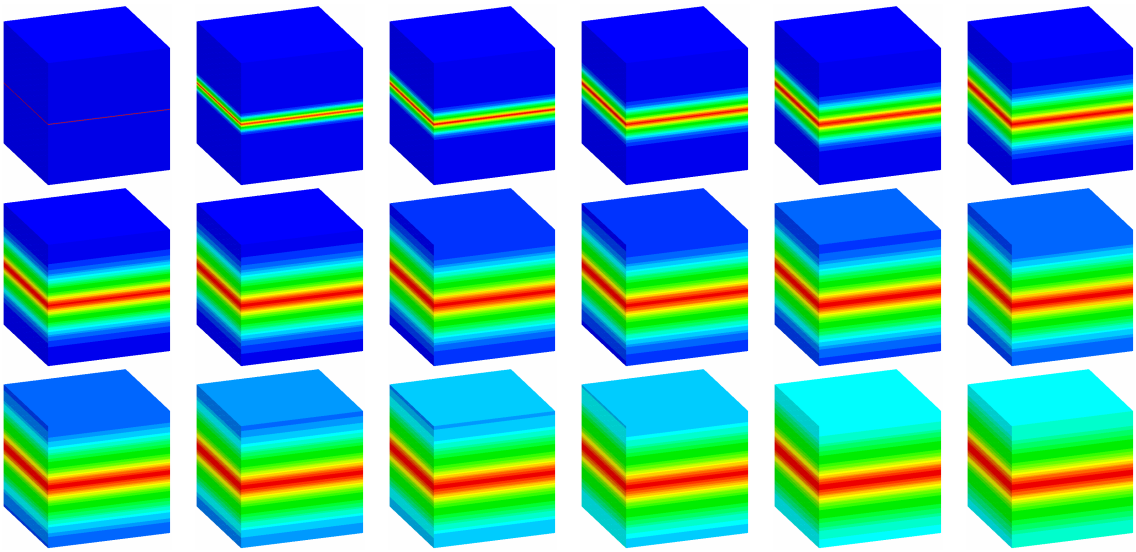

Figure 27. Evolution of surfactant concentration from a midplane source. The simulation grid has 200x200x200 points and the time increment between diffusion steps is 0.5. The images, starting from top left and progressing to the right, are from simulation times of 0, 100, 200, 400, 600, 1000, 1400, 1800, 2200, 2400, 2600, 2800, 3000, 3300, 3600, 3900, 4200, and 4500.

3.1.3 Third-Phase Reactions

While the evolution of a simple two-phase microstructure is germane to the current study, real materials are much more complex. One process that is important to the present work is the chemical reaction between tungsten metal (one of the two phases) and the surrounding barium-containing oxide (the other phase). This reaction not only produces the barium species that diffuse to the surface and likely lowers the work function, but also involves a volume contraction that can produce pores.

In order to model the chemical conversion between phases, we build on the existing framework to include a process that converts the two phases into a third phase with occasional pore generation. The frequency of pore generation phenomenologically represents the volume contraction associated with the conversion. This complicates the simple two-phase model substantially, and allows sites to do much more than just exchange. Therefore, it is useful to consider the model in terms of chemical reactions involving three phases: A, B, and C. (The generic notation is used because the reaction kinetics do not quantitatively correspond to the real physical system.)

Table 1 lists the set of reactions and rate constants used for the present purposes. Reactions 1-6 are site exchanges between the four phases (three solid phases and one pore “phase”), Reactions 7 and 8 represent chemical conversion of the A and B phases into the C phase, and Reaction 9 is pore formation to account for a volume contraction due to the conversion. These reactions are implemented in the model in the same manner as the simple two-phase coarsening described above. Specifically, a lattice site is chosen at random and, based on its species and its surroundings, an applicable reaction is chosen at random from Table 1. The chosen reaction is executed at the chosen site if Eq 1 is satisfied, where in this case the probability is

$$P = \begin{cases} k_n & \Delta E \le 0 \\ k_n \exp\left(\dfrac{\Delta E}{T}\right) & \Delta E > 0 \end{cases} \tag{4}$$

and k_n is the rate constant for the chosen reaction from Table 1. The energy change, ΔE, will depend on the local environment and on the six interfacial energy values for the six unique combinations of phases.

Table 1. Reactions used to model simultaneous coarsening and inter-phase chemical conversion. Species A, B, and C are solid phases; and O is a pore.

#	Reaction	Rate Const.	Description
1	$A + B \rightarrow B + A$	1	A/B Exchange
2	$A + C \rightarrow C + A$	1	A/C Exchange
3	$B + C \rightarrow C + B$	1	B/C Exchange
4	$A + O \rightarrow O + A$	2	A/pore Exchange
5	$B + O \rightarrow O + B$	2	B/pore Exchange
6	$C + O \rightarrow O + C$	2	C/pore Exchange
7	$A + B \rightarrow A + C$	0.005	Chemical Reaction
8	$A + B \rightarrow C + B$	0.005	Chemical Reaction
9	$A + B \rightarrow A + O$	0.004	Pore Formation

Figure 28 contains images from a simulation of simultaneous coarsening and chemical conversion, assuming no volume change (i.e. no pore formation or diffusion). Thus, only Reactions 1, 2, 3, 7, and 8 apply to the results in Figure 28. The simulation grid has 96x96x96 points, the time increment is $\Delta t = 0.5$, and the temperature is $T = 3$. The interfacial energies between the four phases are $E_{AB} = 1$, $E_{AC} = 0.8$, $E_{AO} = 1$, $E_{BC} = 0.8$, $E_{BO} = 1$, and $E_{CO} = 1$. As evident in Table 1, chemical conversion (Reactions 7 and 8) is much slower than diffusion, and so initially the microstructure in Figure 28 shows coarsening much like the previous examples, but with a small fraction of the lattice sites converted to the C phase. As time progresses, more C phase is formed, and since the A/C and B/C interfacial energies are lower than the energies of the other interfaces, the C phase tends to replace the A/B interfaces. When the amount of C phase becomes comparable to the amounts of A and B phases, the microstructure shows qualitatively similar coarsened regions of all three phases.

Figure 29 contains images from a simulation of simultaneous coarsening, chemical conversion, and pore formation. All the reactions in Table 1, except for Reaction 8 (by arbitrary choice), apply to Figure 29. The simulation grid has 96x96x96 points, the time increment is $\Delta t = 0.5$, and the temperature is $T = 3$. The interfacial energies between the four phases are $E_{AB} = 1$, $E_{AC} = 0.8$, $E_{AO} = 0.8$, $E_{BC} = 0.8$, $E_{BO} = 0.8$, and $E_{CO} = 1$. Since Reaction 8 was omitted from the simulations in Figure 29, only species B, and not species A, can convert to C. Thus, as the simulation progresses, the amount of B phase (red sites) decreases at the expense of the formation of C phase (green sites) and pores (white sites).

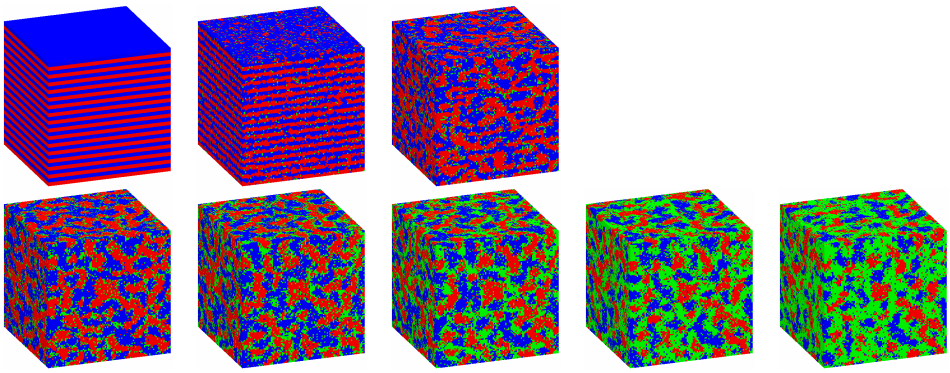

Figure 28. A time progression from a simulation of simultaneous microstructure coarsening and chemical reaction in a layered two-phase material. The simulation grid has 96x96x96 points, the time increment is $t = 0.5$, and the temperature is $T = 3$. The images, starting from top left and progressing to the right, are from simulation times of 0, 100, 200, 300, 400, 500, 600, and 700. In the nomenclature of Tables 1 and 2, the blue sites are species A, the red are B, and the green are C. The interfacial energies are $E_{AB} = 1$, $E_{AC} = 0.8$, $E_{AO} = 1$, $E_{BC} = 0.8$, $E_{BO} = 1$, and $E_{CO} = 1$.

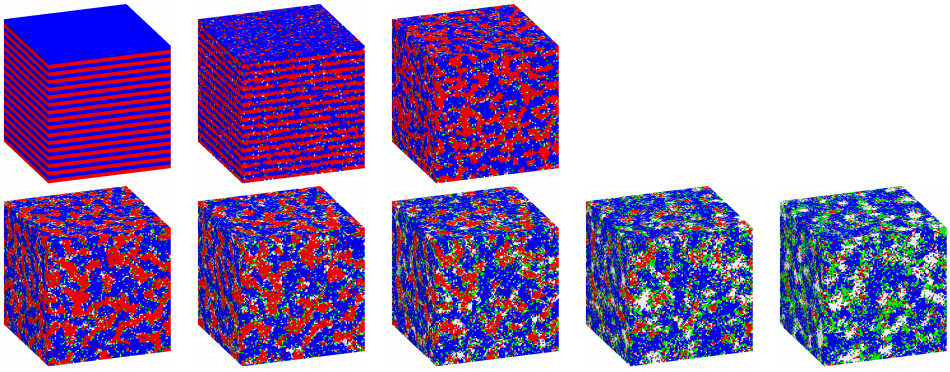

Figure 29. A time progression from a simulation of simultaneous microstructure coarsening, chemical reaction, and pore formation in a layered two-phase material. The simulation grid has 96x96x96 points, the time increment is $t = 0.5$, and the temperature is $T = 3$. The images, starting from top left and progressing to the right, are from simulation times of 0, 100, 200, 300, 400, 500, 600, and 700. In the nomenclature of Tables 1 and 2, the blue sites are species A, the red are B, the green are C, and the white are pores. The interfacial energies are $E_{AB} = 1$, $E_{AC} = 0.8$, $E_{AO} = 0.8$, $E_{BC} = 0.8$, $E_{BO} = 0.8$, and $E_{CO} = 1$.

3.2 Transport Efficiency

The results in Figure 26 and Figure 27 demonstrate the effect of diffusion on microstructural evolution. We will now examine the effect of microstructure on diffusion. A principal interest in modeling the microstructural evolution of layered two-phase structures is due to the influence that it has on the transport of species responsible for work function reduction. For example, in a material containing layers of tungsten and a barium-containing oxide where the chemical reaction between the two produces mobile barium that diffuses to the surface and enables the reduction of the work function, it is important that the mobile barium be able to efficiently diffuse from inside the film to its surface.

To examine the effects of microstructure on transport efficiency, we compute the relative flux of an arbitrary (i.e. fictitious) diffusing species through microstructures taken from the evolution simulations. Since diffusion along interfaces is likely the dominant transport path in reality, it is important to resolve the interfaces explicitly in the model. Therefore, rather than performing diffusion calculations on the same grids used for the microstructural evolution simulations, we rediscretize the microstructures by placing grid points at the corners, rather than the centers, of the microstructures' lattice sites. Since the interfaces in the microstructures lie along the faces of the (cubic) lattice sites in the evolution simulations, the same interfaces will lie directly on the rediscretized grid points in the diffusion calculations.

To compute the diffusional flux through a complex microstructure, we first assign diffusivities to all the possible transport paths. These include single-phase solid, solid/solid interfaces, and solid/pore interfaces. Using these microstructure-dependent diffusivities, the steady-state fluxes and concentrations at every grid in the (rediscretized) microstructure are computed by solving the Laplace equation,

$$\nabla\left(D\nabla C\right) = 0\,, \tag{5}$$

where D is the diffusivity and C is the concentration. This is accomplished by solving Eq 5 in matrix form, with all the grid points on the $-z$ face of the lattice maintained at a concentration of $C = 0$, and those on the $+z$ face at $C = 1$.

Figure 30 contains an example of a diffusion calculation in a polycrystal, with diffusion allowed only along the grain boundaries. Figure 31 shows the fluxes as functions of pore concentration for both a single-phase porous microstructure, and a single-phase porous polycrystal. When the diffusivity along pore walls is much larger than the diffusivity through the bulk, as in the red curve in Figure 31a, the flux is maximized when pore wall paths are maximally percolated through the structure, i.e. at 50% pore concentration. However, if the diffusivity along pore walls is not much larger than the diffusivity through the bulk, as in the blue curve in Figure 31a, then the increase in high-diffusivity paths introduced by the pores is offset by the concomitant removal of bulk diffusion paths, and the flux decreases monotonically with increasing pore concentration. The cases plotted in Figure 31b are similar to the red curve of Figure 31a, except that grain boundaries are present, and it is clear that the size of the grains has only a minor effect on the flux because the diffusivity along grain boundaries is not relatively high. Figure 32 contains plots of flux in an evolving two-phase microstructure started from an initially random distribution of small second-phase particles, with diffusion allowed only along the interfaces. In Figure 32a, the flux decreases with time as the phases coarsen because the surface to volume ratio decreases on average as does the total area of two-phase interfaces (which are the only diffusion paths). In Figure 32b, at low second-phase concentrations, there are not enough interfaces to percolate the microstructure and thus the flux is zero. As suggested in Figure 32a, the flux increases with the concentration of the second phase in Figure 32b simply because the total interfacial area increases. Figure 33 shows similar calculations but with an initially layered structure like the one in Figure 24. At later times, the curves in Figure 33 resemble those in Figure 32a. However, since the high-diffusivity paths are along the two-phase interfaces, and these do not percolate the structure until the layers have broken and evolved sufficiently, the flux

starts low and rises to a maximum as the microstructure evolves and rapid transport paths are formed. (See Figure 24 for a pictorial example of this.)

These results demonstrate some basic behaviors of diffusion through complex microstructures. First, when the interfacial area of high-diffusivity paths is enough to percolate the microstructure, as in Figure 32a, then in a system with "well-distributed" features (i.e. not regular as in a layered structure), the finer the microstructural features the higher the diffusional flux. Clearly, however, there must exist continuous diffusion paths through the microstructure in order for the flux to be nonzero, and thus a layered microstructure where the interfaces are the high-diffusivity paths yields low flux until it coarsens enough to percolate through the entire structure, as in Figure 33. Second, since the flux is approximately proportional to the total area of interconnected high-diffusivity pathways, the flux is generally maximized in two-phase systems (including porous microstructures) when the concentrations of the phases are equal. Though this diffusion model is not material-specific and was applied to idealized microstructures, it can nonetheless provide insights into generalities and trends in the transport efficiency of species diffusing through complex microstructures.

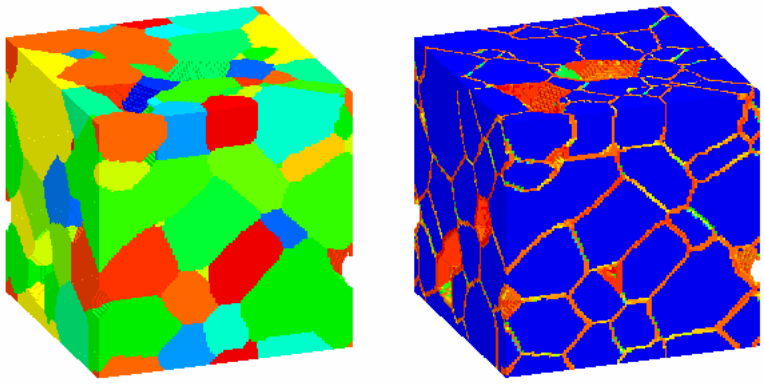

Figure 30. Images of a) a porous polycrystalline microstructure and b) the flux of a diffusing species through it. Diffusion was allowed only along grain boundaries. The colors in image a) merely distinguish the different grains. The blue in image b) is zero flux, red is high flux, and green is in between.

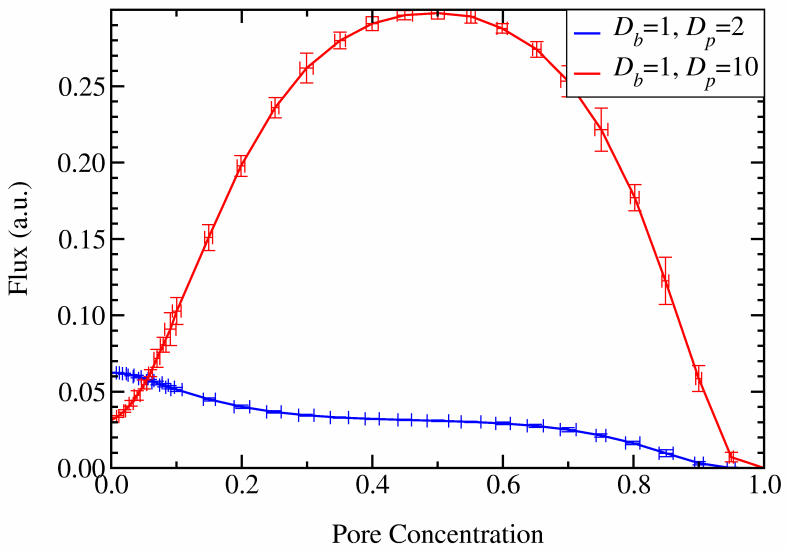

(a)

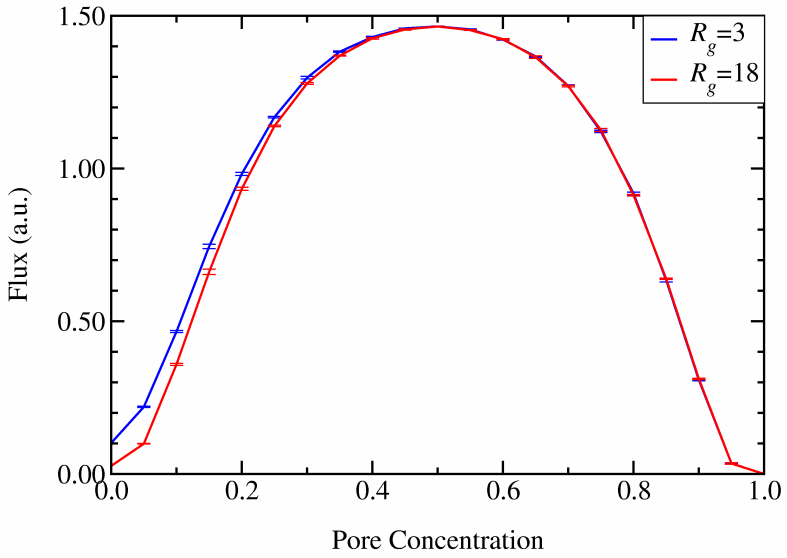

(b)

Figure 31. Microstructure-dependent fluxes as functions of pore concentration through a) porous microstructures and b) porous polycrystalline microstructures. The microstructure contains 64x64x64 grid points, and the diffusion calculation contains 65x65x65. The symbol D_b denotes diffusivity through the bulk, D_p is diffusivity along pore walls, D_g is diffusivity along grain boundaries, and R_g is the average grain radius. The diffusivities in plot (b) are D_b=1, D_g=10, and D_p=100. Error bars represent standard deviations over multiple equivalent simulations started from different initial conditions.

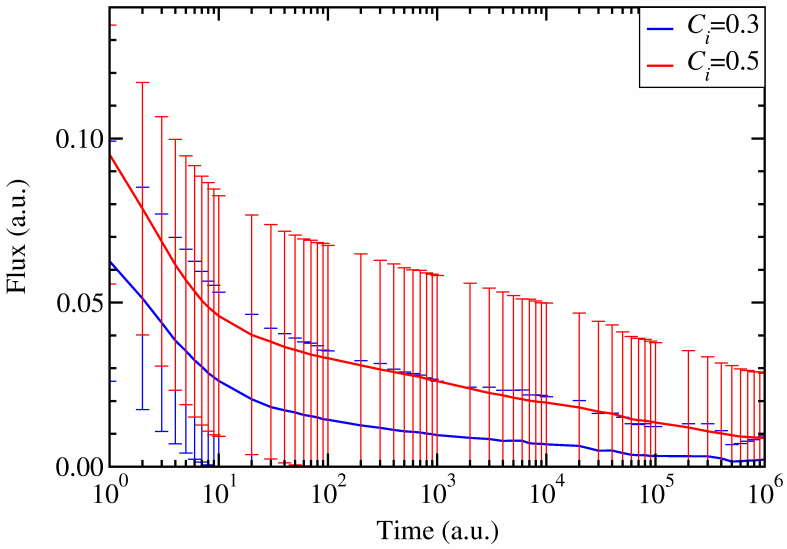

(a)

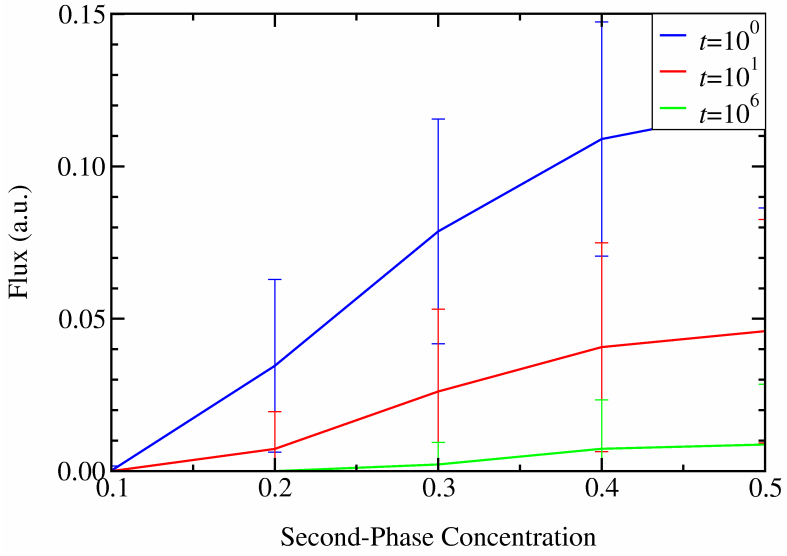

(b)

Figure 32. Microstructure-dependent fluxes as functions of a) time and b) second-phase concentration in an evolving two-phase microstructure started from an initially random distribution of small second-phase particles. The microstructure contains 64x64x64 grid points, and the diffusion calculation contains 65x65x65. The symbol C_i denotes second-phase concentration, and t is time. Diffusion was allowed only along two-phase interfaces. Error bars represent standard deviations over multiple parallel lattice planes in the simulated microstructures.

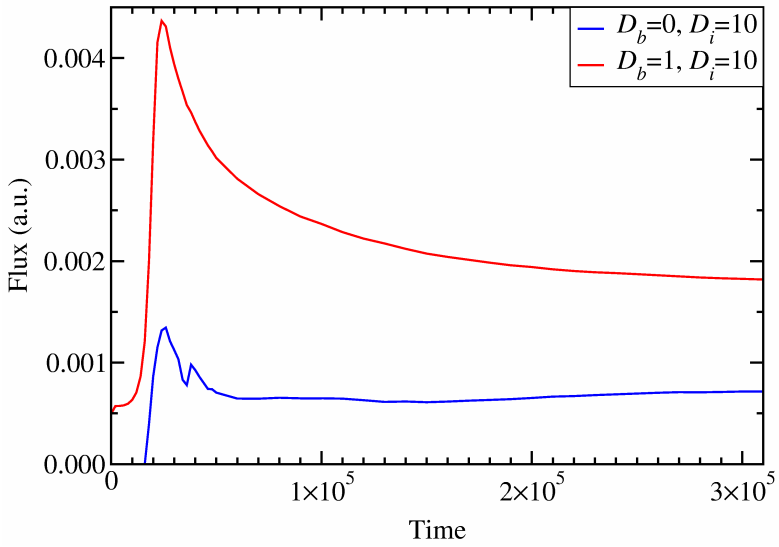

Figure 33. Microstructure-dependent fluxes as functions of a) time and b) second-phase concentration in an evolving two-phase microstructure started from an initially layered structure. The microstructure contains 200x200x200 grid points, and the diffusion calculation contains 201x201x201. The symbol D_b denotes diffusivity through the bulk and D_i is diffusivity along two-phase interfaces.

4. Surface Structure Modelling

There has been no systematic theoretical study of Ba alone or together with O and/or Sr on W surfaces. In principle, very complex structures could occur which are beyond the scope of this project. However, it was noted that an excellent "fit" occurs at the interface between BaO and W(100). This should result in large areas of a commensurate structure that are amenable to computation.

First, it was necessary to find a computer code that reproduces closely the work functions of clean W. Fortunately, the SeqQuest code of Peter Schultz, (Organization 9235), was found to reproduce the experimental work functions of both W(100) and W(110) to within about 0.1 eV. It was necessary though to supplement the Gaussian bases by optimized (as determined by total energy) "floating" s and p orbitals, which sit at the location of the missing row of W atoms above the real surface.

This code was then used to study W(100) with a variety of adsorbates. Because of the much larger metallic radius of Ba than W, only about ½ monolayer (ML) of metallic Ba (meaning one Ba for every two surface W atoms) can be accommodated. A rather large work function (ϕ) was found for both ½ and ¼ ML of Ba vs. experimental emitters (see Table I in Appendix A). This suggests that the presence of Sr and/or O is necessary to obtain the greatly reduced ϕ that is observed.

Computations were then done with many variations in the geometry of BaO and or SrO. First, it was very surprisingly found that 1 ML of BaO has essentially the *same* ϕ as ½ ML of metallic Ba. It was then found that when SrO is mixed with BaO, the preferred structure by a wide margin is BaO/SrO/W(100), in agreement with experiment (see Ref. [12] in Appendix A). However, this structure still has a relative high value for ϕ.

It was noted that the BaO/SrO on W(100) has a stable rocksalt structure (see Fig 1 in Appendix A). Here, each Ba is above an O, and each Sr under an O, with the SrO layer atoms occupying each square hollow in the topmost W(100) layer. It was noted that the W metal relaxes insignificantly to the presence of any of these adsorbates.

Still failing to find a low ϕ structure, the series BaO/SrO, BaO/YO, and BaO/LaO were explored on W(100). It was found that with La present, it is indeed possible to obtain a work function of 1.3 V, close to the lowest that is observed. This surface structure may be difficult to synthesize though since precisely ½ ML of La and Ba need to be deposited.

Finally, 2 ML of BaO was studied. It was found that this material also has the observed low ϕ of 1.3 V and the rocksalt structure makes it very stable. It is suggested, therefore in conclusion, that 1 ML of BaO does *not exist* in nature. If ½ ML of Ba is oxidized on W(100), it is predicted that 2 ML islands of BaO/BaO/W(100) will form.

Since the presence of Sr has not been found to lower ϕ, it is suggested that with mixed metal emitters, the fully oxidized compound, Sr_2O_3, forms a capping layer on two or more ML of BaO, thus protecting it somewhat from ion bombardment.

For basic research, what is most interesting is that ½ ML of Ba and 1 ML of BaO have the same work functions. This seems to violate the normal models for work function reduction by an adsorbate, where surface dipoles of electropositive/negative species decrease/increase ϕ. However, BaO is a highly ionic layer and can well be viewed as nearly $Ba^{2+}O^{2-}$. Therefore, further work is almost complete in which both the surface potentials and the electron density differences between W(100), Ba(½ ML), and BaO(1ML) separately and together as Ba(½ ML)/W(100) and BaO(1 ML)/W(100) are being studied. This will soon result in a subsequent and potentially important publication.

Finally, to check the theoretical results, it is suggested that surface science experiments be made on the system BaO/W(100). These could include not only work function measurements on 1 ML of deposited then oxidized Ba, but also scanning tunneling or atomic force microscopic studies to look for the predicted island formation.

5. Diode Modeling

5.1 Electron Emission Phenomena

In this section, the phenomena of thermionic emission mechanisms from a hot surface are reviewed.

5.1.1 Thermionic Emission from Metals

Thermionic emission depends on emission of electrons from a hot surface. Valence electrons at room temperature within a metal are free to move within the atomic lattice, but very few electrons can escape from the metal surface. The electrons are prevented from escaping by the electrostatic image force between the electron and the metal surface. Heating an emission surface to an appropriate temperature gives some electrons sufficient kinetic energy to overcome the electrostatic image force. As the emitting surface temperature is increased, the number of electrons with sufficient energy to escape the surface increases as well. The energy barrier due to the image force is equal to the difference between the Fermi energy level of the emitter and the electron's potential in vacuum and is referred to as the material work function.

Richardson (1912) first reported the emission current density, J (A/cm^2), as a function of the emitter absolute temperature, T (K), and work function, ϕ (eV)

$$J = AT^2 \exp(-\phi / kT) \tag{1}$$

where A is the Richardson-Dushman constant (120 A/cm^2-K^2) and k is the Boltzmann constant (eV/K). Equation 1 represents the maximum current density that can be emitted from an electrode at temperature T and is often referred to as the saturation emission current density.

When A and ϕ are measured experimentally, the value of A is rarely measured to be 120. Experiments indicate that the work function may not be independent of temperature but has a small temperature coefficient. The work function would then be expressed as

$$\phi = \phi_0 + \alpha T \tag{2}$$

where ϕ_0 (eV) is the work function at absolute zero and α (eV/K) is the temperature coefficient of change in work function. Measurements of α for tungsten indicate a value of 10^{-5} eV/K (Hutson 1955). Substitution of equation 2 into equation 1 yields

$$J = A \cdot \exp\left(-\left(\alpha T\right)/kT\right) \cdot T^2 \cdot \exp\left(-\phi_0/kT\right) = A^* \cdot T^2 \cdot \exp\left(-\phi_0/kT\right), \tag{3}$$

where A^* is often referred to as the effective Richardson-Dushman constant. The measurement of A^* can be difficult; a small error in measuring T can result in a large error in A^*. When the work function increases with temperature, α is positive and A^* is smaller than A. Conversely, if α is negative, A^* is larger than A. Table 2 lists work functions and effective Richardson-Dushman constants for metals typically used in thermionic electrodes (Wright 1953).

The uncertainty of A is not only due to the variation of work function with respect to temperature. Non-uniform surfaces such as polycrystalline materials may hinder the evaluation of A and the work function as well. The work function of polycrystalline materials will vary across the surface. The exponential dependence of emission on work function then implies that emission is not emanating from the entire surface resulting in a smaller predicted value of A^* compared to 120. Also, for single crystal emitters, the true surface of emission, when considered on an atomic or microscopic level, may not equal the perceived macroscopic emission area.

Table 2. Work functions and effective Richardson-Dushman constants for metals typically used in thermionic electrodes (Wright 1953).

Metal	A^* ($A\ cm^{-2}\ K^{-2}$)	(eV)
Molybdenum	55	4.27
Nickel	30	4.84
Platinum	32	5.29
Tantalum	37	4.12
Tungsten	70	4.50

The effect of electron reflection is not included in all derivations. When approaching the surface internally, the electron does have a probability, r, of being reflected at the energy barrier (Beck 1966). When the electron stream is reflected, (1-r) times the number of electrons will be emitted. The variable r is also known as the reflection coefficient. Following the same derivation as noted above, the Richardson Dushman equation may be written as

$$J = A^* \cdot (1-r) \cdot T^2 \cdot \exp\left(-\phi_0 / kT\right) \quad . \tag{4}$$

For many metals, the reflection coefficient is often less than 0.1 and is often neglected considering the other uncertainties mentioned above (Kettani 1970).

5.1.2 Schottky Emission

The Richardson-Dushman equation implies that a maximum current density is achieved if A, ϕ, and T are truly known. When an external field is applied, the current density does increase beyond that predicted by the Richardson-Dushman equation. Figure 34 illustrates the image potential energy and the potential energy (qEx) due to an external field, *E*, applied at the emitter surface.

The term, $\Delta\phi$, represents the lowering of the work function due to a field applied to the surface and is also referred to as the Schottky effect. The Richardson-Dushman equation can now be modified to account for the Schottky effect and is given by

$$J = A^* \cdot T^2 \cdot \exp\left[-\left(\phi - \Delta\phi\right)/kT\right]. \tag{5}$$

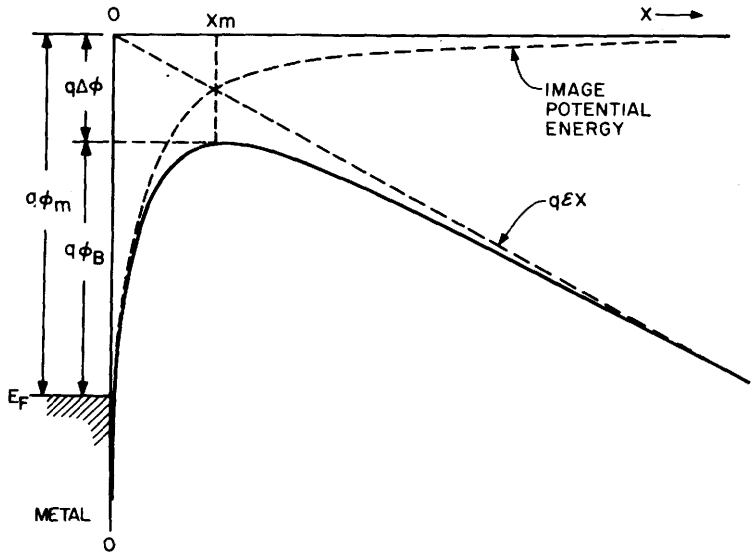

Figure 34. Energy levels experienced by an electron thermionically emitted from a surface with an external electric field applied at the surface (Sze 1981).

The solution of $\Delta\phi$ in terms of the applied field and material properties is given by

$$\Delta\phi = \left[\frac{eE}{4\pi\varepsilon_0}\right]^{1/2} \tag{6}$$

5.1.3 Semiconductor thermionic emission

Semiconductors can be used as thermionic emitters as well as metals. The work function term, ϕ, in the Richardson-Dushman equation can be expressed as

$$\phi = E_a - E_f \tag{7}$$

where E_a and E_f are the vacuum and Fermi energy levels. The conduction band energy level, E_c, may be included in equation 7 as

$$\phi = (E_a - E_c) - (E_f - E_c). \tag{8}$$

From Sze (1994), we obtain

$$J = A\left(N_D / N_{DS}\right) \cdot T^2 \cdot \exp\left(-\phi / kT\right), \tag{9}$$

where N_D is the dopant concentration (cm^{-3}) and N_{DS} is the density of state function.

This derivation has assumed that the position of the bottom of the conduction band is constant throughout the material. The presence of surface states could pin the Fermi level at a distance from the conduction band that is quite different from the distance between the Fermi level and conduction band in the bulk of the semiconductor material.

The image force of an electron emitted from a dielectric is not equal to the charge of the electron as for the case of emission from a metal surface (Morgulis 1947, Herrmann 1951, Wright 1952). The induced electrical charge is obtained by multiplying the electronic charge of equation 6 by the factor, α_S, given by

$$\alpha_S = (\varepsilon_S - 1)/(\varepsilon_S + 1), \tag{10}$$

where ε_S is the dielectric constant. For the alkaline earth oxides used in this work, the square root of α_S is approximately 0.91.

A field applied to the surface of an oxide or semiconductor may reduce the internal work function by an amount, δV_F (Wright 1952). The semiconductor has a limited concentration of free electrons compared to a metal, and an external electric field may not be screened at the surface. The field penetrates into the surface, forms a space charge region, and bends the conduction band with respect to the Fermi level. This effect is shown in Figure 35.

δV_F is given by

$$\delta V_F = (2kT/e) \cdot \arcsin h\left((eE/2\varepsilon_r)\sqrt{\varepsilon_S/2n_0e^2kT}\right), \tag{11}$$

where E is the field at the surface. Equation 11 states that the internal work function will continue to decrease as the field increases and that a large free electron concentration, n_0, will negate the effect of the surface field.

Raju (1994) modified Wright's work by assuming the oxide layer to be a thin film with a thickness, d_f. Raju's calculated reduction in internal work function, δV_r, is related to δV_F by the relation

$$\sinh(e\delta V_r/2kT)/\sinh(e\delta V_F/2kT) = \tanh(d_f/L). \tag{12}$$

5.1.4 Patch Effects

Few thermionic emitters are uniform in material properties across their surfaces. In fact, most emitters are quite inhomogeneous and have patches (two or more) of varying work functions distributed across the surface. When two materials of different work functions but equal temperatures are in contact, electrostatic fields are present among the patches. This effect is illustrated in Figure 36. When no external field is applied to the patchy emitter surface and at a small distance above the patchy emitter, the electrostatic field generated by the patch effect causes the emitter to exhibit an effective

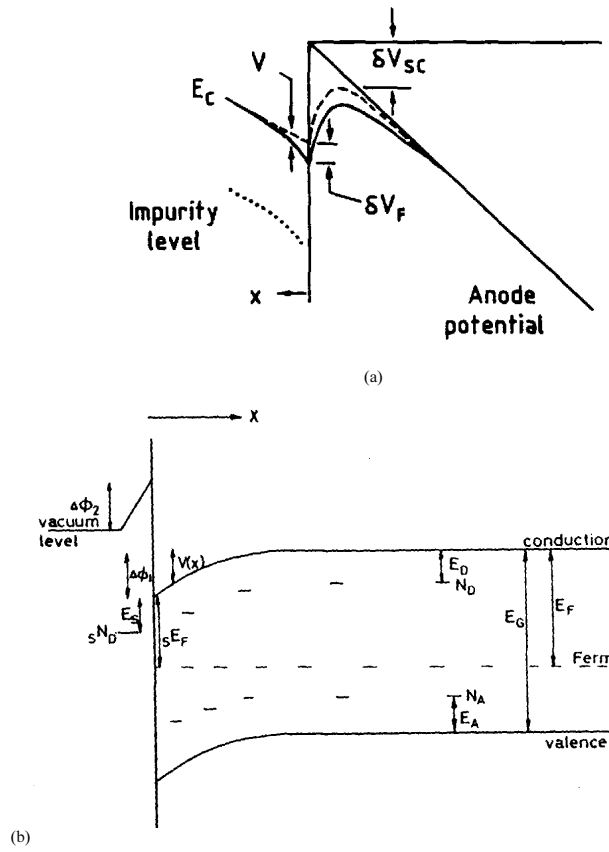

Figure 35. External field intrusion into a semiconductor.

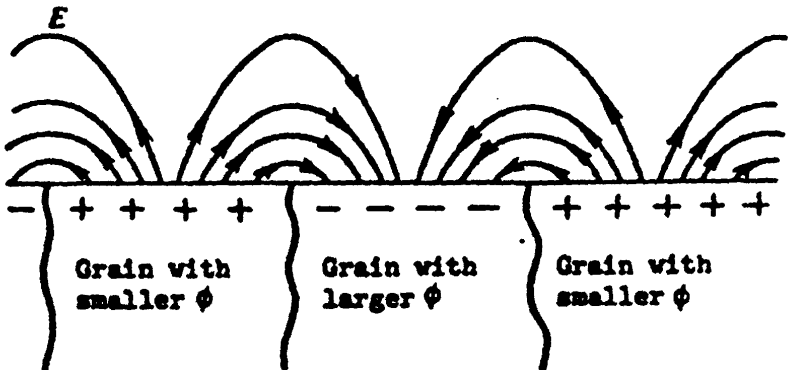

Figure 36. Electrostatic fields generated by surface patch effects (Baksht 1978).

work function that is an area average of both patches. The effective work function , ϕ_e, is given by (Herring 1949)

$$\phi_e = \sum_i f_i \phi_i \,, \tag{13}$$

where f_i is the area fraction of each individual patch, ϕ_i . Figure 37 illustrates the patch effect for an emitter surface with two patches of equal area fraction and with no field applied to the emitter surface. The patch work functions are 1.1 and 1.8 eV. The patch effect adversely affects the low work function patch because of the field effect from the neighboring high work function patch; an electron traveling normal to and away from the low work function patch must climb a 0.35 eV hill. The electrons emitted from the high work function patch are not adversely affected to first order; these electrons still must overcome a 1.8 eV barrier. The effective work function becomes1.45 eV, as governed by equation 13, at a distance of approximately $4x10^{-4}$ cm from the emitter surface.

Figure 38 illustrates the two-patch surface when an accelerating field of 500 V/cm is applied to the emitter surface. The Schottky effect due to the 500 V/cm accelerating bias decreases the work function immediately in front of the high patch from 1.8 eV to 1.76 eV. The energy barrier in front of the low work function patch is also decreased by the accelerating field (dropping from 1.45 eV at zero bias to 1.31 eV). As the accelerating field is increased, the potential energy barrier in front of the low work function patch will cease to exist. Figure 39 shows the effect of a decelerating field (also 500 V/cm) on the two patch surface. In this case, the potential due to the decelerating field presents a larger barrier to the electron emission than the individual patch work functions.

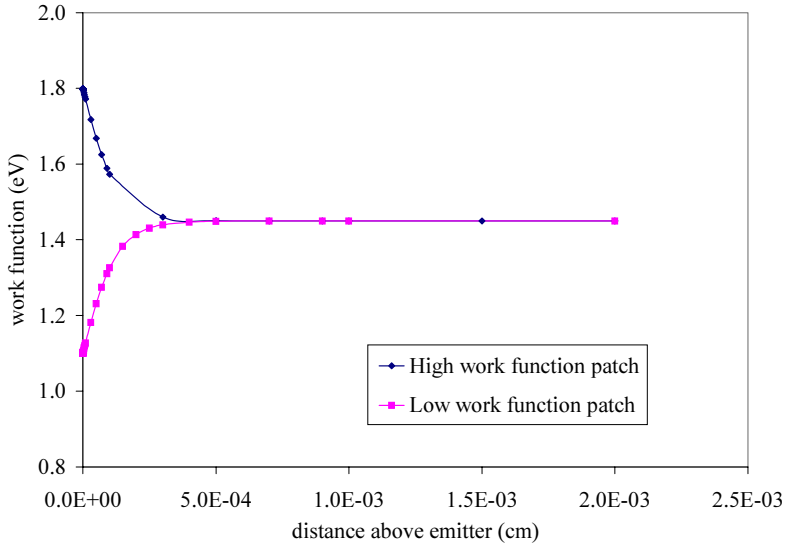

Figure 37. The effective work function above an emitting surface with two patches of equal area fraction and with no applied electric field.

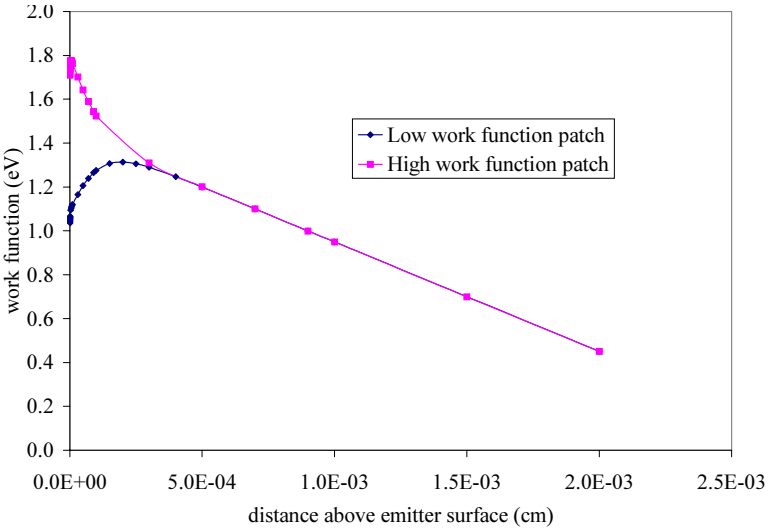

Figure 38. The effective work function above an emitting surface with two patches of equal area fraction and with an applied accelerating electric field of 500 V/cm.

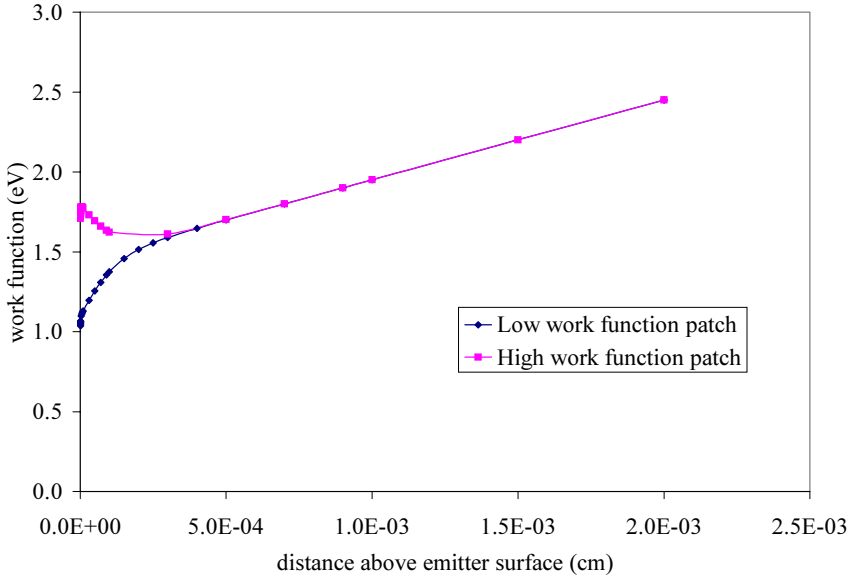

Figure 39. The effective work function above an emitting surface with two patches of equal area fraction with an applied decelerating electric field of 500 V/cm.

5.2 Ideal Vacuum Thermionic Converters

When two electrodes are placed in proximity, the electron will experience a potential profile through the gap when traveling from the emitter to the collector. In this chapter, the ideal vacuum converter analysis of the interelectrode potential profile neglects the space charge effect of one electron on its neighbor electrons; this case represents an idealized condition of electron transport through the gap between the electrodes.

The interelectrode potential profile for three electrode pair combinations is illustrated in Figure 40. For the three conditions, the emitter work function, ϕ_E, may be less than (case a), equal to (case b), or greater than (case c) the collector work function, ϕ_C. The positive y-axis, ψ, represents increasing (or positive) electron energy and decreasing (or negative) voltage. Because both electrodes are connected externally through a load, the Fermi level of the emitter, μ_E, is at the same level as the Fermi level of the collector, μ_C. Since space charge is neglected, the interelectrode potential energy from emitter to collector is linear. ψ_E and ψ_C are the emitter and collector potential energies and are related to the emitter and collector Fermi levels and work functions by the following identities

$$\psi_E = \phi_E + \mu_E \tag{14}$$

and

$$\psi_C = \phi_C + \mu_C . \tag{15}$$

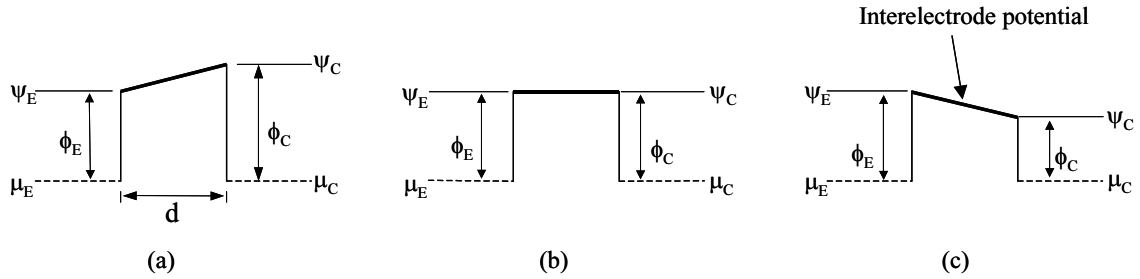

Figure 40. The interelectrode potential profile for three cases of electrode work functions

In the vacuum thermionic converter, the interelectrode potential energy is governed by Poisson's equation. Solving Poisson's equation, the electric field, *E*, in the interelectrode gap is given by

$$E = d\psi/dz = -(\psi_E - \psi_C)/d \ . \tag{16}$$

The force, F, on an electron due to the electric field in the interelectrode gap is then equal to

$$F = eE = -e(\psi_E - \psi_C)/d \, . \tag{17}$$

For the case of $\psi_E > \psi_C$, an electron in the gap will be accelerated from the emitter to the collector. For the case of $\psi_E = \psi_C$, an electron in the gap will not experience deceleration or acceleration forces and will travel from the emitter to the collector if it has an initial velocity toward the collector. For both cases, all of the electrons leaving the emitter will arrive at the collector. For the case of $\psi_E < \psi_C$, an electron in the gap traveling from the emitter toward the collector will experience a decelerating force. Not all electrons leaving the emitter will have sufficient energy to reach the collector.

When the emitter is heated and the collector is cooled, electrons leaving the emitter can arrive at the collector for cases b and c with a magnitude equal to the saturation current density, J_{ES},

described by the Richardson-Dushman Equation with the emitter work function, ϕ_E, and temperature, T_E:

$$J_{ES} = A \cdot T_E^2 \cdot \exp\left(-\phi_E / kT_E\right). \tag{18}$$

When considering case a, fewer electrons will arrive at the collector than leave the emitter as described by equation 18. The decrease in current density occurs because the barrier to thermionic emission as seen by electrons leaving the emitter now includes the effect of the collector. For case a, the Richardson-Dushman equation may be written as

$$J_{EC} = A \cdot T_E^{\,2} \cdot \exp\left(-\phi_C / kT_E\right), \tag{19}$$

where J_{EC} (A/cm^2) is the current density from the emitter to collector, T_E (K) is the emitter temperature, and ϕ_C (eV) is the collector work function. The collector work function can be related to the emitter work function by

$$\phi_C = \psi_C - \psi_E + \phi_E \ . \tag{20}$$

Substituting equation 20 into 19 yields

$$J_{EC} = J_{ES} \cdot \exp\left(-\left(\psi_C - \psi_E\right)/kT_E\right) . \tag{21}$$

The current density, J_{EC}, is a fraction of the emitter saturation current density, J_{ES}.

As a first observation, a thermionic converter should, at a minimum, have an emitter work function equal to the collector work function and, at best, have the emitter work function greater than the collector work function. Fabricating a vacuum converter with an emitter work function less than the collector work function would be the worst case scenario.

The converter current can be changed by applying a voltage across the thermionic converter leads. The load that is driven by the thermionic converter can be used to adjust the voltage across the converter by changing its resistance, which in turn, controls the current flowing through the converter. Figure 41 illustrates the energy profile of a thermionic converter that has a voltage bias, V, applied across its output leads for the case where the emitter work function is greater than the collector work function. Since the positive ψ direction represents increasing electron energy, the collector is negatively biased with respect to the emitter.

Appropriately biasing the converter results in three general cases that relate the electrode output voltage to ψ_E and ψ_C. These three cases are illustrated in Figure 42. In this figure, the emitter work function is greater than the collector work function. In cases (a) and (b), the emitter electron potential energy, $\psi_E = \phi_E + \mu_E$, is greater than or equal to the collector electron potential energy, $\psi_C = \phi_C + eV + \mu_E$. In case (c), the emitter electron potential energy is less than the collector electron potential energy. These three cases can also be realized for a converter in which the emitter and collector work functions are equal, or in a converter in which the emitter work function is less than the collector work function.

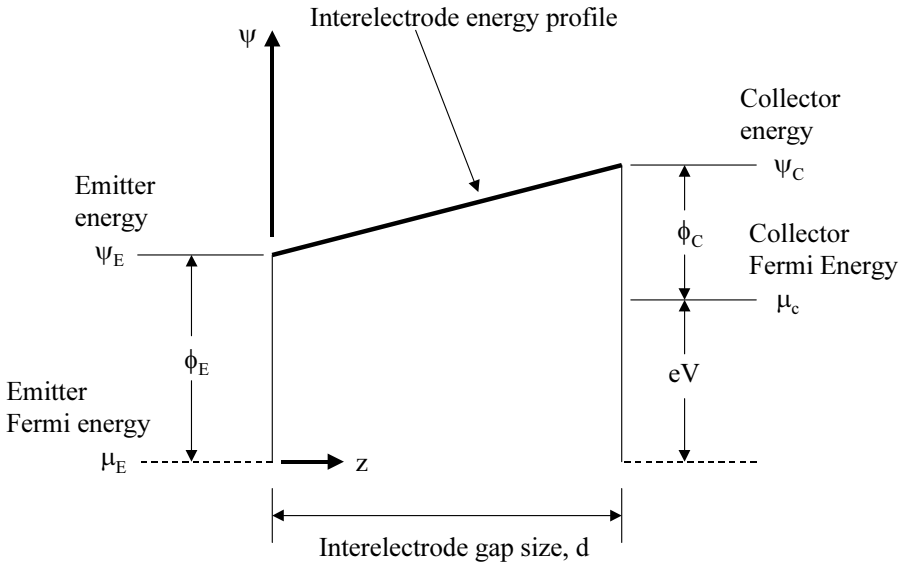

Figure 41. The energy profile of a thermionic converter with an applied voltage bias.

Figure 43 shows the ideal current-voltage characteristic for a thermionic converter with a heated emitter and its collector maintained at absolute zero (the Schottky effect is neglected). This quadrant represents the power production mode. The logarithm of the current density is plotted versus the output voltage. The current is constant and is the saturation current as long as the output voltage is less than (ϕ_E - ϕ_C)/e. This corresponds to case (a) of Figure 42. When the output voltage is greater than (ϕ_E - ϕ_C)/e, the output current density is independent of the emitter work function and decreases exponentially. This corresponds to case (c) in Figure 42. The knee of the curve (where $V = V_0 = [\phi_E - \phi_C]/e$) corresponds to case (b).

The current density, J, in the interelectrode gap is the difference of the current density, J_{EC}, that is emitted from the emitter and flows to the collector and the current density, J_{CE}, that is emitted from the collector and flows to the emitter. As an equation, J is given by

$$J = J_{EC} - J_{CE}. \tag{22}$$

Equation 22 assumes that no space charge, patch, or reflection effects occur; it is an ideal case.

For a thermionic converter with emission from the collector and emitter, the current-voltage relation is given by

$$J = A \cdot T_E^2 \cdot \exp\left(-\phi_E / kT_E\right) - A \cdot T_C^2 \cdot \exp\left(-\left(\phi_E - eV\right)/kT_C\right) \quad \text{for} \quad eV \le \phi_E - \phi_C \tag{23a}$$

$$J = A \cdot T_E^2 \cdot \exp\left(-\left(\phi_C + eV\right)/kT_E\right) - A \cdot T_C^2 \cdot \exp\left(-\phi_C / kT_C\right) \quad \text{for} \quad eV \ge \phi_E - \phi_C \ . \tag{23b}$$

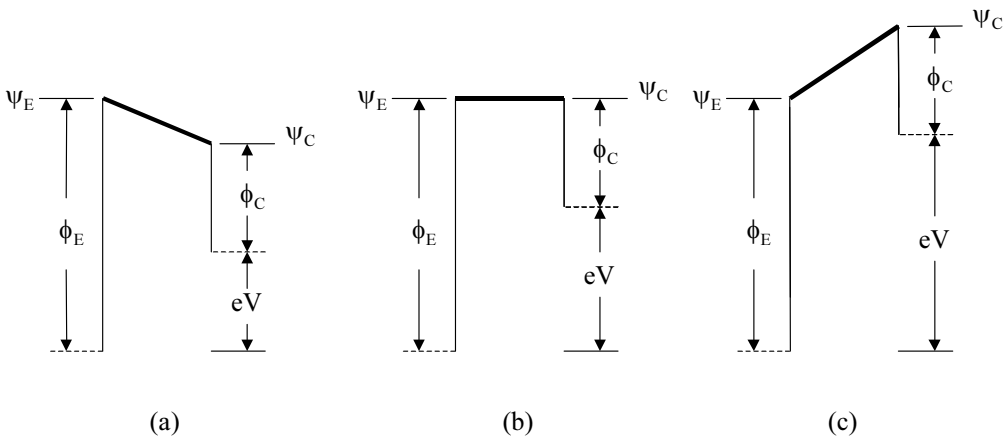

Figure 42. The energy profiles of a thermionic converter with three different applied voltage biases.

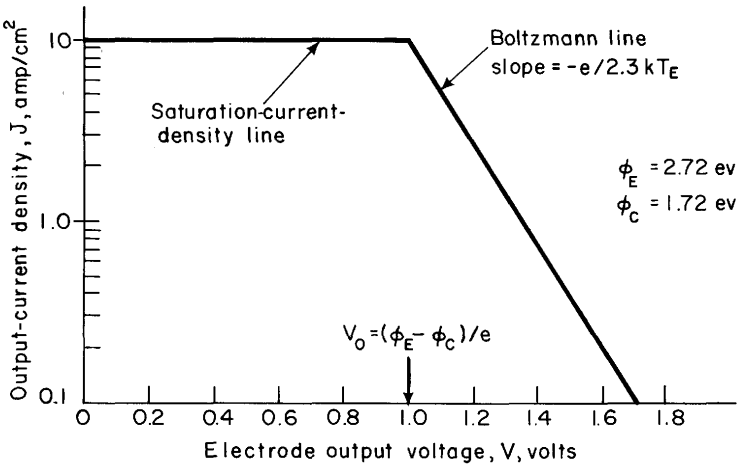

Figure 43. The ideal current-voltage characteristic of a thermionic converter (Hatsopoulos 1973). Operation in this quadrant represents energy production. Back emission from the collector is assumed to be negligible. Schottky emission is neglected.

5.3 The Practical Vacuum Thermionic Converter

In this section, our review of electron transport through the interelectrode gap of the vacuum thermionic converter continues. Space charge effects and the Schottky effect are included, but reflection effects are not yet considered.

5.3.1 Space Charge Effect

In a practical vacuum thermionic converter with interelectrode gaps greater than tens of microns, currents approaching the saturation current are not observed in the power production quadrant. Electrons that are emitted from the emitter produce a space charge in the interelectrode gap

(IEG). For large current densities, the electrons already in transit from emitter to collector form a volume of free negative charge in the gap. This volume of negative charge forms an electric field that will act to repel further emission of electrons and reflect the emitted electrons back to the emitter.

The electric fields generated by the electrons in transit can be calculated by using Poisson's equation. For a one-dimensional application, Poisson's equation is

$$d^2\psi/dz^2 = -e^2 n_e/\varepsilon_0 \,, \tag{24}$$

where ψ is the electron energy, n_e is the electron number density at position z in the interelectrode gap and ε_0 is the vacuum dielectric constant. The second derivative of the electron energy, ψ, is always negative. Therefore, the repelling force on the electron decreases as the electron moves away from the emitter.

5.3.2 Interelectrode Electron Potential Profiles

Figure 44 illustrates five cases of the energy profiles as a function of the converter output voltage. For these cases, the emitter work function is always assumed to be greater than the collector work function.

In Figure 44a, the converter output voltage is very large and negative. Electrons emitted from the emitter see a large energy barrier equal to the sum of the collector work function and converter output voltage energy, $\phi_C + eV$. Electrons emitted from the collector experience an energy barrier equal to ϕ_C. For typical converter operating temperatures, the barrier to the emitter electrons will result in small forward currents that are usually below the space charge limit. The cold collector will also emit very few electrons. If the converter output voltage is increased to very large negative levels, the collector emission will enter the Schottky mode of emission. This operation mode is typically called the retarding mode of operation. The gradient, $d\psi/dx$, of the interelectrode energy is positive from the emitter to the collector, and no maximum of ψ is observed in the gap. The electric field is decelerating to electrons from the emitter and accelerating to electrons from the collector.

As the converter output voltage is decreased, the energy barrier to the emitter electron decreases, and electron emission from the emitter increases. The collector emission remains constant as its emission only depends on T_C and ϕ_C. As the emitter current increases, space charge effects will start at a converter output voltage, V_R, defined as the critical voltage. This operational mode is pictured in Figure 44b. At the critical voltage, the slope of ψ becomes zero at the collector surface. Again, for typical converter operational conditions where the emitter temperature is much greater than the collector temperature, the emitter current is much greater than the collector current. However, if the collector temperature is high enough, a substantial back emission from the collector can occur. At V_R, the converter is defined as operating at the critical point. The critical voltage is given by

$$V_R = \psi_{CR} - \phi_C - \mu_E . \tag{25}$$

As the converter output voltage decreases below the critical voltage, the emission current from the emitter continues to increase and the space charge effect becomes dominant. Figure 44c illustrates this operational mode. The electron energy profile in the gap, as calculated by Poisson's equation, now has a maximum value, ψ_{max}, in the gap that exceeds the energy potential at the emitter, ψ_E, and collector, ψ_C. The slope of ψ is zero at ψ_{max}. ψ_{max} occurs in the gap at position, x_{max}. Electrons from the emitter are decelerated at positions less than x_{max} from the emitter and are accelerated at positions greater than x_{max}. The reverse is true for electrons emitted from the collector. The energy barrier to electrons leaving the emitter is now

$$\left(\psi_{\max} - \psi_E\right) + \phi_E \ , \tag{26}$$

and the energy barrier to the electrons leaving the collector is

$$\left(\psi_{\max} - \psi_C\right) + \phi_C \ . \tag{27}$$

The value of ψ_{max} and its location in the gap depend on ϕ_E, ϕ_C, T_E, T_C, V, and the gap size. As the converter output voltage is decreased, the position of ψ_{max} moves from the collector surface to the emitter surface. This operational range of ψ_{max} is referred to as the space charge limited range of operation.

When the location of ψ_{max} reaches the emitter surface, the converter output voltage is defined as the saturation output voltage , V_S. Figure 44d illustrates this condition. The slope of ψ is defined as zero at the emitter surface. The energy barrier to the electrons in the emitter is equal to ϕ_E , and the current from the emitter is now equal to the emitter saturation current. The energy barrier to electrons emitted from the collector is equal to

$$\left(\psi_E - \psi_C\right) + \phi_C \ . \tag{28}$$

As the converter output voltage is decreased below the saturation voltage, the Schottky effect allows the converter current from the emitter to exceed the emitter saturation current. The converter output current increases proportionally to the square root of the field at the emitter surface. Figure 44e shows this effect. The electric field is accelerating to electrons from the emitter across the entire gap. Emission from the collector is virtually nonexistent.

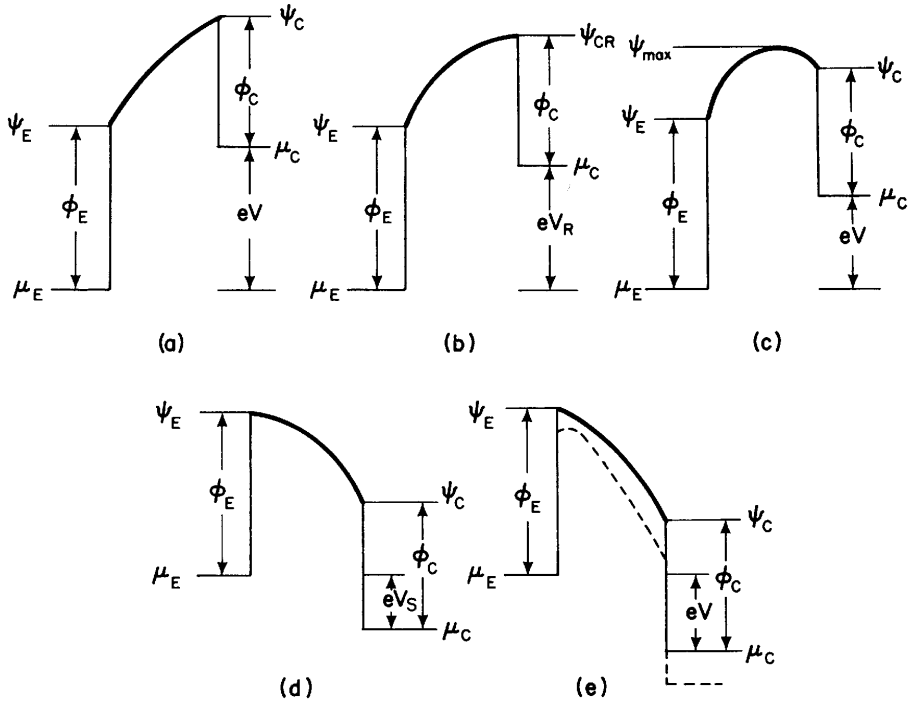

Figure 44. The electron energy distribution in the gap for the five operational modes of a thermionic converter that exhibits space charge (Hatsopoulos 1973).

5.3.3 Practical Converter Voltage-Current Characteristics

Figure 45 shows a calculated output voltage emission current characteristic for a practical thermionic converter designed for negligible back emission from the collector. The operational parameters for this diode calculation are T_E = 1500K, T_C = 500K, ϕ_E = 2.2 eV, ϕ_C = 1.6eV, and d = 0.001 cm. The voltage current characteristic for an ideal diode without space charge and Schottky effect is also presented. The five modes of operation discussed in the section above are also labeled. The power production mode of the converter takes place in quadrant one of Figure 45. Quadrants two and four represent modes of operation where the thermionic converter is consuming power and acts as a traditional vacuum tube diode. In quadrant 2, electron emission from the emitter is dominant. In quadrant 4, electron emission from the collector dominates although it is virtually nonexistent. Depending on the thermionic converter properties and operating conditions, the saturation and critical points may occur in quadrants one or two.

The retarding mode current densities from the emitter and collector, J_{ERM} and J_{CRM}, respectively, are given by

$$J_{ERM} = A \cdot T_E^2 \cdot \exp\left(-\left(\phi_C + eV - e\Delta V_{sch,rm}\right)/kT_E\right) \tag{29}$$

$$J_{CRM} = A \cdot T_C^2 \cdot \exp\left(-\left(\phi_C - e\Delta V_{sch,rm}\right)/kT_C\right), \tag{30}$$

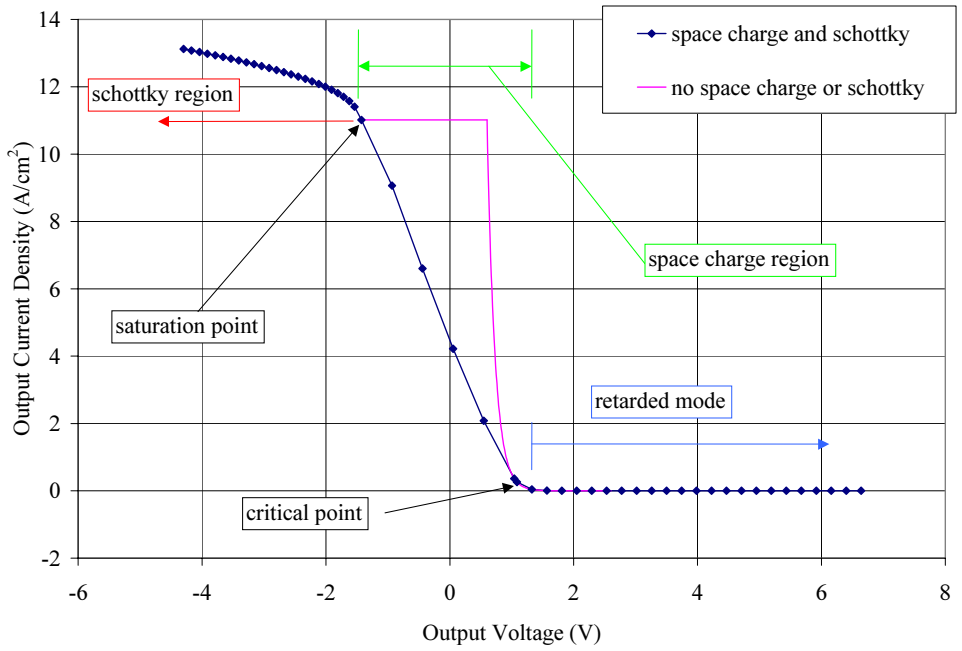

Figure 45. Thermionic converter diode current density output as a function of voltage bias.

for the operating condition, $V > V_R$ and where $\Delta V_{sch,rm}$ is the Schottky effect lowering of the collector work function. At the critical point of operation, the emitter and collector currents, J_{ER} and J_{CR}, are

$$J_{ER} = A \cdot T_E^2 \cdot \exp\left(-\left(\phi_C + eV_R\right)/kT_E\right) \text{ and} \tag{31}$$

$$J_{CR} = A \cdot T_C^2 \cdot \exp\left(-\phi_C/kT_C\right) \text{ for } V_R = \left(\psi_{CR} - \phi_C\right)/e \ . \tag{32}$$

V_R is related to ψ by

$$V_R = \phi_E - \phi_C + \psi_{CR} - \psi_E \, . \tag{33}$$

In the space charge operational mode, the emitter and collector currents, J_{ESC} and J_{CSC}, are

$$J_{ESC} = A \cdot T_E^2 \cdot \exp\left(-\left\{\left(\psi_{\max} - \psi_E\right) + \phi_E\right\}/kT_E\right) \text{ and} \tag{34}$$

$$J_{CSC} = A \cdot T_C^2 \cdot \exp\left(-\left\{\left(\psi_{\max} - \psi_C\right) + \phi_C\right\}/kT_C\right) \text{ for } V_R \le V \le V_S \, . \tag{35}$$

The operational voltage is related to ψ by the expression

$$V = \left(\phi_E - \phi_C + \psi_C - \psi_E\right)/e \ . \tag{36}$$

The saturation mode current densities from the emitter and collector, J_{Esat} and J_{Csat}, respectively, are given by

$$J_{Esat} = A \cdot T_E^2 \cdot \exp\left(-\phi_E / kT_E\right) = A \cdot T_E^2 \cdot \exp\left(-\left\{\psi_E - \psi_C + \phi_C - eV_S\right\}/kT_E\right) \quad (37)$$

and

$$J_{Csat} = A \cdot T_C^2 \cdot \exp\left(-\left\{\psi_E - \psi_C + \phi_C\right\}/kT_E\right). \quad (38)$$

Finally, in the accelerating or Schottky mode of operation, current densities from the emitter and collector, J_{Esch} and J_{Csch}, respectively, are

$$J_{Esch} = A \cdot T_E^2 \cdot \exp\left(-\left\{\phi_E - \Delta V_{sch}\right\}/kT_E\right) \text{ and} \quad (39)$$

$$J_{Csch} = A \cdot T_C^2 \cdot \exp\left(-\left\{\left(\psi_E - \psi_C\right) + \phi_C - \Delta V_{sch}\right\}/kT_C\right), \text{ for } V<V_S. \quad (40)$$

where

$$V = \left(\phi_C - \phi_E + \psi_E - \psi_C\right)/e. \quad (41)$$

In general, equations 29 through 41 cannot be presented in a closed form solution. The current densities can be calculated when ψ_{max}, ψ_E, and ψ_C are known. The Poisson equation must be used to solve for these variables. However, Nottingham (1960) presented a closed form solution of J_R for the special case where J_R is much less than the saturation current density

$$J_R = 7.729x10^{-12}\, T_E^{3/2} / d^2 \ . \quad (42)$$

5.4 Space Charge Effects and Theories

To model the operation of a thermionic converter, the potential energy distribution in the interelectrode space must be calculated. Once the energy distribution is known, the equations of Section 5.3 may be used to calculate the current-voltage characteristics of the diode. The potential energy distribution may be determined by solving Poisson's equation and its applicable boundary conditions. The electron density in the interelectrode space must be known to solve Poisson's equation. The electron density depends on the nature of emission from the emitter and collector as well as the energy values in the gap.

Langmuir (1913) developed one of the first theoretical analyses of the operation of the vacuum thermionic converter. In his work, he assumed collisionless electron transport between two, infinite parallel plates operating in vacuum. Langmuir also assumed that the electrons are emitted with a Maxwellian velocity distribution. His work demonstrated that the electrons travel in an electric field that forms from the applied potential at the electrodes and the distribution of the electrons.

5.4.1 Collisionless Space Charge Analysis

The potential energy distribution in the gap can be determined if the motion of the electrons can be calculated. The transport of electrons from the emitter to collector are caused by forces due to

gradients in the energy potential, electron density, and electron particle temperature. The electron transport requires the simultaneous solution of Maxwell's equations for the electromagnetic field in vacuum and the Boltzmann transport equation. If the magnetic field is assumed to be negligible, Poisson's equation is the only electromagnetic field equation needed.

Poisson's equation ,

$$d^2\psi/dz^2 = -e^2\, n_e(z)/\varepsilon_0 \ , \tag{43}$$

is used to determine the shape of the potential energy profile in the gap (as shown in Figure 46). The electron density, n_e, must be calculated. Therefore, an electron distribution function, $f_e(z,v_e)$, must be determined as a function of position and electron velocity. The integral of the distribution function over all velocities yields the electron density. The electron density must be expressed in terms of f_e, and the distribution function must be expressed in terms of ψ_E. The Boltzmann transport equation is used to solve the electron distribution function.

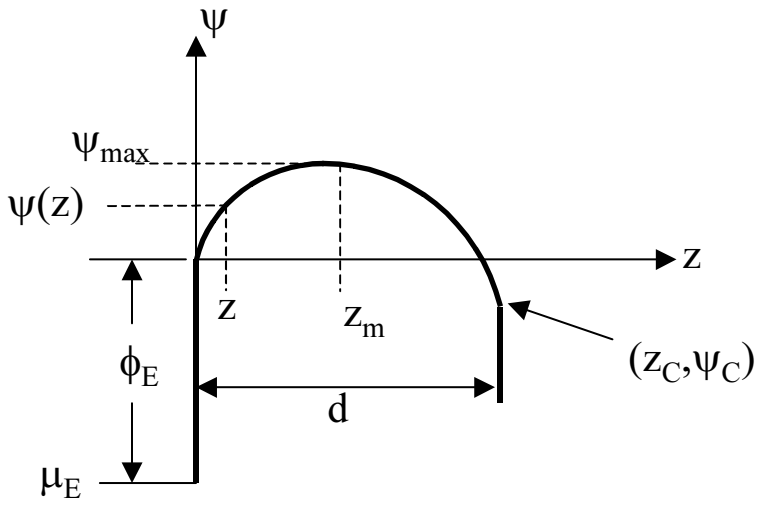

Figure 46. Interelectrode gap potential energy distribution.

Solving the transport equation yields a new version of Poisson's equation to give

$$2\, d^2\gamma/d\xi^2 = \exp(\gamma)\cdot\left[1 \pm erf(\gamma^{1/2})\right] \ \text{for} \ \ \xi \gtrless 0 \ , \tag{44}$$

where dimensionless variables, ξ and γ are given by

$$\gamma = \left(\psi_m - \psi(z)\right)/kT_E \ \text{ and } \ \xi = \left(z - z_m\right)/x_0 \ , \tag{45}$$

where x_0 is described below.

From Figure 46, we can see that the boundary conditions are

$$\gamma = 0 \text{ for } \xi = 0 \text{ and } d\gamma/d\xi = 0 \text{ for } \xi = 0 . \tag{46}$$

Integrating equation 44 then results in

$$\xi = \int_0^{\gamma} \left[\exp(t) - 1 \pm \exp(t) erf\left(t^{1/2}\right) + 2(t/\pi)^{1/2} \right]^{-1/2} dt \text{ for } \xi \gtrless 0 . \tag{47}$$

Figure 47 shows the potential energy barriers in terms of the newly defined dimensionless parameters, ξ and γ. Equation 45 shows that the new ξ-γ coordinate system now has its origin at the peak of the electron potential energy curve in the gap. This location corresponds to (z_m, ψ_{max}) in the old z-ψ coordinate system. The space charge barriers, γ_E and γ_C, as seen from the emitter and collector are now

$$\gamma_E \equiv (\psi_{max} - \psi_E)/kT_E \text{ and } \gamma_C = (\psi_{max} - \psi_C)/kT_E , \tag{48}$$

respectively. The distance of the origin in the $\tilde{\xi}\gamma$ coordinate system to the emitter and collector, ξ_E and ξ_C, in terms of the old x-ψ coordinate system are given by

$$\xi_E = z_E/x_0 \text{ and } \xi_C = z_C/x_0 , \tag{49}$$

respectively. Since $z_E + z_C = d$, we can observe that

$$\xi_E + \xi_C = d/x_0. \tag{50}$$

The term, x_0, represents a normalization distance of the gap size, d. The variable, x_0, is related to the emitter temperature and net current density by

$$x_0 = 1.09x10^{-6} T_E^{3/4}/J^{1/2} . \tag{51}$$

Section 5.10 will review the use of equation 47 to calculate the thermionic converter current.

5.5 Space Charge Theory With Back Emission

The emission current from the collector may be significant for certain vacuum thermionic converter operating conditions when the operating collector temperature is high and/or the collector work function is low. However, these conditions rarely occur for a properly designed converter system. Electron emission from the collector is also known as back emission. Kniazzeh (1959) extended Langmuir's space charge theory to the analysis of the interelectrode potential energies for cases where back emission cannot be neglected. The Boltzmann equation and electron distribution equations are still valid to solve back emission. However, at the maximum potential energy, ψ_{max}, the electron distribution function is the sum of two half Maxwellian distributions. The first is due to the electrons leaving the emitter as discussed above. The second half Maxwellian is due to electron emission from the collector.

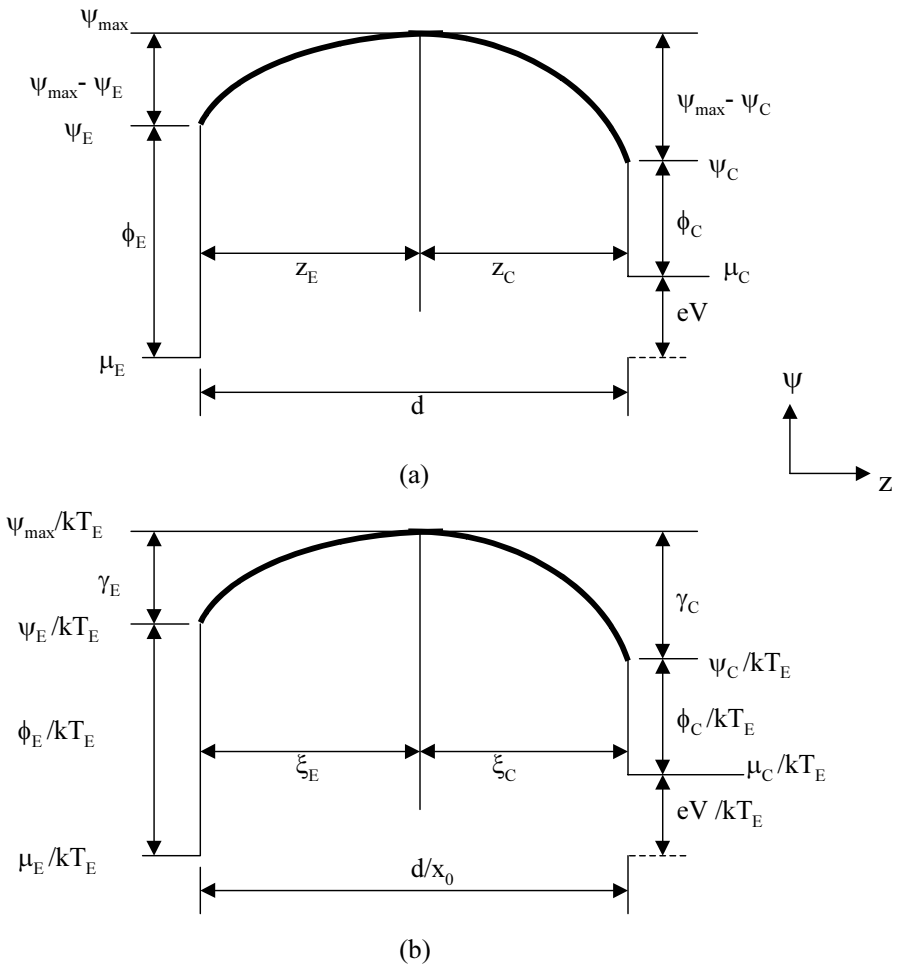

Figure 47. Potential energy diagram (a) and dimensionless energy diagram (b) and nomenclature used for space charge theory.

Poisson's equation for forward and backward emission is then given by

$$\left(d\gamma/d\xi\right)^2 = \exp(\gamma) - 1 \pm \exp(\gamma)erf\left(\sqrt{\gamma}\right) - 2\sqrt{\gamma/\pi} \qquad + \mathrm{B}\left[\exp(\delta\gamma) - 1 \mp \exp(\delta\gamma)erf\left(\sqrt{\delta\gamma}\right) + 2\sqrt{\gamma/\pi}\right]$$

for $\xi \gtrless 0$ where $\delta = T_E/T_C$. (52)

The variable, B, is a voltage reference (Kniazzeh 1959).

5.6 Schottky Emission

As noted in Figure 46, the slope of ψ is zero at z_{max}, and the position of ψ_{max} moves from the collector to the emitter as the converter output voltage is decreased. At the saturation mode of operation, ψ_{max} is exactly located at the emitter surface, and the slope of ψ is also zero at the emitter surface. As the diode voltage is further decreased and the Schottky mode is entered, ψ_{max}

remains at the emitter surface, but the slope of ψ at the emitter surface is no longer zero but is negative. Since the value of γ_0' is no longer zero, we may write the first integral solution of equation 44 as

$$\left(d\gamma/d\xi\right)^2 - \gamma_0'^2 = \exp(\gamma) - 1 - \exp(\gamma)\cdot erf\left(\sqrt{\gamma}\right) + 2(\gamma/\pi)^{1/2} \text{ for } \xi > 0\,. \tag{53}$$

It is also noted that ξ no longer has a positive and negative value but is only positive because the origin of the ξ–γ coordinate system has moved to the emitter surface. The solution of equation 53 yields

$$\gamma = \int_0^{\xi}\left[\gamma_0'^2 + \exp(\gamma) - 1 - \exp(\gamma)\cdot erf\sqrt{\gamma} + 2\sqrt{\gamma/\pi}\right]^{-1/2} d\xi\ . \tag{54}$$

The value of γ_0' is given by

$$\gamma_0' = 653.5\text{x}10^{-6}\cdot \text{T}^{7/4}\cdot \text{j}^{-1/2}\cdot\left[\ln(\text{j}/\text{j}_0)\right], \tag{55}$$

where j_0 is the saturation current density and j is the current density in the Schottky mode (Hasker 1983).

5.7 Electron Reflection Effects in Thermionic Theory

Historically, the cesium vapor thermionic converter community has neglected reflection effects in thermionic emission and conversion applications. However, some anomalies observed in the operation of these converters have caused researchers to conclude that reflection effects may need to be investigated in more detail (Balestra 1978, Rasor 1998). Reflection of electrons internal to the electrode must be considered as well as electrons external to the electrode.

5.7.1 Thermionic Equations Revisited

The vacuum thermionic converter produces a net current current density, J, when the emitter is heated and the collector is cooled. The net current is conventionally predicted as the difference in the emitter current density, J_E, and the collector current density, J_C, and is given by

$$\text{J} = \text{J}_\text{E} - \text{J}_\text{C}\ . \tag{56}$$

The emitter and collector current densities can be obtained from the Richardson-Dushman equation

$$J = A\cdot T^2\cdot\exp\left(-\left(\psi_m - \phi\right)/kT\right)\cdot\exp\left(-\phi/kT\right)\ , \tag{57}$$

where ϕ is the electrode work function, ψ_m is the maximum electron potential energy experienced by the electron from the emitting electrode, T is the electrode temperature, and A is

the Richardson–Dushman constant. The Richardson-Dushman constant is based on material properties and is calculated to be 120 A $cm^{-2}K^{-2}$. However, measured values of the parameters in equation 57 rarely lead to a Richardson-Dushman constant equal to 120. The reduction in A is primarily attributed to electron reflection effects, which leads to A being replaced by an effective Richardson-Dushman constant, A^*, where

$$A^* = A \cdot (1 - \overline{R}) . \tag{58}$$

The quantity, $\overline{R}$, is the average electron reflection coefficient. The average electron reflection coefficient accounts for reflection of electrons arriving at the electrode surface from within the electrode material with energies greater than ψ_m. Some possible reflection mechanisms include two-dimensional diffraction effects, reflection due to forbidden energy bands, reflection due to patchy surfaces, and reflection due to abrupt changes in electrical potentials (Herring and Nichols 1949). Ballestra (1978) and Zollweg (1964) have reported reflection coefficients of up to 70% for electron energies found in converter operation. Herring (1949) also noted that surfaces that internally reflect electrons must also reflect electrons from external sources (such as a second emitting surface) due to quantum symmetry rules. The net current given by equation 56, however, does not allow for external reflection of electrons. The following derivation is used to include external electron reflection in the net current (Marshall 1998). Equation 56 can be rewritten with total emitter and collector current densities, $\tilde{J}_E$ and $\tilde{J}_C$, where $\tilde{J}_E$ and $\tilde{J}_C$ include internal and external electron reflection (or emitted and reflected electrons). $\tilde{J}_E$ and $\tilde{J}_C$ are given by

$$\tilde{J}_E = \overline{D}_E J_E + \overline{R}_E^I \tilde{J}_C \tag{59}$$

and

$$\tilde{J}_C = \overline{D}_C J_C + \overline{R}_C^I \tilde{J}_E , \tag{60}$$

where $\overline{D}$ is the average electron transmission coefficient and is related to $\overline{R}$ by the equation, $\overline{D} = (1 - \overline{R})$. The subscript signifies the electrode with which the coefficient is associated. The superscript, I, signifies that the coefficient with which the superscript is associated is averaged over the spectrum of the total current from the opposite electrode. The absence of a superscript signifies that the coefficient is averaged over the internal spectrum of the electrode specified by the subscript. Using this convention, $\overline{D}_E$, is then the average electron transmission coefficient of the emitter for an electron spectra impinging on the emitter surface from within the emitter (or for an internal electron spectra). $\overline{D}_E^I$ is the average electron transmission coefficient of the emitter for an external electron spectra impinging on the emitter surface from the collector electrode. $\overline{R}_E^I$ is the average electron reflection coefficient of the emitter for an external electron spectra impinging on the emitter surface from the collector electrode. Also, equation 59 states that the total current density from the emitter has two components. The first component, $\overline{D}_E J_E$, is due to internal electrons transmitted through the emitter surface (or emitted from within the emitter). The second component, $\overline{R}_E^I \tilde{J}_C$, is due to the total current density, $\tilde{J}_C$,

incident on the emitter from the collector which is then reflected by the emitter back into the gap; note that $\bar{J}_C$ includes both emitted and reflected electrons at the collector. Equation 60 states a similar concept for the current density from the collector. The terms, J_E and J_C, are now defined as the ideal emission current densities where A is always equal to 120 $A \cdot cm^{-2} \cdot K^{-2}$. Equation 56 can now be written as

$$J = \bar{J}_E - \bar{J}_C . \tag{61}$$

Solving the simultaneous equation set of 59-61 gives the new converter net current density, J, that includes the effect of internal and external electron reflection

$$J = \tau \cdot \left(J_E - \Gamma J_C \right) , \tag{62}$$

where

$$\tau = \overline{D}_E \cdot \overline{D}_C^I \big/ \left(\overline{D}_E^I + \overline{D}_C^I - \overline{D}_E^I \cdot \overline{D}_C^I \right) \text{ and } \Gamma = \overline{D}_C \overline{D}_E^I \big/ \overline{D}_E \overline{D}_C^I . \tag{63}$$

The variable, τ , is defined as the effective diode transmission coefficient. The variable, Γ, is defined as the symmetry index. The product, $\tau\Gamma$, is the effective transmission coefficient of the collector. Traditional thought according to equation 56 states that a cold emitter has no effect on the net current density. Equation 62 now states that a cold collector can have an impact on the net current produced by a vacuum converter when $\overline{D}_C^I$ and $\overline{D}_C$ are less than one. If no electron reflection occurs, all of the transmission coefficients will be equal to one. Under this condition, equation 62 will reduce to equation 56. The transmission variables, $\overline{D}_E$, $\overline{D}_C$, $\overline{D}_E^I$, and $\overline{D}_C^I$, may be determined experimentally or theoretically.

5.7.2 Reflection Effects on Space Charge Calculations

The effect of electron reflection on space charge calculations for two-way thermionic emission was recently derived (Marshall 1998, 2000). Figure 48 illustrates the energy potential profile that an electron must overcome in transit from the emitter to the collector for varying degrees of space charge. Figure 48 shows the linear electron energy profile when no space charge exists and the traditional space charge shape discussed in Section 5.4. An interesting feature of space charge due to reflection effects is that reflection can either decrease or increase space charge in the gap.

Marshall (2000) derived a general equation for space charge that includes the effect of reflection from both the emitter and collector electrodes. In Marshall's derivation, four computational zones were defined. The four zones, shown in Figure 49, include the emitter side below ψ_m, the emitter side above ψ_m, the collector side below ψ_m, and the collector side above ψ_m. Electron movement from zone 1 to zone 2 was assumed to be negligible. The emitter side designates the gap at all positions to the left of ψ_m. The derivation resulted in the following Poisson's equation for space charge with reflection effects for the emitter side of the gap

$$(d\gamma/d\xi)^2 = -\alpha_{E1}\left[\exp(\gamma) - \exp(\gamma)erf\sqrt{\gamma} + 2\sqrt{\gamma/\pi} - 1\right] - \alpha_{E2}\left[2\sqrt{\gamma/\pi} - \exp(\gamma)erf\sqrt{\gamma}\right]$$

$$-\varsigma/\delta\left\{\alpha_{C1}\left[\exp(\gamma\delta) - \exp(\gamma\delta)erf\sqrt{\gamma\delta} + 2\sqrt{\gamma\delta/\pi - 1}\right] - \alpha_{C2}\left[2\sqrt{\gamma\delta/\pi} - \exp(\gamma\delta)erf\sqrt{\gamma\delta}\right]\right\}$$

$$\text{for } \xi < 0\ , \tag{64}$$

where ς is defined as the ratio of the current density from the collector divided by the current density from the emitter at ψ_m and the subscripts refer to the emitter or collector side and zone 1 or zone2. The variables α_{E1}, α_{E2}, α_{C1}, α_{C2} are reflection adjustment factors for the various four zones. Marshall (2000) explored the case in which electron movement from zone 1 to zone 2 was negligible in order to obtain approximate values for the adjustment factors. For this assumption, the reflection adjustment factors are approximated by

$$\alpha_{E1} = \left\{\overline{D}_E\left(2 - \overline{D}_C^I\right)\right\}/\left(\overline{D}_E^I + \overline{D}_C^I - \overline{D}_E\overline{D}_C^I\right) \tag{65}$$

$$\alpha_{C1} = \left\{\overline{D}_C\left(2 - \overline{D}_E^I\right)\right\}/\left(\overline{D}_E^I + \overline{D}_C^I - \overline{D}_E\overline{D}_C^I\right) \tag{66}$$

$$\alpha_{E2} = 2 \tag{67}$$

$$\alpha_{C2} = 0\,. \tag{68}$$

For the collector side, Poisson's equation was found to be

$$(d\gamma/d\xi)^2 = \beta_{E1}\left[\exp(\gamma) - \exp(\gamma)erf\sqrt{\gamma} + 2\sqrt{\gamma/\pi} - 1\right] - \beta_{E2}\left[2\sqrt{\gamma/\pi} - \exp(\gamma)erf\sqrt{\gamma}\right]$$
$$+\varsigma/\delta\left\{\beta_{C1}\left[\exp(\gamma\delta) - \exp(\gamma\delta)erf\sqrt{\gamma\delta} + 2\sqrt{\gamma\delta/\pi - 1}\right] - \beta_{C2}\left[2\sqrt{\gamma\delta/\pi} - \exp(\gamma\delta)erf\sqrt{\gamma\delta}\right]\right\}$$

$$\text{for } \xi > 0\,. \tag{69}$$

Also, for this case, $\beta_{E1} = \alpha_{E1}$, $\beta_{E2} = 0$, $\beta_{C1} = \alpha_{C1}$, and $\beta_{C2} = \alpha_{E2}$.

5.8 Patch Effect Modelling

A thermionic diode electrode operating in the Schottky mode with currents small enough to neglect space charge will display the following output current–voltage characteristic

$$\ln J = \ln J_{SAT} + \left(e \cdot 3.79 \cdot 10^{-4}/kT\right)\sqrt{E}\,, \tag{70}$$

where E is the electric field at the emitter surface. When no space charge exists, the electric field is also the diode voltage, V, divided by the gap dimension, d

$$E = V/d\ . \tag{71}$$

Equation 70 then signifies that ln J plotted against $E^{1/2}$ results in a straight line, also known as the Schottky effect.

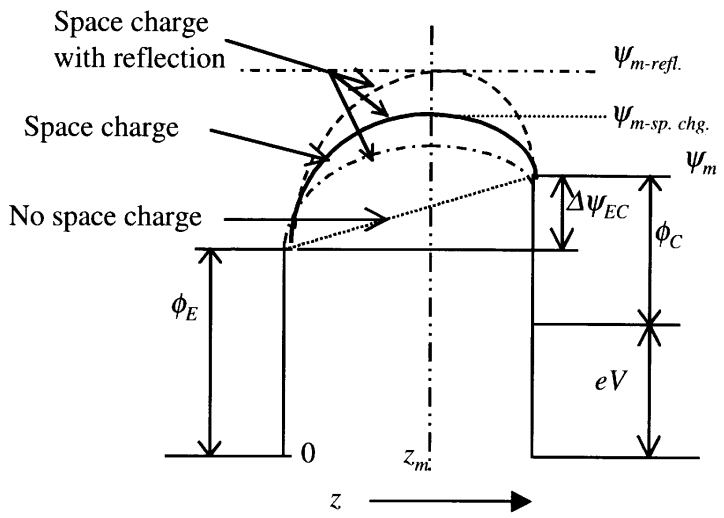

Figure 48. Interelectrode gap electron energy profile with no space charge, space charge, and space charge with reflection.

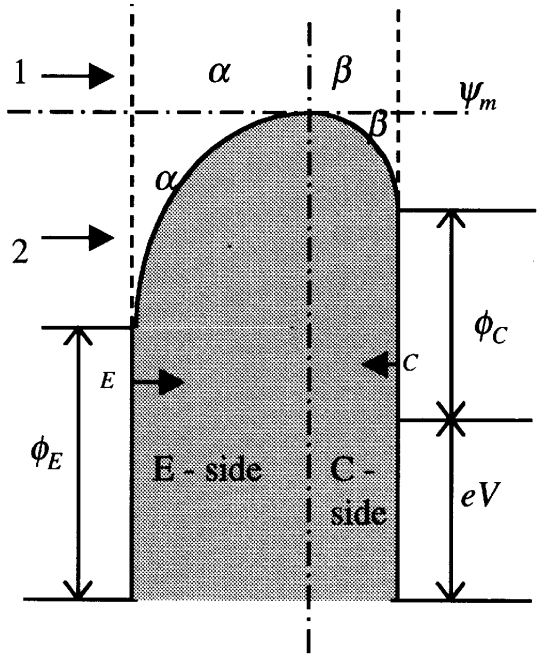

Figure 49. Pictorial of boundary conditions used to derive space charge effects with reflection.

For uniform surfaces, the Schottky effect straight line can extend to values as low as 10 V/cm (Baksht 1978). Over the years, researchers have observed an anomalous Schottky effect in which the ln J vs $E^{1/2}$ plot did not become linear until relatively high values of $E^{1/2}$. This anomalous Schottky effect was attributed to emission surfaces that were not uniform in terms of work function; this effect was also called the patch effect referring to patches of varying work function

distributed along the surface. The patch fields suppress thermionic emission from the low work function patches. When a counteracting field is applied to the patch field, normal Schottky emission is not observed until the patch field is completely suppressed. Baksht introduced the dimensionless coefficient, β, for insertion into equation 71 to approximate the anomalous Schottky effect

$$J = J_{SAT} \cdot \exp(e/kT) \cdot \exp\left(3.79 \times 10^{-4} \beta \sqrt{E}\right). \tag{72}$$

In equation 72, β is varied from 0 to 1 as the applied field increases. Figure 50 shows the patch effect (β < 1) compared to the Schottky effect (β = 1).

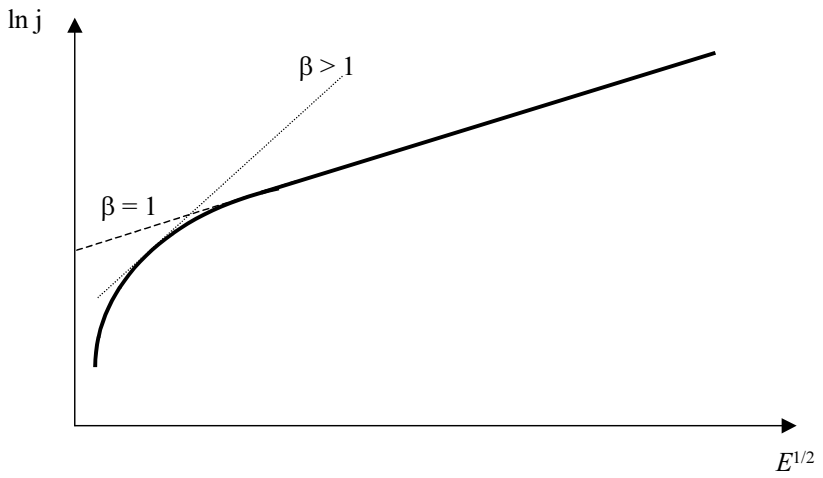

Figure 50. Schottky plot with patch effects at low-field bias.

Becker (1935) simulated patch effects by assuming a "checkerboard" distribution of equally sized low- and high-work function elements across the emitter surface. The two-dimensional variation of work functions was assumed to be sinusoidal in each direction. Nottingham (1936) assumed the emitter surface as a series of equally sized, but infinitely long, parallel low- and high-work function strips with a sinusoidal distribution from low- to high-work function. Hansen (1966) used conformal mapping techniques to improve Nottingham's configuration to parallel strips with abrupt work function changes at the strip boundaries. All of the works mentioned above reported results similar to the effect shown in Figure 50. In this work, the patch effect is modeled one-dimensionally across the electrode surface; the dimension, z, normal to the surface forms the second dimension. The one-dimensional model assumes the patches to be infinitely long in one of the dimensions.

5.8.1 THE ONE-DIMENSIONAL PATCH MODEL FOR AN EMITTING SURFACE

The vacuum thermionic converter can have patchy surfaces on both the emitter and collector. Figure 51 shows a thermionic converter with patchy electrodes that has a voltage bias placed

across the diode. By the use of superposition, the converter can be divided into three subsets. Figure 51a can be divided into: 1) a diode with a patchy emitter, smooth collector, and no bias (Figure 51b), 2) a diode with a smooth emitter, patchy collector, and no bias (Figure 51c), and 3) a diode with smooth emitter and collector with bias,V (Figure 51d). Here, a smooth electrode refers to an electrode with a homogeneous surface and no patches.

LaPlace's equation

$$d^2\psi_E/dx^2 + d^2\psi_E/dz^2 = 0 \tag{73}$$

can be used to solve each case with the boundary conditions

$$\delta\psi_E(x=0)/\delta x = 0, \tag{74}$$

$$\delta\psi_E(x=b/2)/\delta x = 0, \tag{75}$$

$$\psi_E(z=d) = 0\ , \tag{76}$$

$$\psi_E(z=0) = \phi_{1E},\ \text{for}\ 0 \le x \le a/2, \tag{77}$$

$$\psi_E(z=0) = \phi_{2E},\ \text{for}\ a/2 \le x \le b/2\ , \tag{78}$$

where a is the width of the low work function patch, b is the width of the high work function patch, ϕ_{1E} is the low-work function patch of the emitter, and ϕ_{2E} is the high-work function patch of the emitter. Figure 52 illustrates the one-dimensional model orientation.

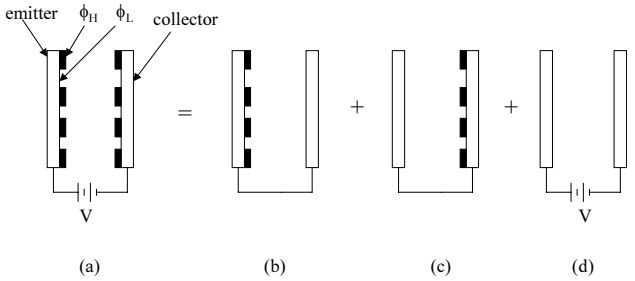

Figure 51. The patchy diode and the use of superposition to solve the patch field

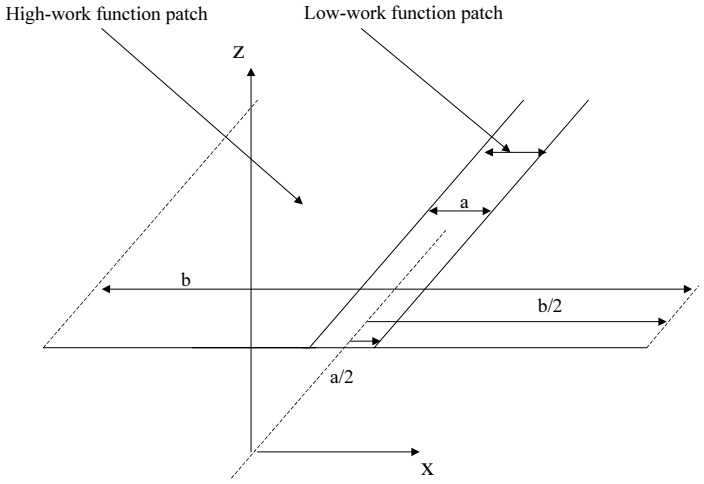

Figure 52. A proposed one-dimensional patch composed of two different work function patches

The solution of equation 73 is given by

$$\psi(x,z) = \phi_{2E} - (a/b)(\phi_{1E} - \phi_{2E})$$
$$+ 2/\pi \cdot (\phi_{1E} - \phi_{2E}) \cdot \sum_{n=1}^{\infty} (1/n) \cdot \sin(n\pi\, a/b) \cdot \cos(\lambda_x x) \cdot \sinh[\lambda_n (d - z)] / \sinh(\lambda_n d). \quad (79)$$

Equation 79 represents the electron potential energy above the patchy emitter and along its surface.

For the patchy collector with normal coordinate, $\tilde{z}$, the electron potential energy, ψ_C, is derived as above and can be written as

$$\psi_C(x,\tilde{z}) = \phi_{2C} - (a/b)(\phi_{1C} - \phi_{2C})$$
$$+ (2/\pi) \cdot (\phi_{1C} - \phi_{2C}) \cdot \sum_{n=1}^{\infty} (1/n) \cdot \sin(n\pi\, a/b) \cdot \cos(\lambda_x x) \cdot \sinh[\lambda_n (d - \tilde{z})] / \sinh(\lambda_n d) \quad (80)$$

The gap distance, d, is related to z and $\tilde{z}$ by

$$d = z + \tilde{z}, \quad (81)$$

and can be substituted into equation 80 to yield

$$\psi_C(x,z) = \phi_{2C} - (a/b)(\phi_{1C} - \phi_{2C})$$
$$+ (2/\pi) \cdot (\phi_{1C} - \phi_{2C}) \cdot \sum_{n=1}^{\infty} (1/n) \cdot \sin(n\pi\, a/b) \cdot \cos(\lambda_x x) \cdot \sinh[\lambda_n z] / \sinh(\lambda_n d). \quad (82)$$

Equation 82 represents the electron potential energy above the patchy collector measured from the emitter surface and along the collector surface. Parts 1 and 2 out of 3 parts of equations 80 and 82 represents the area weighted average of the work functions of the two patches. The potential energy distribution for the third part of the superposition shown in Figure 18d is given by

$$\psi(x,z) = (eV/d)z \ , \quad (83)$$

where V is the voltage applied across the thermionic converter.

5.8.2 The One-Dimensional Patch Model Applied to Opposing Surfaces in a Converter

The fields due to emitter patches, collector patches, and voltage bias sum to form the total field, E_t, in the gap and is given by

$$E_t = \delta\psi_E/\delta z + \delta\psi_C/\delta z + eV/d \ , \quad (84)$$

The total potential energy distribution in the gap, ψ_t, can then be calculated by integrating equation 84 to yield

$$\psi_t(x,z) = \psi_0 + (2/\pi)\cdot(\phi_{1E} - \phi_{2E})\cdot\sum_{n=1}^{\infty}(1/n)\cdot\sin(n\pi\, a/b)\cdot\cos(\lambda_x x)\cdot\sinh[\lambda_n(d-z)]/\sinh(\lambda_n d)$$

$$+ (2/\pi)\cdot(\phi_{1C} - \phi_{2C})\cdot\sum_{n=1}^{\infty}(1/n)\cdot\sin(n\pi\, a/b)\cdot\cos(\lambda_x x)\cdot\sinh[\lambda_n z]/\sinh(\lambda_n d) + (eV/d)z \ , \qquad (85)$$

where ψ_0 is an integration constant that is equal to the area weighted average of the patches at the emitter surface.

Figure 53 shows the electron potential energy in the gap as calculated by equation 85 for a diode voltage bias of zero (V = 0). The patch work function with a high value for both emitter and collector is 1.8 eV, and the patch work function with a low value for both emitter and collector is 1.1 eV. The relative patch size is assigned as b = 2a. Figure 53b shows a cross-cut of the electron potential energy along the z-axis as a function of distance along the gap at the center of the low work function patch (x = 0) and the center of the high work function patch (x = b/2). Again, for both the emitter and collector, the patch field forms an effective barrier of 1.45 eV in front of the low-work function patches. The high-work function patch is not influenced by the patch field.

Figure 57 illustrates the gap electron potential energy distribution with respect to x and z when the emitter has an accelerating field bias of 500 V/cm at its surface. Conversely, the collector has a decelerating field bias of 500 V/cm at its surface. Figure 57b shows that the electron potential energy at the center of the emitter low work function patch (x = 0) now has a maximum, $\psi_{max\ lp}$, of approximately 1.31 eV. This maximum has decreased by 0.14 eV compared to the case in Figure 53b because of the accelerating field at the emitter surface. The maximum electron potential energy at the emitter high patch surface remains relatively unchanged, dropping only by several hundredths of an eV. Increasing the accelerating field will eventually lower $\psi_{max\ lp}$ to its true value of 1.1 eV. The collector surface patch effect does not matter because of the decelerating field at its surface; the maximum energy barrier observed by the electrons leaving the collector is $\psi_{max\ lp}$ and $\psi_{max\ hp}$ near the emitter surface.

The maximum potential energy in front of the low work function patch caused by the patch field is not constant across the patch surface; this variation in $\psi_{max\ lp}$ is shown in Figure 57. The value of $\psi_{max\ lp}$ increases and moves toward the emitter surface as the x -position across the low work function patch moves from its center to the boundary with the high-work function patch. Figure 56 illustrates the maximum electron potential energy, ψ_{max}, as a function of position, x, across the patch and the distance, z, into the gap at which the maximum occurs; the large transition in electron potential energy occurs at the patch boundary. Nottingham (1936) refers to this maximum electron potential energy profile as the "skyline." The effect of increasing accelerating field (from 500 V/cm to 4500 V/cm) on the maximum electron potential energy is demonstrated in Figure 57. The maximum over the low work function patch decreases and extends toward the patch boundary as the field is increased. The maximum electron potential energy in front of the high work function patch decreases slightly. As the low work function patch size decreases, the patch field causes the surface effective work function and maximum

electron potential energy to increase, as shown in Figure 58. Therefore, higher fields will be required to reduce the maximum potential as shown in Figure 57.

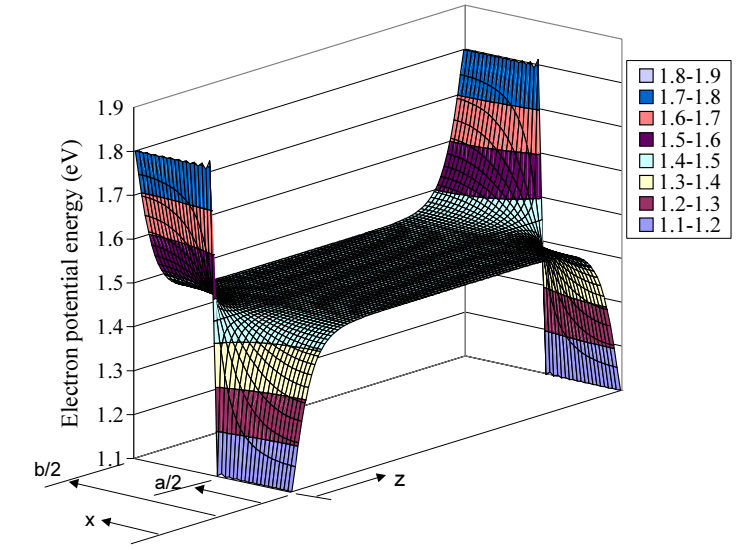

(a)

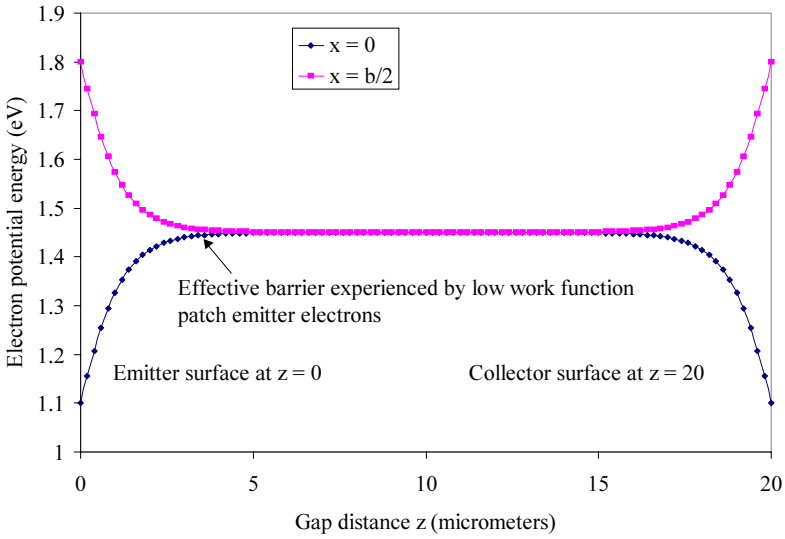

(b)

Figure 53. (a) The electron potential energy in the interelectrode gap due to the emitter and collector patch field with no external field bias. (b) The electron potential energy in the interelectrode gap at two x-positions.

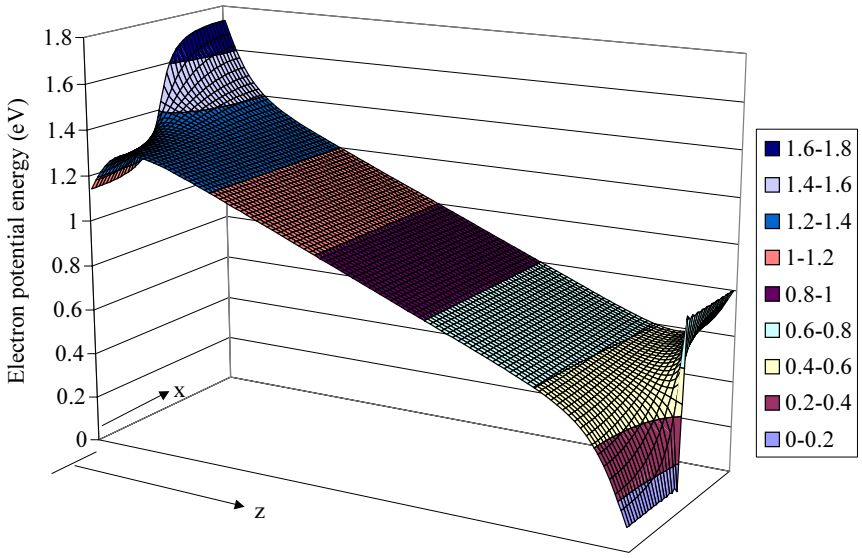

(a)

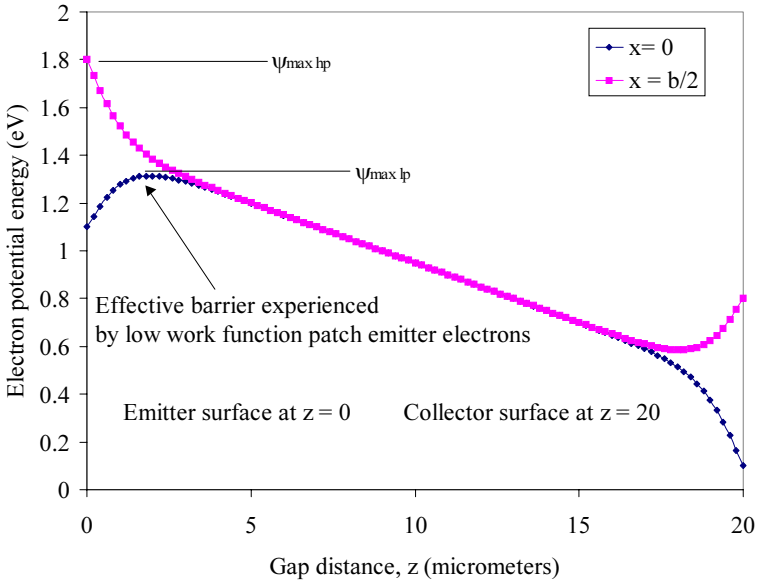

(b)

Figure 54. (a) The electron potential energy in the interelectrode gap due to the emitter and collector patch field with an accelerating external field bias. (b) The electron potential energy in the interelectrode gap at two x-positions.

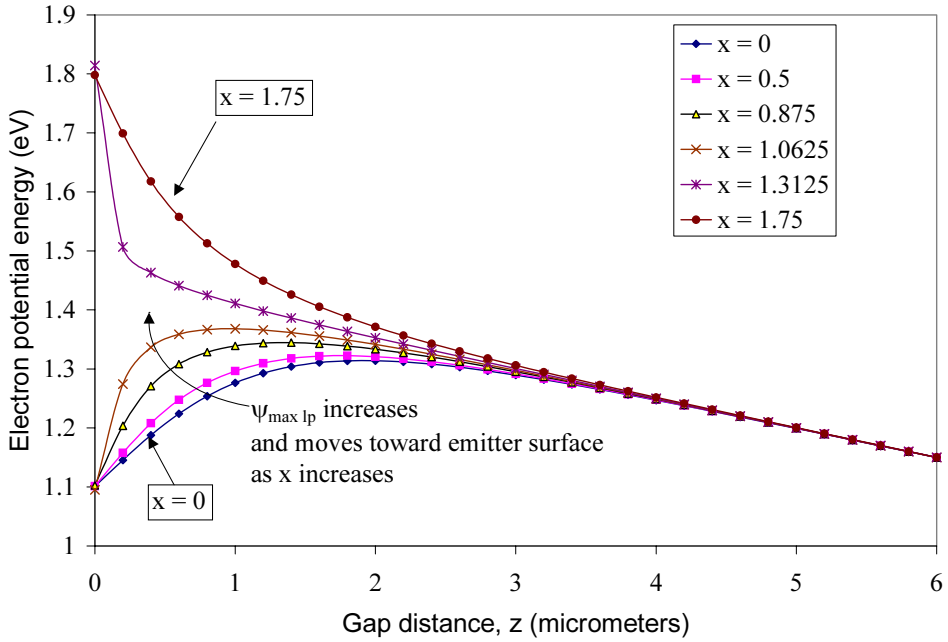

Figure 55. Electron potential energy profiles above the emitter as a function of position along the patchy surface and position above the patchy surface.

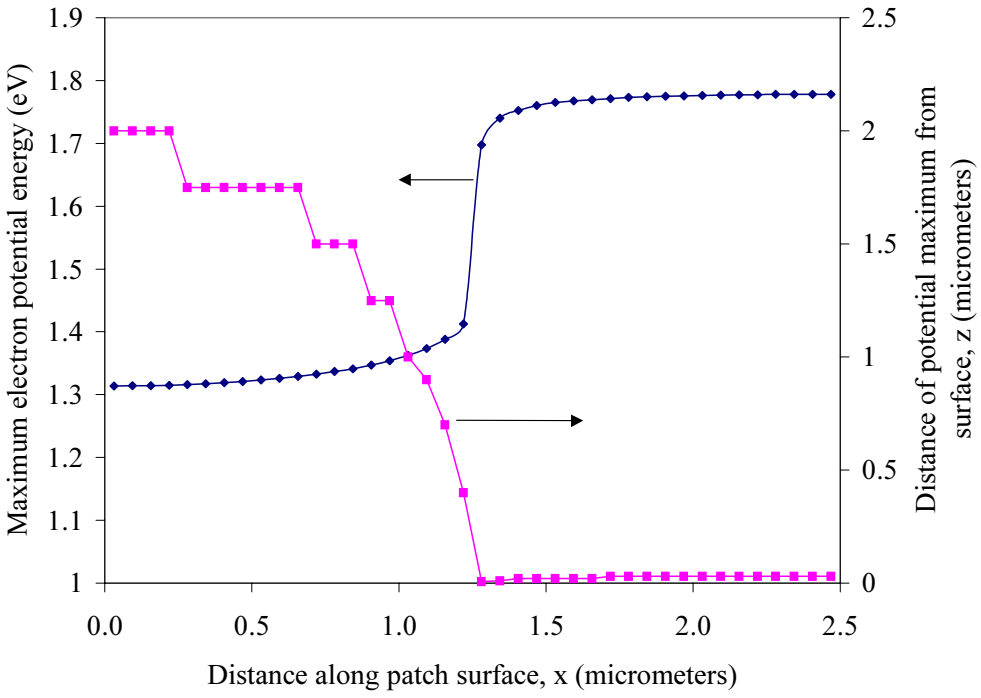

Figure 56. The maximum electron potential energy and the location of the maximum above a patchy surface as a function of position along the patch surface.

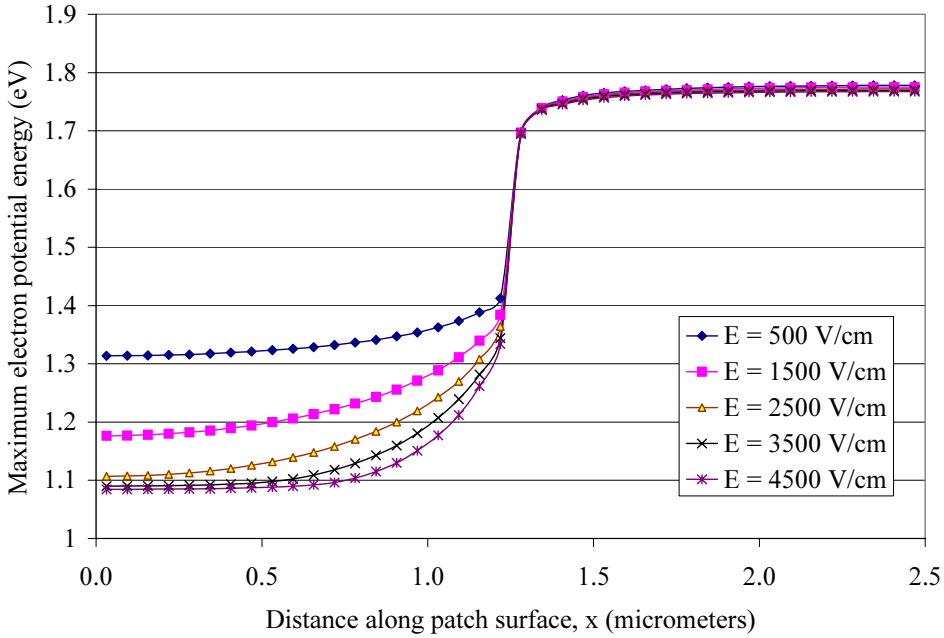

Figure 57. The maximum electron potential energy across a patchy surface as a function of an accelerating bias field applied to the surface.

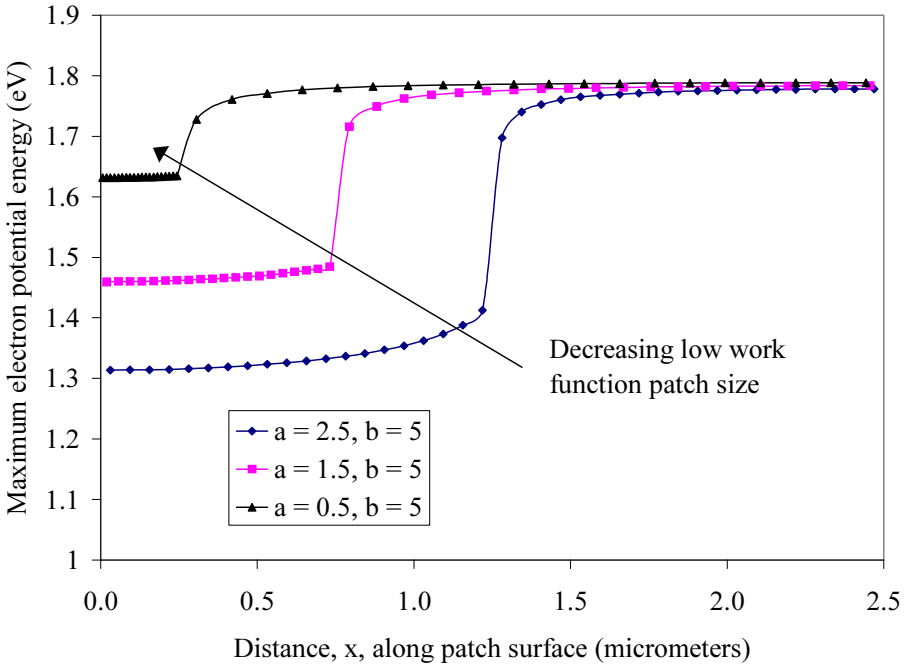

Figure 58. The effect of patch size on the maximum electron potential energy as a function of position across the patchy surface.

5.9 The Effect of Patchy Surfaces on Transmission Coefficients

Two patch types are defined: a low-ϕ patch of width a and a high-ϕ patch of width b. As illustrated in Figure 59, the patches are assumed to be alternating one–dimensional strips. The work function in the high-ϕ patch is allowed to gradually transition to the low-ϕ patch. The maximum in the motive barrier (skyline) is illustrated as a function of x-position across the patches. Discrete x-positions are numbered from i = 1 through N for the low-ϕ patch, and from i = 1+N through M for the high-ϕ patch.

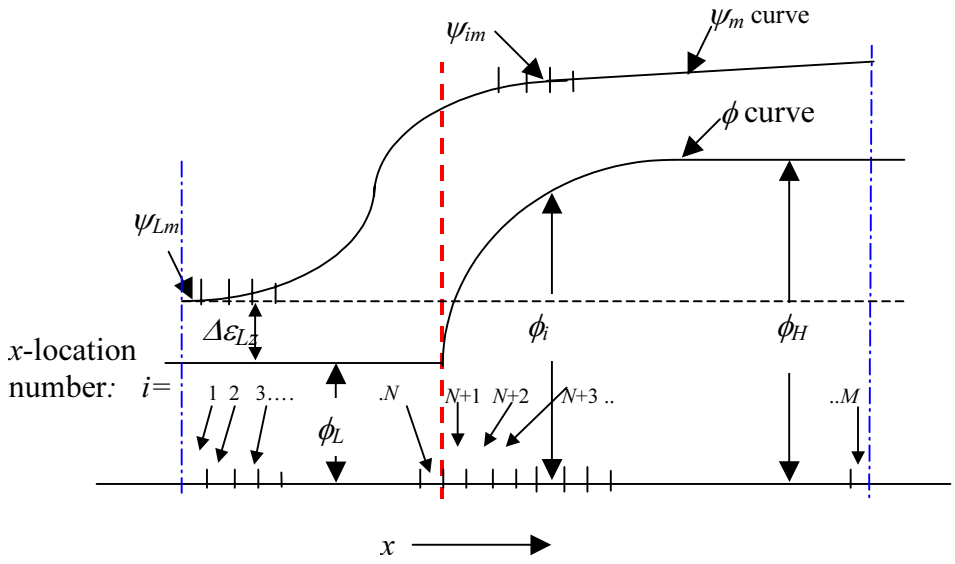

Figure 59. Patch work function distribution.

Transmission coefficients are assigned to each mesh interval i by taking the mesh interval having the lowest value for its maximum motive ψ_{Lm}, as the maximum motive for the entire surface. Consequently, electron energy is referenced to $\varepsilon_z = 0$ at ψ_{Lm}. Furthermore, all electrons in interval i with energy ε_z (referenced to $\varepsilon_z = 0$ at ψ_{Lm}) less than ψ_{im} will be 100% reflected, and the transmission coefficient equals zero. For the low work function patches, we assume a dipole due to absorbed species on the surface resulting in a reflection coefficient similar to the one observed for Ir-Cs-O, shown in Figure 60. Electrons with energy greater than ψ_{im} will have sufficient energy to escape, but a fraction will be reflected depending on the value of the transmission coefficient at the energy under consideration. For the high work function patches, the transmission coefficient associated with an inverted gaussian potential can be assumed (Marshall 1999).

Note that the zero of energy for the reflection coefficients is referenced to ϕ_i at each mesh interval; thus at each mesh interval i the energy point to ε_z corresponds to $\varepsilon_{zd} = \Delta\varepsilon_{zL} + \varepsilon_z - \Delta\phi_i$ in Figure 59. Here, $\Delta\varepsilon_{zL} = \psi_{Lm} - \phi_L$ and $\Delta\phi_i = \phi_i - \phi_L$. These assumptions are illustrated in Figure 61 for the interval with the lowest maximum motive. An electron with the same energy striking a region with a higher maximum motive is illustrated in Figure 62. For this case, the electron has insufficient energy to escape, and the transmission coefficient is zero. For an electron of higher energy (labeled 2), the electron has sufficient energy to pass over the motive barrier for interval i.

Note the change in position of the zero of energy relative to the reflection coefficient. The rules for assigning energy dependent transmission coefficients are:

Low-ϕ patch For $\varepsilon_z > \psi_{im}$, use $D_L(\varepsilon_{zd})$ from Ir-Cs-O data in Fig. 60 (ε_z corresponds to $\varepsilon_{zd} = \Delta\varepsilon_L + \varepsilon_z - \Delta\phi_i$.).

For $\varepsilon_z < \psi_{im}$, $D(\varepsilon_z) = 0$.

High-ϕ patch For $\varepsilon_z > \psi_{im}$, Transmission coefficient = $D_H(\varepsilon_{zd})$, from inverted gaussian dipole quantum calculation. (Use the same approach for referencing the zero of energy as above.)

For $\varepsilon_z < \psi_{im}$, $D(\varepsilon) = 0$.

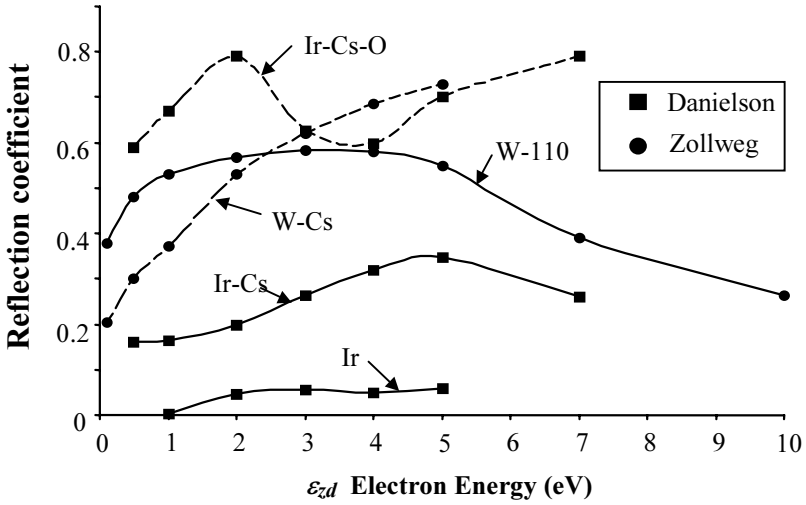

Figure 60. Reflection coefficient vs. electron energy for various electrodes.

Using the previously defined transmission coefficients and approach, we can compute the energy-dependent associated transmission coefficient using

$$D_{aE}(\varepsilon_z) = \sum_{i=1}^{N} aD_{Li}(\varepsilon_z)/N + \sum_{i=N+1}^{M} bD_{Hi}(\varepsilon_z)/(M-N) \Big/ (a+b). \tag{86}$$

Note that the same approach is used for the obstructed mode. Also recall that

$$D_i(\varepsilon_z) = D_i(\varepsilon_{zd} = \Delta\varepsilon_{zL} + \varepsilon_z - \Delta\phi_i), \quad \Delta\varepsilon_{zL} = \psi_{Lm} - \phi_L, \text{ and } \quad \Delta\phi_i = \phi_i - \phi_L. \tag{87}$$

Integrating the internal energy/angle spectrum equation over all angles, we obtain the ideal (no reflection) energy spectrum for emission (Marshall 1998):

$$F_E(\varepsilon_z) = \frac{1}{kT_E} \exp\left(\frac{-\varepsilon_z}{kT_E}\right). \tag{88}$$

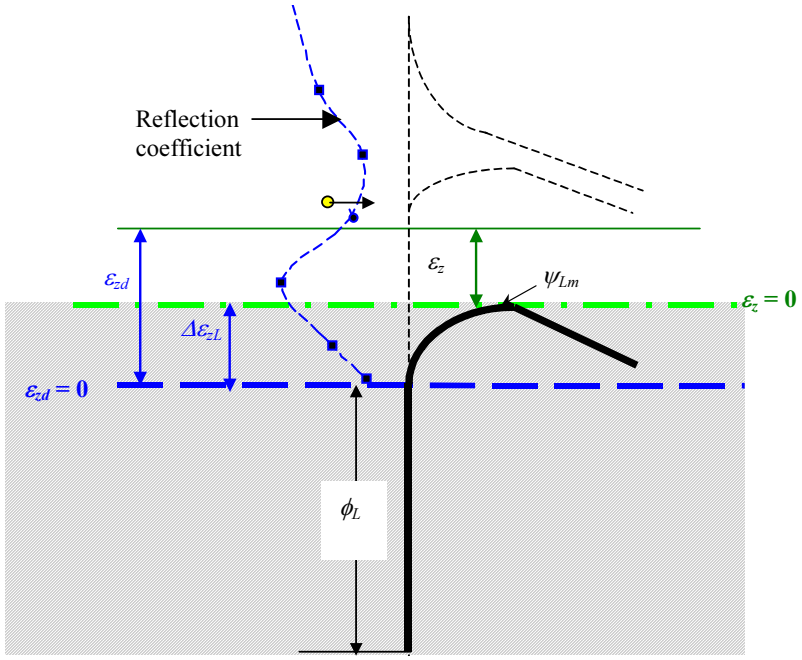

Figure 61. Energy reference points for interval with lowest ψ_{im} (i.e., ψ_{Lm}).

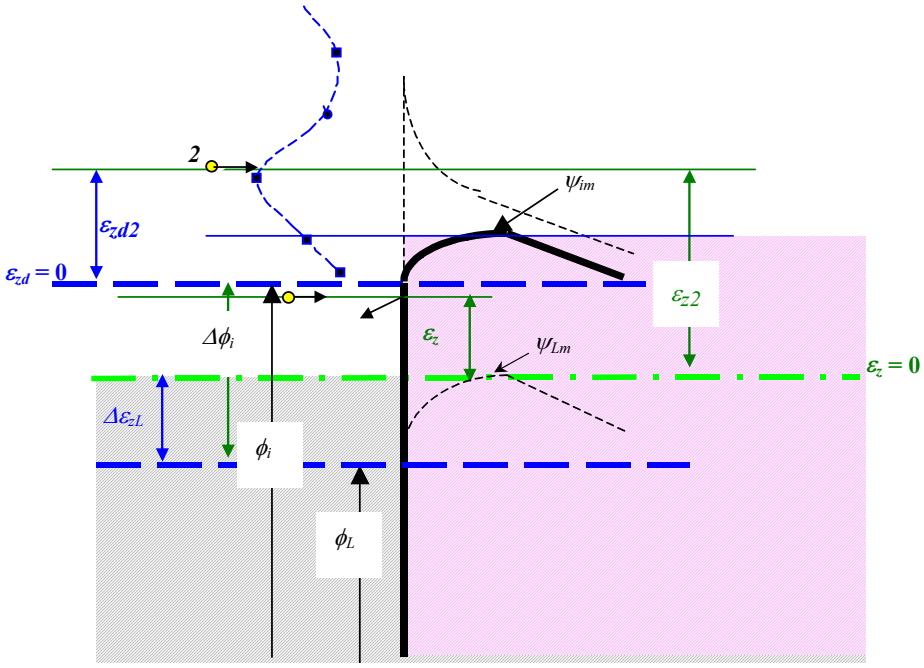

Figure 62. Energy reference points for interval with > ψ_{Lm}.

The average associated transmission coefficients for the emitter is

$$\overline{D}_{aE} = \int_0^\infty D_{aE}(\varepsilon_z) F_E(\varepsilon_z) d\varepsilon_z . \tag{89}$$

The same process is used to compute $\overline{D}_{aC}$.

The incident spectrum includes electrons emitted from and reflected from both electrodes, including multiple reflections. We begin with the fractional spectrum for electrons emitted from the emitter, incident upon the collector

$$f_{C1}^{E}(\varepsilon_z) = D_{aE}(\varepsilon_z) F_E(\varepsilon_z). \tag{90}$$

The superscript for external electron fractional spectra identifies the source of the electrons, and the subscript identifies the surface struck and the number of times these electrons have struck the surface.

The spectrum of these electrons after reflecting from the collector and striking the emitter for the first time is,

$$f_{E1}^{E}(\varepsilon_z) = f_{C1}^{E}(\varepsilon_z) R_C(\varepsilon_z) = D_{aE}(\varepsilon_z) F_E(\varepsilon_z) R_C(\varepsilon_z), \tag{91}$$

where $R_C(\varepsilon_z)$ is the energy-dependent reflection coefficient for the collector. Following this process we obtain

$$f_{C2}^{E}(\varepsilon_z) = f_{E1}^{E}(\varepsilon_z) R_E(\varepsilon_z) = D_{aE}(\varepsilon_z) F_E(\varepsilon_z) R_C(\varepsilon_z) R_E(\varepsilon_z),$$

$$f_{E2}^{E}(\varepsilon_z) = D_{aE}(\varepsilon_z) F_E(\varepsilon_z) R_C^2(\varepsilon_z) R_E(\varepsilon_z)$$

$$f_{C3}^{E}(\varepsilon_z) = D_{aE}(\varepsilon_z) F_E(\varepsilon_z) R_C^2(\varepsilon_z) R_E^2(\varepsilon_z)$$

$$\ldots. \tag{92}$$

The total spectra of electrons emitted by the emitter incident externally on the emitter is

$$f_E^{E}(\varepsilon_z) = D_{aE}(\varepsilon_z) F_E(\varepsilon_z) R_C(\varepsilon_z) \sum_{n=1}^{\infty} \left[R_E(\varepsilon_z) R_C(\varepsilon_z) \right]^{n-1}, \tag{93}$$

or

$$f_E^{E}(\varepsilon_z) = \frac{D_{aE}(\varepsilon_z) F_E(\varepsilon_z) R_C(\varepsilon_z)}{1 - R_E(\varepsilon_z) R_C(\varepsilon_z)}. \tag{94}$$

If we assume no energy or angle change during reflection, the collector reflection coefficient is

$$R_C(\varepsilon_z) = 1 - D_{aC}(\varepsilon_z), \tag{95}$$

and

$$R_E(\varepsilon_z) = 1 - D_{aE}(\varepsilon_z), \tag{96}$$

then Eq. (94) becomes

$$f_E^{E}(\varepsilon_z) = \frac{D_{aE}(\varepsilon_z) F_E(\varepsilon_z) \left[1 - D_{aC}(\varepsilon_z) \right]}{D_{aE}(\varepsilon_z) + D_{aC}(\varepsilon_z) - D_{aE}(\varepsilon_z) D_{aC}(\varepsilon_z)}. \tag{97}$$

From above, we also find that the total spectra of electrons emitted by the emitter incident externally on the collector is

$$f_C^E(\varepsilon_z) = \frac{D_{aE}(\varepsilon_z) F_E(\varepsilon_z)}{D_{aE}(\varepsilon_z) + D_{aC}(\varepsilon_z) - D_{aE}(\varepsilon_z) D_{aC}(\varepsilon_z)}. \tag{98}$$

Following the same procedure for electrons emitted from the collector we obtain:

$$f_C^C(\varepsilon_z) = \frac{D_{aC}(\varepsilon_z) F_C(\varepsilon_z)[1 - D_{aE}(\varepsilon_z)]}{D_{aE}(\varepsilon_z) + D_{aC}(\varepsilon_z) - D_{aE}(\varepsilon_z) D_{aC}(\varepsilon_z)}, \tag{99}$$

and

$$f_E^C(\varepsilon_z) = \frac{D_{aC}(\varepsilon_z) F_C(\varepsilon_z)}{D_{aE}(\varepsilon_z) + D_{aC}(\varepsilon_z) - D_{aE}(\varepsilon_z) D_{aC}(\varepsilon_z)}. \tag{100}$$

The externally incident current density of all external electrons incident on the emitter is

$$J_E^I(\varepsilon_z) = f_E^E(\varepsilon_z) J_E + f_E^C(\varepsilon_z) J_C. \tag{101}$$

Thus, the fractional incident spectrum for the emitter is

$$f_E^I(\varepsilon_z) = \frac{J_E^I(\varepsilon_z)}{\int_0^\infty J_E^I(\varepsilon_z) d\varepsilon_z}, \tag{102}$$

and the associated transmission coefficients for external electrons incident on the emitter is

$$\overline{D}_{aE}^I = \int_0^\infty D_{aE}(\varepsilon_z) f_E^I(\varepsilon_z) d\varepsilon_z. \tag{103}$$

The collector coefficients are obtained in the same manner. Only Eqs. (97-103) are needed to compute $\overline{D}_{aE}^I$. A similar procedure is used to compute $\overline{D}_{aC}^I$.

5.10 Overview of current-voltage calculational code

The outer shell of the code reads the input data and calls several subroutines. Two of the subroutines model the patchy surface of the emitter and collector. The remaining five subroutines calculate the diode characteristics of the five operating modes. The two patch subroutines compute the electron potential energy above the patchy surfaces for a zero field condition at the electrode surface. The saturation mode of operation subroutine, jsfind, is called first. Jsfind calculates the saturation mode voltage and current density. Then, the critical point mode of operation subroutine, jrfind, is called; this subroutine calculates the critical point voltage and current density. The third call is to the Schottky mode subroutine, jschtfind. This subroutine calculates a set of output voltages and current densities, starting from the saturation voltage to a user specified maximum voltage, v_sch_max. Next, the space charge mode subroutine, jspchfind, is called and calculates a user specified number of voltage-current density sets

between the saturation and critical points. Finally, the retarded mode operation subroutine, jretregfind, is called. This subroutine calculates a set of output voltages and current densities, starting from the critical point voltage to a user specified maximum voltage, v_retd_max.

5.10.1 Saturation Point Subroutine, JSAT

At the saturation point, the bias field on the emitter is defined to be zero, and the bias field on the collector is decelerating in nature. Figure 63 illustrates the electron energy potential for the saturation condition.

First, a saturation voltage value is guessed. If patch conditions exist on the emitter and collector surface, the first calculation performed is to calculate the average emitter and collector work functions as well as the "skyline" barrier (as described in section 5.8.2). Then, the transmission coefficients described in Section 5.9 are calculated. Finally, the effective diode transmission coefficient, τ , and the symmetry index, Γ, are calculated. The calculational steps of equations 104 through 106 (shown below) are performed to calculate a new saturation point diode voltage, v_sat.

The emitter saturation current density,

$$xj\_es = \tau_{sat} \cdot A \cdot T_E^2 \cdot \exp\left(-\phi_E / kT_E\right), \tag{104}$$

is calculated. The dimensionless or normalized gap distance, ξ_C or d/x_0, as shown in Figure 31 is then calculated by (recall that $\xi_E = 0$)

$$\xi_C = d/x_0 = d/\left(1.09x10^{-6} \cdot \left(T_E^{3/4} / \sqrt{xj\_es}\right)\right), \tag{105}$$

where d is the gap size of the converter. Given ξ_C, the Poisson's equation for the collector side is then integrated to solve for the dimensionless voltage, γ_C (see Sections 5.4, 5.5, or 5.7). The Poisson's equation is integrated using Simpson's rule with an Aitken extrapolation.

The saturation voltage, v_sat, can then be calculated with the relationship shown in Figure 63,

$$v\_sat = \phi_E - \phi_C - \left(kT_E\right)\gamma_C \ . \tag{106}$$

The effective energy potentials above the patchy surface and transmission coefficients can then be recalculated. v_sat is calculated again using the procedure described above. This procedure is repeated until the value of v_sat converges.

The back emission current density from the collector, xj_c_at_sat, is given by the Richardson-Dushman equation

$$xj\_c\_at\_sat = A \cdot T_C^2 \cdot \exp\left(-\left(\phi_C + kT_E\gamma_C\right)/kT_E\right), \tag{107}$$

where the term in the numerator of the exponential represents the potential energy barrier experienced by electrons emitted from the collector.

Finally, the net current density at the saturation point, xj_sat_net, is given by

$$xj\_sat\_net = \tau_{sat}\left(xj\_es - \Gamma_{sat} \cdot xj\_c\_at\_sat\right). \tag{108}$$

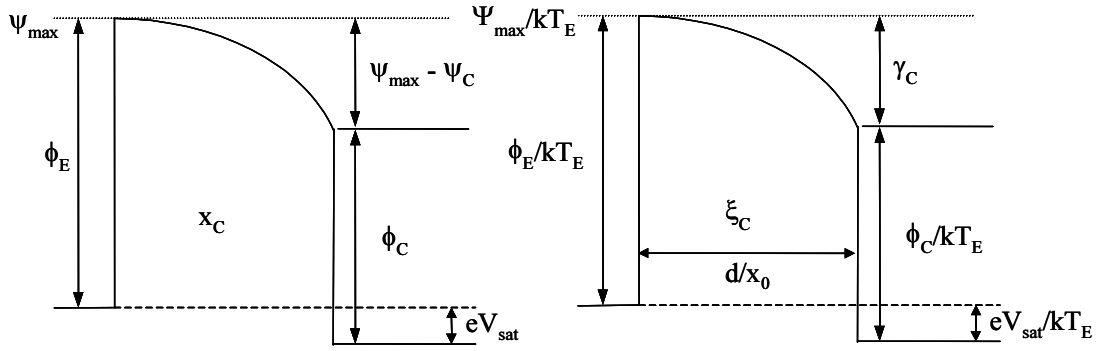

Figure 63. The electron potential energy and dimensionless potential energy for the saturation mode.

5.10.2 Critical Point Subroutine, JRFIND

At the critical point, the bias field on the collector is defined to be zero, and the bias field on the emitter is decelerating in nature. Figure 64 illustrates the interelectrode electron energy potential distribution for the critical condition.

First, a critical point voltage value is assumed. If patch conditions exist on the emitter and collector surface, the first calculation performed is to calculate the average emitter and collector work functions as well as the "skyline" barrier (as described in section 5.8.1). Then, the transmission coefficients described in Section 5.9 are calculated. Finally, the effective diode transmission coefficient, τ , and the symmetry index, Γ, are calculated. The calculational steps of equations 109 through 112 (shown below) are performed to calculate a new critical point diode voltage, v_crit.

The saturation current from the emitter , xj_es, is first calculated by

$$xj\_es = \tau_{crit} \cdot A \cdot T_E^2 \cdot \exp\left(-\phi_E / kT_E\right). \tag{109}$$

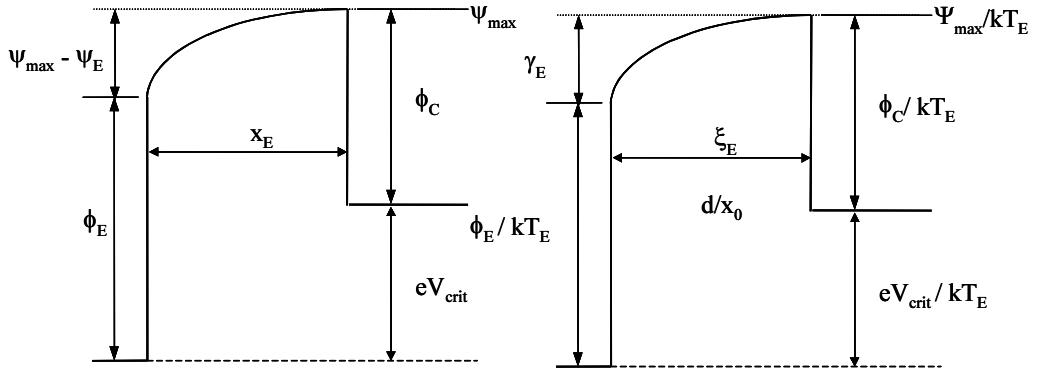

Figure 64. The electron potential energy and dimensionless potential energy for the critical point mode

Next, the emitter current at the critical point must be estimated; the saturation current serves as an upper limit on the first estimation of the critical point current. The upper and lower limits of the estimated critical point current are then arbitrarily chosen as $0.9999 \cdot \mathrm{xj\_es}$ and $0.00001 \cdot \mathrm{xj\_es}$, respectively. With the first estimate of the critical point emitter current density, xj_t, the dimensionless emitter electron potential energy, γ_E, is given by

$$\gamma_E = \ln(xj\_es / xj\_t) \; . \tag{110}$$

Given γ_E, Poisson's equation for the emitter side is then integrated to solve for the dimensionless gap dimension, ξ_E (see Sections 5.4, 5.5, or 5.7).

Equation 111 can now be used to calculate an updated critical point emitter current density, xj_t_new,

$$xj\_t\_new = 1.188x10^{-12} \cdot \xi_E^2 \cdot T_E^{1.5} / dgap^2 \; . \tag{111}$$

If the difference between xj_t_new and xj_t exceeds a user defined tolerance limit, xj_t_new is substituted for xj_t in equation 110. This process is continued until the difference becomes less than a user-defined tolerance; the critical point current is then assigned the variable name, xj_e_cr.

Once the critical point current density has been calculated, γ_E and ξ_E, are known, and Figure 64 illustrates the relation between the critical point output voltage and γ_E. The critical point output voltage, v_cr, is

$$\mathrm{v\_cr} = \mathrm{kT_E}\gamma_E + \phi_E - \phi_C \; . \tag{112}$$

The effective patch energy potentials and transmission coefficients can then be recalculated. v_cr is calculated again using the procedure described above. This procedure is repeated until the value of v_cr converges.

The emission from the collector surface, xj_c_cr, is then

$$xj\_c\_cr = A \cdot T_C^2 \cdot \exp\left(-\phi_C / kT_C\right) . \tag{113}$$

Finally, the net current density at the critical point, xj_cr, is given by

$$\mathrm{xj\_cr} = \tau_{\mathrm{crit}}\left(\mathrm{xj\_e\_cr} - \Gamma_{\mathrm{crit}} \cdot \mathrm{xj\_c\_cr}\right). \tag{114}$$

5.10.3 Schottky Point Subroutine, JSCHTFIND

In the schottky mode, the bias field on the emitter is accelerating in nature, and the bias field on the collector is decelerating. Figure 65 illustrates the interelectrode electron energy potential distribution for the schottky mode of operation.

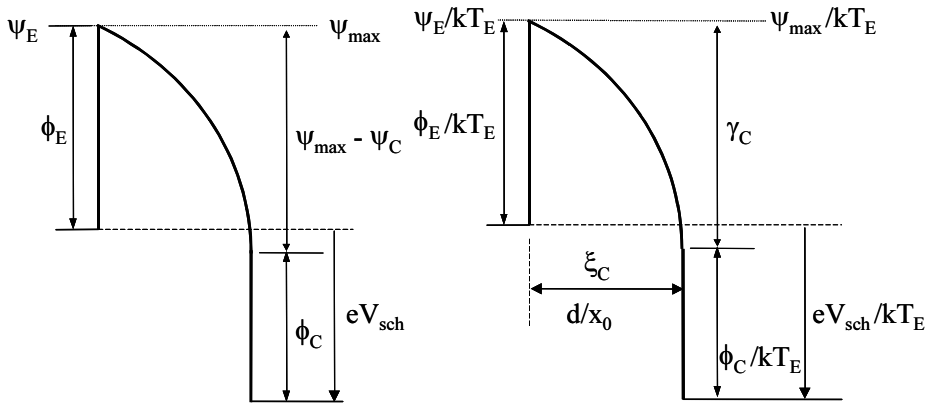

Figure 65. The electron potential energy and dimensionless potential energy for the Schottky mode

In the main section of the code, the maximum Schottky voltage, v_sch_max, and the number of Schottky mode points, num_sch , to be calculated are input parameters. The maximum field, e_max, that the emitter will experience during the Schottky mode is then

$$e\_\max = (v\_sch\_\max - v\_sat)/dgap \ . \tag{115}$$

The incremental electric field, del_e, on the emitter surface is then the maximum electric field divided by the number of output voltage-current pairs, num_sch, to be calculated in the Schottky mode. The electric field, efield, at each Schottky mode calculation is then

$$\mathrm{efield} = \mathrm{e\_max} - \left(\mathrm{num\_sch} - \mathrm{istep}\right) \cdot \mathrm{del\_e}, \tag{116}$$

where istep is the loop parameter that varies from 1 to num_sch.

If patch conditions exist on the emitter and collector surface, the first calculation performed is to calculate the average emitter and collector work functions as well as the "skyline" barrier (as described in section 5.8.1). Then, the transmission coefficients described in Section 5.9 are calculated. Finally, the effective diode transmission coefficient, τ , and the symmetry index, Γ, are calculated. The calculational steps of equations 117 through 119 (shown below) are performed to calculate a new critical point diode voltage, v_crit. The iterational procedure described above in section 5.10.1 to calculate v_sat is also used to calculate the Schottky voltage, v_sch.

The emitter saturation current, xj_es, is first calculated. The Schottky current, xj_sch, can then be calculated with equation 117 and is

$$xj\_sch = \tau_{sch} \cdot xj\_es \cdot \exp\left(3.79x10^{-4}\sqrt{\alpha_S \cdot efield}\,/kT_E\right). \tag{117}$$

The dimensionless gap distance, ξ_C, is related to the schottky current by

$$\xi_C = 9.186x10^5 \cdot T_E^{-3/4} \cdot \sqrt{xj\_sch} \cdot dgap\ , \tag{118}$$

from equation 105. Given ξ_C, Poisson's equation is then integrated to solve for the dimensionless voltage, γ_C. The schottky voltage, v_sch, can then be calculated with the relationship shown in Figure 65,

$$v\_sch = \phi_E - \phi_C - (kT_E)\gamma_C\ . \tag{119}$$

The effective potential barriers and transmission coefficients can then be recalculated. v_sch is calculated again using the procedure described above. This procedure is repeated until the value of v_sch converges.

The back emission from the collector, xj_c_schp, is given by the Richardson-Dushman equation

$$xj\_c\_schp = A \cdot T_C^2 \cdot \exp\left(-\left(\phi_C + kT_E \cdot \gamma_C\right)/kT_C\right), \tag{120}$$

where the term in the numerator of the exponential represents the potential energy barrier experienced by electrons emitted from the collector.

Finally, the net current density in the schottky mode, xj_net_schp, is given by

$$xj\_net\_schp = \tau_{sch}\left(xj\_sch - \Gamma_{sch} \cdot xj\_c\_schp\right). \tag{121}$$

5.10.4 Space Charge Subroutine, JSPCHFIND

For the space charge mode of operation, the electron potential energy maximum exists in the gap. The bias field on the emitter and collector is decelerating in nature. Figure 66 illustrates the interelectrode electron energy potential distribution for the space charge mode of operation.

If patch conditions exist on the emitter and collector surface, the first calculation performed is to calculate the average emitter and collector work functions as well as the "skyline" barrier (as described in section 5.8). Then, the transmission coefficients described in Section 5.9 are calculated. Finally, the effective diode transmission coefficient, τ , and the symmetry index, Γ, are calculated. The same iterational procedure described above in section 5.10.1 to calculate v_sat is also used to calculate the maximum electron potential energy, ψ_{max}.

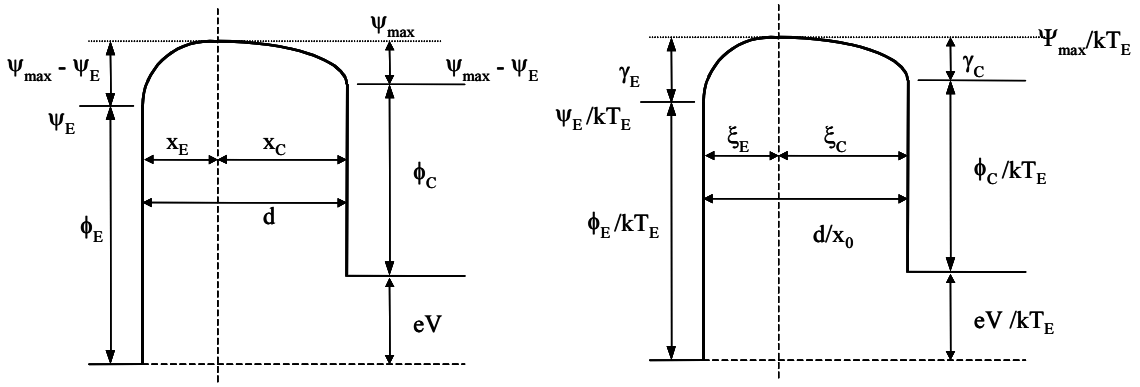

Figure 66. The electron potential energy and dimensionless potential energy for the space charge mode.

The voltage range of operation in the space charge mode, delv, is set by the saturation subroutine and the critical point subroutine and is given by

$$delv = v\_sat - v\_cr \tag{122}$$

The program user inputs the number of voltage-current pairs, num_sp_ch, to be calculated in the space charge mode. Therefore, the voltage, v, to be calculated is

$$v = v\_cr - iv \cdot delv / num\_sp\_ch \ , \tag{123}$$

where iv is an integer counter ranging from 1 to num_sp_ch.

After an operational voltage, v, is selected in the space charge mode, the dimensionless collector electron potential, γ_C, must be guessed. Based on this estimate, $\gamma_{C\ est}$, the maximum electron potential energy shown in Figure 66 is calculated by

$$\psi_{max} = \gamma_{Cest} \cdot (kT_E) + \phi_C + eV \ . \tag{124}$$

The emitter current density, J_E, can then be calculated given ψ_{max} and is

$$J\_E = A \cdot T_E^2 \cdot \exp\left(-\psi_{\max} / kT_E\right) . \tag{125}$$

The collector current density, J_C, is given by

$$J\_C = A \cdot T_C^2 \cdot \exp\left(-\left(\psi_{\max} - V\right)/kT_C\right) . \tag{126}$$

The dimensionless emitter electron potential energy, γ_E, can then be calculated by the equation

$$\gamma_E = \ln\left(J\_ES / J\_E\right) , \tag{127}$$

where J_ES is the emitter saturation current. Given γ_E, Poisson's equation for the emitter side is then integrated to solve for the emitter-side dimensionless distance, ξ_E. The collector-side dimensionless distance, ξ_C, is related to ξ_E and is given by

$$\xi_C = dgap / x_0 - \xi_E . \tag{128}$$

Given ξ_C, Poisson's equation for the collector side is then integrated to solve for the new estimate of emitter-side dimensionless potential, $\gamma_{C\ new}$.

The values of the initially guessed dimensionless potential, $\gamma_{C\ est}$, is compared to the newly calculated dimensionless potential, $\gamma_{C\ new}$. If the difference is above a user defined tolerance, a new value of $\gamma_{C\ est}$ is chosen, and the procedure is repeated. When the difference is below a user defined tolerance, the procedure is stopped, and a value of γ_C has been determined for the output voltage. The maximum electron potential energy, ψ_{max}, is given by

$$\psi_{\max} = \gamma_C kT_E + \phi_C + V , \tag{129}$$

as shown in Figure 66.

The effective potential barriers and transmission coefficients can then be recalculated. ψ_{max} is calculated again using the procedure described above. This procedure is repeated until the value of ψ_{max} converges.

With ψ_{max}, the emitter and collector current densities, xj_e and xj_c, are calculated by

$$xj\_e = A \cdot T_E^2 \cdot \exp\left(-\psi_{\max} / kT_E\right) \tag{130}$$

and

$$xj\_c = A \cdot T_C^2 \cdot \exp\left(-\left(\psi_{\max} - V\right)/kT_C\right) . \tag{131}$$

Finally, the net current density in the space charge mode, xj_sc_net, is given by

$$xj\_sc\_net = \tau_{spch}\left(xj\_e - \Gamma_{spch} \cdot xj\_c\right). \tag{132}$$

5.10.5 Retarded Mode Subroutine

In the retarded mode, the bias field on the emitter is decelerating in nature, and the bias field on the collector is accelerating. Figure 67 illustrates the interelectrode electron energy potential distribution for the retarded mode of operation. The collector is entering the Schottky mode of operation, and the emitter is operating in a retarded mode. The identities and functions of the emitter and collector are opposite to those in the Schottky mode of operation described in section 5.10.3. In the retarded mode, the collector will emit the greater current density of the two electrodes.

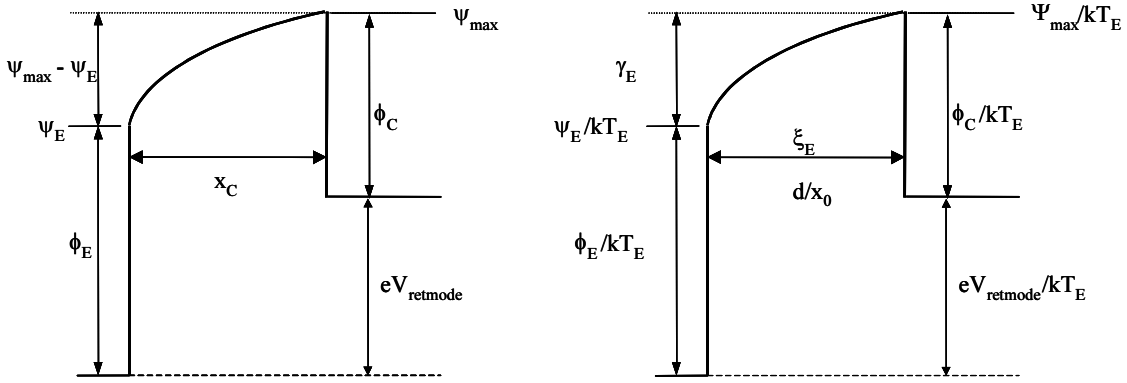

Figure 67. The electron potential energy and dimensionless potential energy for the Retarded mode.

In the main section of the code, the maximum retarded mode voltage, v_retd_max, and the number of retarded mode points, num_retd_reg, are input parameters. The maximum field, e_max, that the emitter will experience during the retarded mode is then

$$e\_max = (v\_retd\_max - v\_cr)/dgap \ . \tag{133}$$

The incremental electric field, del_e, on the collector surface is then the maximum electric field divided by the number of output voltage-current pairs, num_retd_reg, to be calculated in the retarded mode. The electric field, efield_rm, at each retarded mode calculation is then

$$efield\_rm = e\_max - \left(num\_retd\_reg - istep\right) \cdot del\_e \ , \tag{134}$$

where istep is a loop parameter that varies from 1 to num_retd_reg .

If patch conditions exist on the emitter and collector surface, the first calculation performed is to calculate the average emitter and collector work functions as well as the “skyline” barrier (as

described in section 5.8). Then, the transmission coefficients described in Section 5.9 are calculated. Finally, the effective diode transmission coefficient, τ , and the symmetry index, Γ, are calculated. The iterational procedure described above in section 5.10.1 to calculate v_sat is also used to calculate the retarded mode voltage, v_sch_rm.

The collector saturation current, xj_e_rm_sat, is first calculated. The Schottky current from the collector, xj_e_rm_sch, can then be calculated and is given by

$$xj\_e\_rm\_sch = \tau_{rm} \cdot xj\_e\_rm\_sat \cdot \exp\left(3.79x10^{-4}\sqrt{\alpha_S \cdot efield\_rm}\,/\,kT_C\right). \quad (135)$$

The dimensionless gap distance, ξ_E, is related to the Schottky current by

$$\xi_E = 9.186\text{x}10^5 \cdot T_C^{-3/4} \cdot \sqrt{\text{xj\_e\_rm\_sch}} \cdot \text{dgap} \ . \quad (136)$$

Given ξ_E, Poisson's equation is then integrated to solve for the dimensionless voltage, γ_E. The retarded mode voltage, v_sch_rm, can then be calculated using the relationship shown in Figure 67, and is given by

$$\text{v\_sch\_rm} = \phi_E - \phi_C + (kT_E)\gamma_E \ . \quad (137)$$

The back emission from the emitter, xj_c_rm, is given by the Richardson-Dushmann equation

$$xj\_c\_rm = A \cdot T_E^2 \cdot \exp\left(-\left(\phi_E + kT_C\gamma_E\right)/kT_E\right), \quad (138)$$

where the term in the numerator of the exponential represents the potential energy barrier experienced by electrons emitted from the emitter.

Finally, the net current density in the retarded mode, xj_ner_rm, is given by

$$xj\_ner\_rm = \tau_{rm}\left(xj\_e\_rm\_sch - \Gamma_{rm} \cdot xj\_c\_rm\right). \quad (139)$$

5.11 Modeling results

The modeling code described above is now compared with data obtained from two different cathodes.

5.11.1 Data Reduction

Two important physical parameters that must be obtained are the work function of the emitter and collector (ϕ_E and ϕ_C) and the effective Richardson-Dushmann constant (A^*). For this work,

ϕ_E, ϕ_C, and A^* are determined by operating the diode in the forward bias and reverse bias Schottky mode. The Schottky emission current, I, is described by

$$I = a \cdot A \cdot T^2 \cdot \exp[\phi/kT] \cdot \exp\left((e/kT)\sqrt{e\alpha_S V/4\pi\varepsilon_0 d}\right) = I_0 \cdot \exp\left((e/kT)\sqrt{e\alpha_S V/4\pi\varepsilon_0 d}\right), \qquad (140)$$

where A is the Richardson-Dushmann constant, T is the electrode temperature, k is Boltzmann's constant, e is the electron charge, and ε_0 is the permittivity of free space, V is the applied voltage across the gap, a is the emission area, I_0 is the Richardson-Dushmann current, and d is the gap size. Equation 140 can be rearranged to express the natural logarithm of current as a function of the square root of voltage and is given by

$$\ln(I) = \ln(I_0) + \left(\left(e^{3/2}\alpha_S^{1/2}\right)/\left(2kT\sqrt{\pi\varepsilon_0 d}\right)\right)\cdot\sqrt{V}\ . \qquad (141)$$

Equation 141 yields a straight line when the natural logarithm of current is plotted versus the square root of voltage. The y-intercept of equation 141 yields the Richardson-Dushmann current. The slope of the line represented by equation 141 may be used to estimate the interelectrode gap size of the converter diode, d, by solving the term in front of the $\sqrt{\mathrm{V}}$ term for d.

At zero voltage, $I = I_0$ and equation 141 can be rewritten as

$$\ln(I_0) = \ln\left(a \cdot A \cdot T^2 \cdot \exp(-\phi/kT)\right)\ . \qquad (142)$$

Equation 142 can be rearranged to yield

$$\ln\left(\mathrm{I}_0/\mathrm{T}^2\right) = \ln(\mathrm{a}\cdot\mathrm{A}) - \phi/\mathrm{kT}\ . \qquad (143)$$

Two or more values of $\ln\left(\mathrm{I}_0/\mathrm{T}^2\right)$ obtained at different temperatures can be plotted versus $1/\mathrm{T}$ to yield a Richardson plot. The y-intercept, g, of equation 143 is then equal to $\ln(\mathrm{a}\cdot\mathrm{A})$. The Richardson-Dushmann constant, A, is found from

$$A = \exp(g)/a\,. \qquad (144)$$

The slope of the Richardson plot, m, (or equation 143) is $-\phi/k$. The work function, ϕ, is then found by the relation

$$\phi = -\mathrm{mk}\,. \qquad (145)$$

5.11.2 Oxide Cathode Results

Figure 68 illustrates the Schottky plot for typical forward bias diode sweeps. The 550 and 600 ºC plots exhibit linearity beyond 80 Volts, and the 500 ºC plot exhibits linearity beyond an

output voltage of 100 Volts. Figure 69 shows the Richardson plot of the sweep measurements from Figure 68. The Richardson-Dushmann constant and emitter work function calculated are 2.3×10^{-3} A/cm^2/K^2, 1.26 eV and are in fair agreement with the range of work functions and constants reported in the literature. Gap sizes for the emitter were calculated to range from 14.5 to 18.8 microns. The actual gap size was 20 microns.

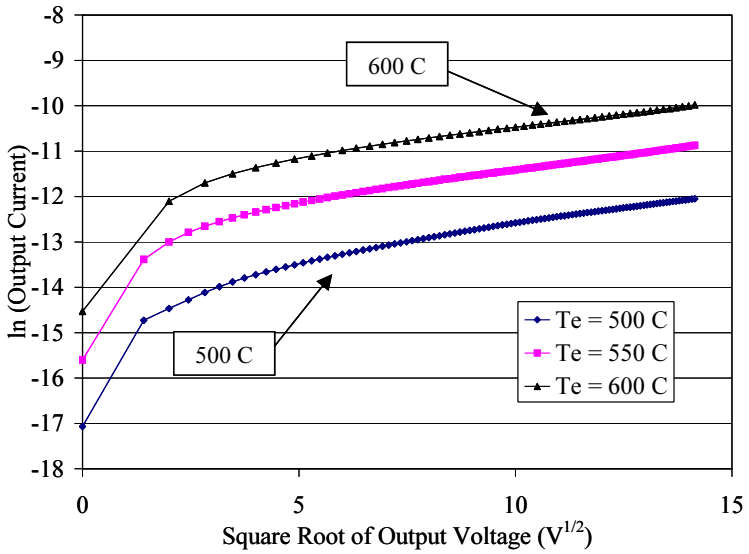

Figure 68. Forward biased Schottky plots at various temperatures.

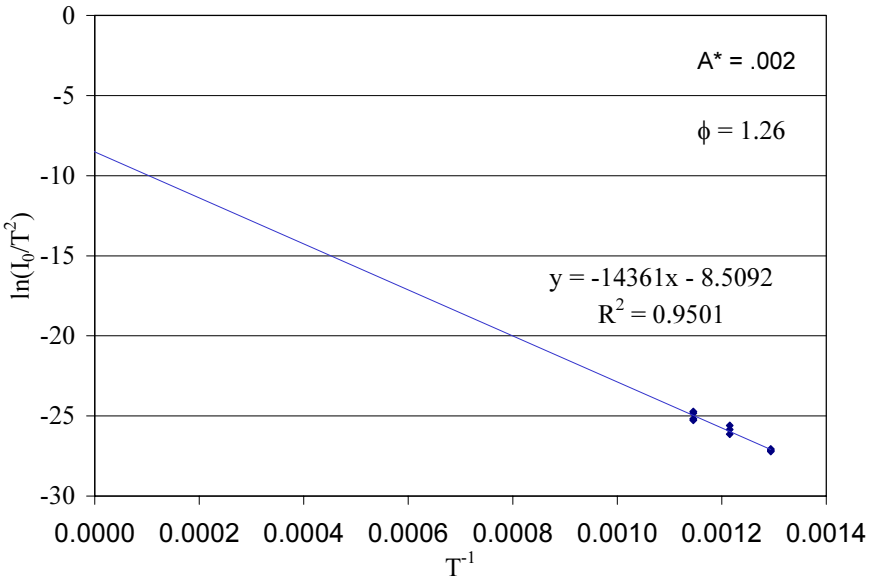

Figure 69. The Richardson plot of the data from Figure 68.

The Schottky emission data primarily supplies information about the low work function patch. Therefore, the work function and effective Richardson-Dushmann constants reported above are those of the low work function patch, and we may write

$$\phi^* = \phi_L \ , \tag{146}$$

where ϕ^* is defined as the Schottky measured value of the electrode work function and ϕ_L is the work function value of the low work function patch. The effective Richardson-Dushmann constant, A^*, can be divided by the Richardson-Dushmann constant, A (A = 120 A/cm^2/K^4), to define an estimate of the area fraction ,F_L, of the low work function patch area to the entire surface area of the electrode

$$F_L = A^* / A \,, \tag{147}$$

or

$$A^* = F_L \cdot A \,. \tag{148}$$

The area fraction of the high work function patch, F_H, is then given by

$$F_H = 1 - F_L \,. \tag{149}$$

The current density measured at zero field (or zero voltage bias on the diode) can then be used to estimate the zero field work function, $\bar{\phi}$, of the patchy surface as given by

$$\bar{\phi} = kT \cdot \ln\left(-AT^2 a / I \right), \tag{150}$$

where I is the current measured at zero field, and a is the surface area of the electrode. The work function value of the high work function patch, ϕ_H, can then be estimated by

$$\phi_H = \left(\bar{\phi} - F_L \phi_L\right) / \left(1 - F_L\right). \tag{151}$$

For the low work function values reported above, the high work function patch value is calculated to be approximately 2.23 eV for the emitter.

Figure 70 illustrates the forward bias (or Schottky mode) comparison of the measured data and the model simulation. The model fits the data well at all voltage values. The patch model assumed two distinct patch sizes with abrupt boundary changes. The nature of patchy surfaces is not well reported or understood, and the patch distribution may well be quite different than that modeled to date. The model predicted patch effect can be quite dramatic in reducing current at low voltage values. For the emitter and collector, the low work function patch size was selected to be 0.55 and 16 microns, respectively. These values were chosen by fitting the model results to the measured data. The high work function patch size was also selected by fitting the model values to the measured data.

Reflection coefficient values are not available for the oxide modeled above. Figure 71 illustrates the reflection coefficient used for modeling.

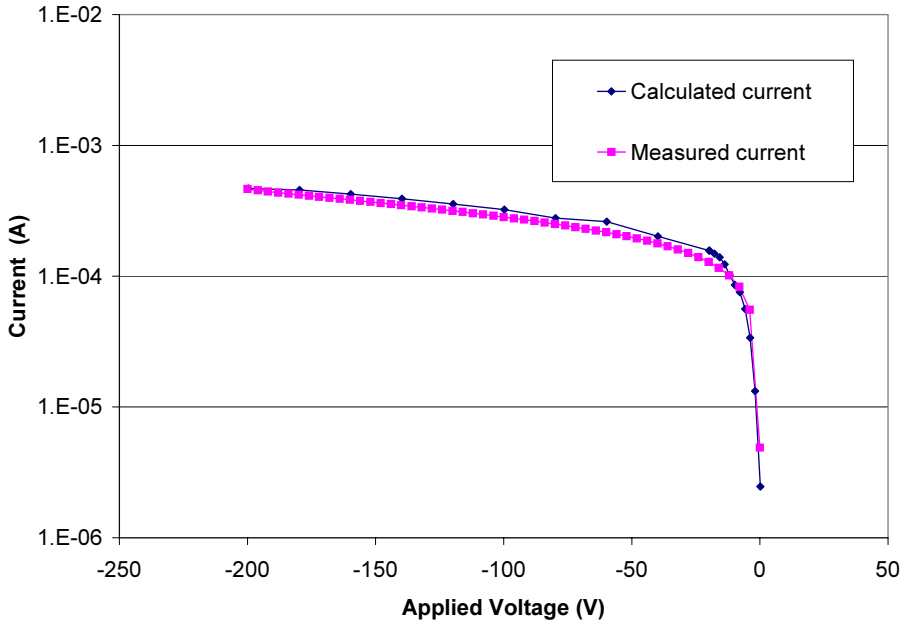

Figure 70. Comparison of modeled diode current-voltage response to measured values.

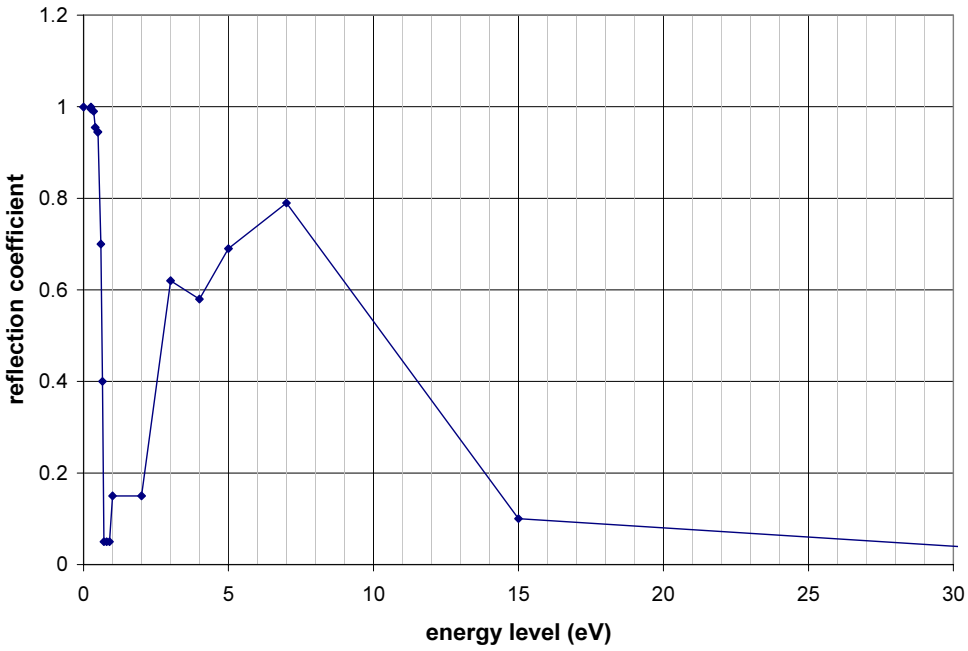

Figure 71. Reflection coefficient data used for the oxide cathode.

5.11.3 Microdispenser results

The measured microdispenser cathode voltage current characteristics are illustrated in Figure 72. The cathode was tested at temperatures ranging from 947 to 1145K. Measurements of these

films show a non-linear trend in the emission current. The nonlinearity tends to be more pronounced at lower temperatures. An example (for T = 1030K) is pictured in Figure 73, also known as the Schottky plot of the emission current. The measurement of the slope indicates that the gap size is approximately 68 microns; in reality, the gap size of the test diode is 100 microns.

Studies have shown that a field applied to the surface of a semiconductor may reduce the work function by an amount, δV_f. The semiconductor has a limited concentration of free electrons compared to a metal, and an external electric field can penetrate into the surface, form a space charge region, and bend the conduction band with respect to the Fermi level. Analysis using Poisson's equation shows that the work function reduction has the form

$$\delta V_F = (2kT/e)\cdot \arcsin h\left[(V/d)\sqrt{b/n_0 T}\right], \tag{152}$$

where n_0 is the free electron density, e is the electron charge, and b is a constant. Equation 152 implies that field incursion becomes more pronounced at low temperatures and low free electron densities. Low temperatures also result in low free electron densities. This effect is observed in the thin film current measurements over a wide variety of temperatures but is most pronounced at low temperatures. The analysis assumes that the metal capping layer of the thin film loses intimate electrical and physical contact with the oxide below it after thermal annealing. This feature would allow field incursion into the lower oxide layers. Figure 73 pictures the modeled emission current after the field incursion effect is removed. The constant, b, is estimated so that the slope of the modeled current indicates a gap size of approximately 100 microns.

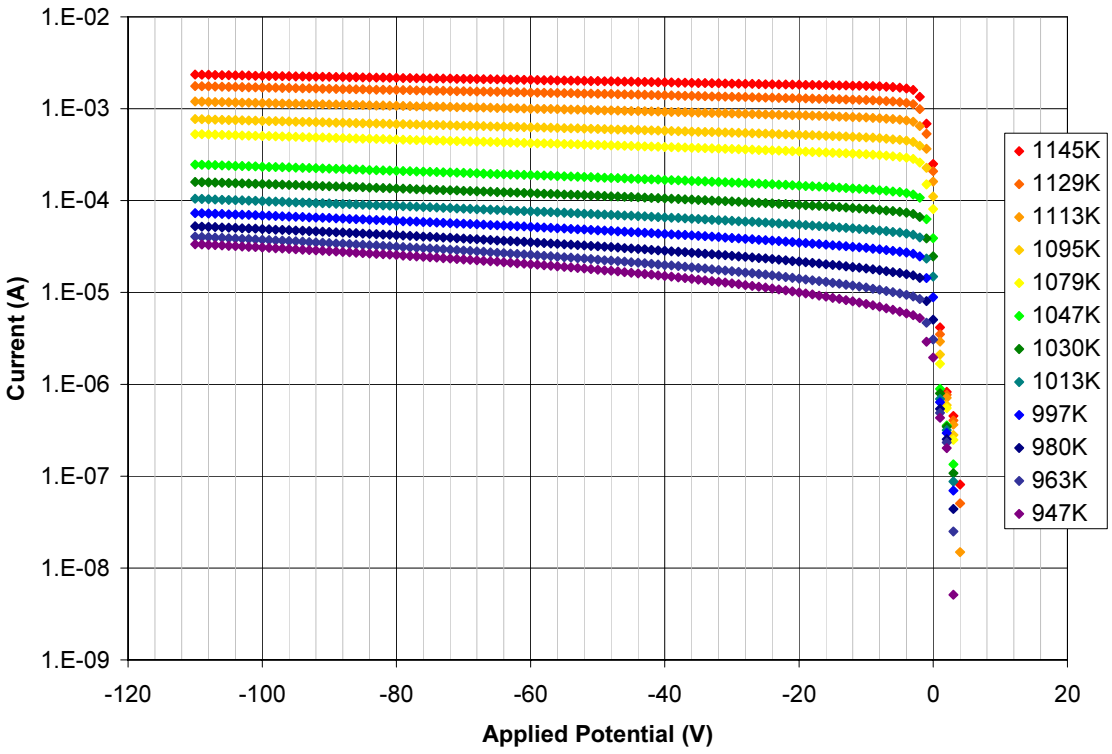

Figure 72. Measured microdispenser cathode voltage current characteristics.

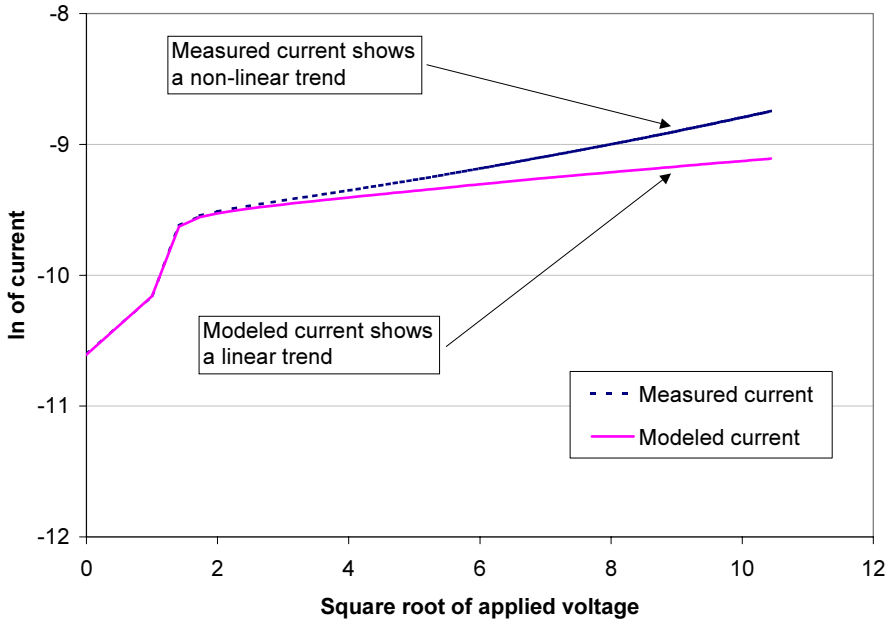

Figure 73. Schottky plot of the emission current.

After all of the currents in Figure 72 are compensated for field penetration, a Richardson plot can be calculated and is shown in Figure 74. The slope yields a work function of approximately 2.2 eV, and the y-intercept yields a Richardson coefficient of 26 $A/cm^2/K^4$.

Figure 75 illustrates the forward bias (or Schottky mode) comparison of the measured data and the model simulation. The model fits the data well at all voltage values. Reflection coefficient concepts and values described in Section 5.9 were used for the modeling parameters. Patch sizes were chosen so that the non-linear portion of the model matched the non-linear portion of the data, and compliance with equations 147 – 150 were met.

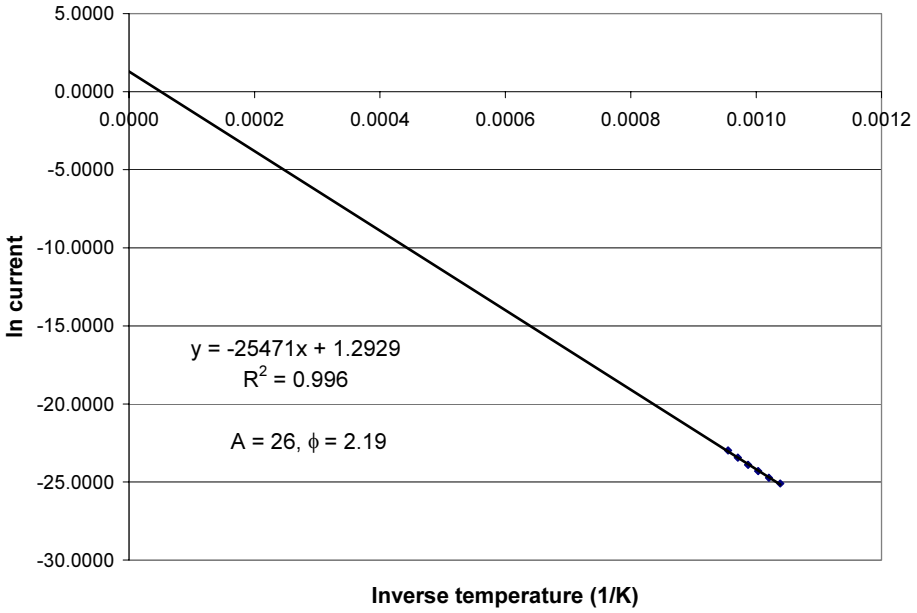

Figure 74. Richardson plot of measured data.

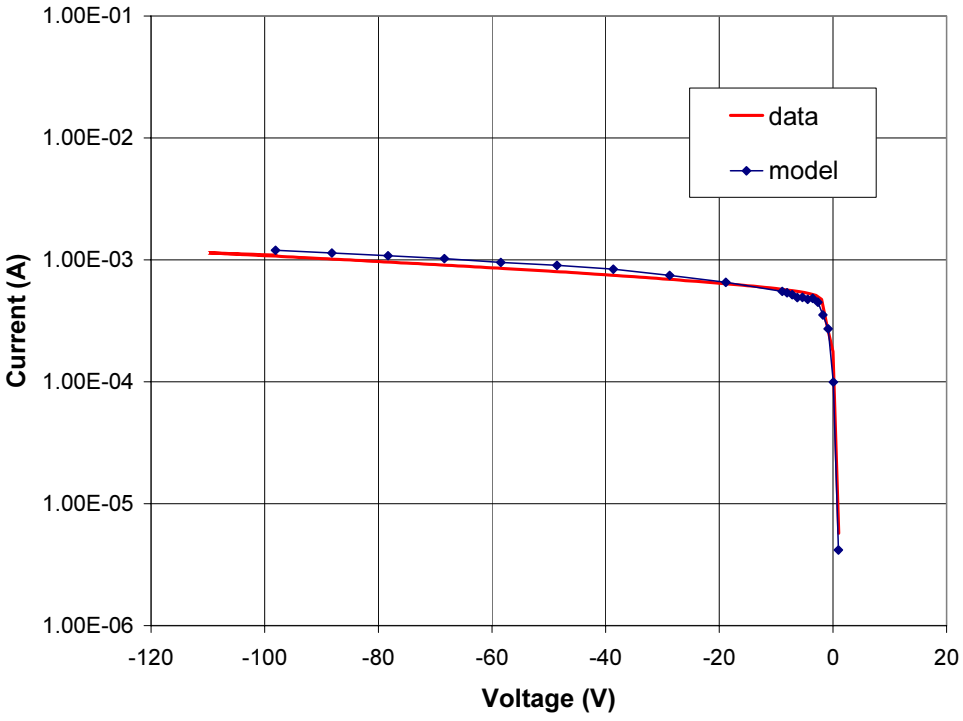

Figure 75. Comparison of modeled mirodispenser diode current-voltage response to measured values

5.12 Modelling Conclusions

Although the model is successful in capturing the MTC current-voltage characteristics, several weaknesses need to be addressed. First, the reflection coefficients for thermionic emission materials of interest for the MTC need to be calculated and measured. Second, the active emission sites need to be optically recorded to determine the patch characteristics of the emitter. Given the reflection coefficients and patch sizes of the emitter, the modeler can calculate the diode characteristics without having to estimate reflection coefficients or patch sizes.

6. References

Baksht, F. G., G. A. Dyuzhev, A. M. Martsinovskiy, B. Ya. Moyzhes, G. Ye. Pikus, E. B. Sonin, and V. G. Yur'yev (1978) Thermionic Converters and Low-Temperature Plasma, L. K. Hansen, ed., DOE-tr-1, Technical Information Center, U.S. Department of Energy.

Balestra, C. L., F. N. Huffman, and C. C. Wang (1978) "Topical report on electron reflection from one-dimensional Barriers," ThermoElectron Corporation Report, TE4237-38-79, Waltham, MA.

Beck, A.H. (1958) *Proc. I.E.E.*, 2750R, 372.

Becker, J. A. (1929) *Phys. Rev.*, **34**, 1323.

Cattelino, M. and G. Miram, (1997) *Appl. Surf. Sci.*,111, 90.

Cortenraad et al. (1999) Appl. Surf. Sci. 146, 69-74

Edison, T. A. (1884) US Patent Specification, No. 307,031, filed Nov. 15, 1883, patented Oct. 21 1884.

Gärtner, G., P. Geittner, H. Lydtin and A. Ritz, (1997) *Appl. Surf. Sci.*,111, 11.

Gurtovoy, M. Y. and Kovalenko, G. I. (1941) A study of the Operation of a Diode in Cesium Vapor, *Fizichni Zapiski,* 9: 240.

Hasker

Hernqvist, K. G. , Kanefsky, M. , and Norman, E. (1958) Thermionic Energy Converter, *RCA Rev.*, 19:244.

Herrmann, G. and S. Wagener (1951) The Oxide Coated Cathode: Volume 1 Manufacture, Chapman & Hall Ltd., London.

Herring, C. and M. H. Nichols (1949) Rev. Mod. Phys. **21**, 185.

Hutson, A. R. (1955) *Phys. Rev.* **33**, 454.

Kettani, M. A. (1970) Direct Energy Conversion, Addison-Wesley Publishing Company, Reading, MA.

King, D. B. (1999), 16th Symposium on Space Nuclear Power and Propulsion, AIP Conference Proceedings #330.

Kniazzeh, A. (1959) Potential Distribution Between Two Parallel Thermionic Emitters with Application to the Thermo Electron Engine, Thesis submitted in Partial Fulfillment of the Requirements for the Degree of Bachelor of Science, MIT.

Kotula, P. G., M.R. Keenan, and J.R. Michael, (2003) *Microsc. Microanal.,* 9, 1.

Langmuir I. (1913) The Effect of Space Charge and Residual Gases on Thermionic Curremts in High Vacuum, *Phys. Rev*., **2**: 450-486.

Magnus, S. H., D.N. Hill, and W.L. Ohlinger, (1997) *Appl. Surf. Sci.*,111, 50.

Marshall, A. C. (1998) Appl. Phys. Lett., 73(16), 2971

Marshall, A. C. (1998) An equation for thermionic currents in vacuum energy conversion diodes, Applied Physics Letters, Vol. **73**, No. 20, pp.2971-2973.

Marshall, A. C. (1999) "Quantum reflection at dipole barrier," internal memo, 1999.

Marshall, A. C. (2000) "An Advanced Thermionic Theory: Recent Developments", *Proc. 17th Symposium on Space Nuclear Power and Propulsion*, M. S. El-Genk and M. D. Hoover, eds., American Institute of Physics, New York, AIP Conference Proc. 504, pp. 1319-1326.

Muller, W. (1997) Appl. Surf. Sci. 111, 1997, 30-34.

Morgulis, N. D. (1947) "The Schottky Effect for Composite Semi-conductor Electron Emitters," Journal of Physics, Vol. XI, No. 1.

Nottingham, W. B. (1960) The Thermionic Diode as a Heat-to-Electrical-Power Transducer, Direct Conversion of Heat to Electricity, J. Kaye and J. A. Welsh (Eds.), pp. 2-1 to 2-16, John Wiley & Sons, Inc., New York.

Raju, R. S. and C. E. Maloney (1994) "Characterization of an Impregnated Scandate Cathode Using a Semiconductor Model," IEEE Transactions on Electron Devices, Vol.41, No. 12, December, pp. 2460-2467.

Rasor, N. S. (1998) "The Importance of Electron Reflection on Thermionic Converter Performance," 33rd Intersociety Energy Conversion Engineering Conference-1998, ANS Conference Proceedings 700262, Colorado Springs, CO. p 211.

Richardson, O. W. (1912) Some Applications of the Electron Theory of Matter, *Phil. Mag.*, 23:594-627.

Schlichter, W. (1915) Die Spontane Electronenemission gluhender Metalle und das gluhelektrische Element, *Ann. Physik*, 47(4):573-640.

Sze, S. M. (1981) Physics of Semiconductor Devices, John Wiley & Sons, New York.

Thomas,R. E., J.W. Gibson, G.A. Haas and R.H. Abrams, (1990) *IEEE Trans. Electr. Dev.*, 37(3), 850.

Wright, D. A. and J. Woods (1952) "The Emission from Oxide-coated Cathodes in an Accelerating Field," Proc. Phys. Soc., Sect. B, Vol. 65, pp 134 - 148.

Zagwijn, P. M., J.W. Frenken, U. van Slooten, and P.A. Duine, (1997) *Appl. Surf. Sci.*,111, 35.

Zavadil, K.R., D.B. King and J.A. Ruffner, (1999) Low Work Function Thermionic Materials, SAND99-2982.

Zavadil, K. R., D.B. King and J.A. Ruffner, (2001) Space Technology and Applications International Forum 2001, M.S. El-Genk, ed., AIP, Vol. 552, 1165-1170.

Zavadil, K.R., J.A. Rufner, and D.B. King, (2003) Low Work Function Materials for Microminiature Energy Conversion and Recover Applications, US Patent 6,563,256B1.

Zollweg, R. J. (1964) Surf. Sci. **2**, 409.

Appendix A:

BaO/W(100) thermionic emitters and the effects of Sc, Y, La, and the density functional used in computations

D. R. Jennison, P. A. Schultz, D. B. King, and K. R. Zavadil
Sandia National Laboratories
Albuquerque, NM 87185-1415

Abstract

Density functional theory is used to predict workfunctions, ϕ. For relaxed clean W(100), the local density approximation (LDA) agrees with experiment better than the newer generalized gradient approximation, probably due to the surface electron self-energy. The large Ba metallic radius indicates it covers W(100) at about 0.5 monolayer (ML). However, Ba^{2+}, O^{2-}, and metallic W all have similar radii. Thus 1 ML of BaO (one BaO unit for each two W atoms) produces minimum strain, indicating commensurate interfaces. BaO(1 ML) and Ba(½ ML) have the *same* ϕ to within 0.02 V, so *at these coverages* reduction or oxidation is not important. Due to greater chemical activity of ScO vs. highly ionic BaO, when mixing the latter with this suboxide of scandia, the overlayer always has BaO as the top layer and ScO as the second layer. The BaO/ScO bilayer has a rocksalt structure, suggesting high stability. In the series BaO/ScO/, BaO/YO/, and BaO/LaO/W(100), the latter has a remarkably low ϕ of 1.3 V (LDA), but 2 ML of rocksalt BaO also has ϕ at 1.3 V. We suggest BaO(1 ML) *does not exist* and that is worthwhile to attempt the direct synthesis and study of BaO(2 ML) and BaO/LaO.

While there are many reasons to understand the workfunctions (ϕ) of technologically relevant materials, little reliable theoretical work has been done. Here we begin with a general fundamental study, finding that an older method achieves better results than a newer one in first-principles calculations. We suggest that this is due to the decades-old neglect of an important factor, namely the surface-electron self-energy. We then begin an initial exploration of systems of high importance, and end with the proposal of a new system that promises usefulness if it can be synthesized.

Of recent interest, microgap thermionic converter (MTC) diodes are an innovative design using advanced electrode materials to convert heat into electricity. The current MTC prototype is a planar, two electrode thermionic vacuum diode. However, commercial electronic integrated circuit (IC) fabrication techniques now allow the MTC to be produced as one unit with micron sized electrode gap features (a micron sized gap between the electrodes plays a key role in obtaining higher energy conversion efficiencies). In addition, the IC fabrication technique allows thousands of MTCs to be fabricated as one large conversion unit. This scale of fabrication may allow various MTC units to be fabricated with power outputs ranging from milliwatts to hundreds of watts and at very low cost.

Low work function emitter materials that are compatible with the electronic fabrication techniques have been developed. Work is also in progress to produce different materials with low but different work functions. The use of variable work function electrodes would allow the creation of MTCs tailored to function efficiently for several heat sources and their remarkably low (550-1000 C) temperature regimes. In summary, the successful use of MTCs with small electrode spacing and variable electrode work functions would allow: 1) the conversion of heat energy to relatively large electrical power densities (up to 10s of W/cm^2) at relatively high conversion efficiencies (up to 25%), and 2) operation of converters tailored to function for the different heat sources and their temperature regimes. The heat required for this direct conversion process is fuel independent; any heat source (combustion, solar, advanced nuclear reactors, radioisotopes, waste heat) can be used. Possible applications include micro-robotics, space-based power, mobile and remote electrical power sources, and commercial power production.

While there has been significant progress in MTC development, the electrode materials are not well understood and the electrode thermionic properties are highly sensitive to manufacturing processes. Advanced theoretical and modeling capabilities are required to achieve optimum performance for MTC diodes.

Traditional low temperature emitters are based on stabilized barium strontium oxide (BSCO ≡ 47.5% Ba, 47.5% Sr and 5% Ca) [1]. Saito, *et al*. have shown that depositing a capping layer of scandia (Sc_2O_3) improves the longevity of traditional BSCO emitters, which can be exposed to accelerated impacting positive ions from electron stimulated desorption processes at the collector [2]. The role of scandia has been recognized for some time in higher operating temperature tungsten based dispenser cathodes [3]. The primary problem with BSCO films is that deposition from carbonate precursors is required with a subsequent activation stage that releases CO_2, trapped H_2O, and suboxides. This activation process is responsible for producing the emitting oxide, which has a very low activation energy for free Ba production and is easily "poisoned" by subsequent atmospheric exposure. As a result, activation must be conducted in the diode environment, which results in the production of high levels of condensable gases. We have found [4] that the adsorption of these gases onto the internal surface area of the diode produces unacceptable values of leakage current between the emitter and collector.

The electron source community has optimized *macroscopic* dispenser cathodes based on impregnating a porous tungsten matrix with barium oxide for display applications [1]. Their thin film work has been limited to modification of these macrostructures to improve cathode lifetime [5, 3].

Barium is the oxide material of choice in thermionic cathodes. Extensive work by the vacuum tube and electron gun communities established the role of Ba in macroscopic emitter structures [6].
Ba has been viewed as an adsorbate that lowers the surface work function through the formation of a surface dipole. While obvious for Ba metal, it is not clear whether this is true for an overlayer of highly ionic BaO, where the nearest-neighbor dipoles oppose each other. BaO would be produced in any but the highest vacuum applications. Below we provide theoretical evidence that the simplistic argument is vacuous in that both Ba and BaO single layers on

W(100) have essentially the same ϕ, and that lower workfunctions are only produced by BaO(2ML), which may be the stable structure.

In the porous diodes, a life cycle for Ba exists that starts with localized reduction to produce free Ba from the host oxide, diffusion of free Ba through the bulk emitter, surface diffusion of Ba usually accompanied by oxidation, and eventual desorption and loss. The classic barium-strontium-calcium oxide (BaSrCaO), used in the tube industry and formed from the carbonates, retains considerable carbon in the annealed matrix to act as the local reductant, thus permitting facile Ba (vs. BaO) diffusion. These films contain ntrinsic porosity and it is assumed that this porosity aids in Ba surface transport vs. bulk transport. The electron source community has settled on porous W forms that are impregnated with a $BaCO_3$, $CaCO_3$ and Al_2O_3 mixture at elevated temperature in hydrogen or vacuum. The W structure acts as a support, an internal electron conductor, and supplies a large interfacial area for Ba reduction. This latter design cannot be used to produce thin films, although the concepts can be incorporated into a thin film structure.

In summary, emitters of high interest have metallic Ba or BaO at the surface. Because of lattice matching requirements, the latter is the most commensurate with a W(100) substrate. As mentioned, it has been found that a mixed BaO and scandia emitter is also of interest [1-3]. However, the detailed atomic structure of this surface is unknown and the saturated oxide Sc_2O_3 may simply play the role of protecting underlying BaO from ion bombardment. For vacuum tube devices biased at 100s - 1000s V, the electrons are energetic when they hit the anode and positive-ion electron stimulated desorption (ESD) occurs — this damages the cathode material layer as these ions are accelerated into it. However, for a thermionic converter biased at ~ 1 V, this effect would not be an issue because ion ESD thresholds are always > 10 eV. In such cases, Ba replenishment from a porous substrate is not necessary.

Steric arguments based on commensurability likely ensure a Sc_2O_3/BaO/W(100) layered geometry. It is also possible that a tripole chain of Sc-O-Ba may further lower the workfunction. Due to uncertainties in geometry, this issue we shall leave for the future.

In this Letter, using first principles density functional theory (DFT) [7] we first explore clean W(100). Surprisingly, we discover that the older local density approximation (LDA) [8] predicts a ϕ of 4.4 V. This is much closer to the nominal experimental value of 4.5 V than the newer generalized gradient approximation (GGA) [9]. Here the Perdew-Burke-Ernzerhof (PBE) form [10] yielded ϕ = 3.8 V (computational details described below). A similar situation was recently reported for surface energies where LDA is a bit low but matches experiment much more closely than the nominally better GGA [9]. The error was traced to an accidental cancellation of errors related to surface-electron self-exchange and self-correlation. While an approximate correction was found that when applied brought *both* LDA and GGA into agreement with experiment [11], the correction is not yet automatically and accurately available computationally. Thus in what follows, we used only LDA.

We then studied both metallic Ba and BaO on W(100). Because of the large metallic radius of Ba (2.22 Å), only about ½ ML can be accommodated, making a c(2x2) LEED pattern, as reported [12]. However, Ba^{2+}, O^{2-}, and metallic W all have about the same radii, 1.35 Å, 1.40 Å, and 1.41 Å, respectively. Thus a commensurate overlayer of one BaO unit for each two W atoms is likely to exist over large areas. Surprisingly, we found both Ba(½ ML) and BaO(1 ML) have the *same* ϕ. Thus reduction and oxidation of Ba is not an issue at these coverages, except for transport out of the porous substrate.

After exploring this system, we turned to the baria/scandia overlayers on W(100) with a suboxide of Sc. The reasons are both for fundamental understanding and because some applications, such as actively pumped klystron tubes, have non-oxidizing environments in which a suboxide can exist. Many geometries were tried including BaO/ScO/, ScO/BaO, and mixed layers. From the total LDA energies, it was easily determined that the system preferred BaO as the top layer with ScO as the second and in contact with both BaO above and W(100) below. This is very logical and has been suggested by experiment[12], as the energy is lowered both by the electrostatic interactions of ScO with the highly ionic BaO and also at the interface with W(100). At this interface, adhesion comes from both metal polarization, the dominant way saturated oxides bind to metals [11, 13], but also from covalency since Sc is not fully ionized. Furthermore, it was found that the rocksalt structure is favored for the oxide bilayer, thus suggesting high stability by having interlocking Madelung potentials.
Noting the interesting structure of the system and the possibility of synthesis, we then examined how proceeding lower in the periodic table would affect ϕ, i.e. going from Sc to Y to La. A dramatic drop was found, ending in only ϕ = 1.3 V. This motivates an attempt to synthesize this new surface structure on W(100). However, we ended the study with a rocksalt bilayer of BaO, which should be even easier to make. Surprisingly, here ϕ = 1.3 V also, suggesting that those cathodes covered with BaO and which indicate very low workfunctions likely are or have islands of bilayers. Because of the rocksalt structure, we suggest these are more stable than 1 ML and that the latter does not exist.

The slab DFT calculations used the local-orbital basis pseudopotential code SeqQuest [14]. This code automatically sets the vacuum energy to zero so the computed Fermi level is directly related to same [15]. The code is capable of both LDA [8] and GGA [9] calculations. Here the PBE [10] variety of GGA was used. Pseudopotentials used the standard norm-conserving variety of both Hamann [16] (for the metals) and Troullier-Martins [17] (for O) type and used high quality (double-zeta or better) contracted Gaussian basis sets. For more information on the code and its availability, see Ref. [18].

All slab calculations, clean W and with overlayers, were symmetric on both surfaces thereby eliminating any net dipole. For the clean surface, nine bcc W layers were used with a single atom per layer. This small unit cell necessitated a 12x12x1 ***k***-point grid resulting in 36 points in the irreducible wedge of the Brillouin zone (the code uses full cell symmetry). Because of the thickness of the slab, all layers were allowed to relax but only the top two (relaxing -2.5% and +0.6%, respectively) differed significantly in layer spacing from the bulk lattice geometry of LDA (a_0 = 3.088 Å) or PBE (3.171 Å), computed during the construction of the pseudopotentials [18].

Because ϕ is extremely sensitive to the details of the asymptotic behavior of the valence wavefunctions into the vacuum (details which have no appreciable effect on things such as total energy or eigenvalues), floating s and p Gaussian orbitals were added. These were placed at locations above the surface that would have been occupied by the next layer of atoms. This addition to basis set completeness changed the ϕ results significantly, by about + 0.3 V, and moved the computed values towards the nominal experimental numbers. Because of this sensitivity, the computational error bars on predicted ϕ's should be taken as ± 0.1 V.

For the overlayer calculations, four W atoms per layer were needed. This supercell was reduced from 9 to 7 layers of W and the ***k***-point mesh to 6x6x1, resulting in 9 points. The larger cell size and the small surface relaxation of W(100) makes this change acceptable.
Because mixed oxide/metal systems often display both hard and very soft vibrational modes, geometric relaxation must sometimes be done carefully, especially with open oxides such as alumina [13]. Here, however, due to the close packed nature of the systems, relaxation was rapid. A steepest descent algorithm used the computed forces and the "fully relaxed" geometries had all residual forces < 0.03 eV/Å. Upon the seven layer W slab, Ba was placed at ¼ and ½ ML, BaO with one unit cell per two W atoms, and mixed BaO and ScO overlayers in various arrangements. As noted above, by a wide margin the preferred BaO/ScO/W(100) structure had the oxide film in a rocksalt structure and the ScO in the hollows of the W(100) (see Fig. 1). The results for these systems may be found in Table I.
These conclusions have experimental support. Indeed, the recent work of Zagwijn, *et al.* [12] using medium energy ion scattering (MEIS) found evidence of barium on top of ScO_x/W(100), although the oxygen density indicated the sample was somewhat reduced. However, two recent papers by Gartner, *et al.* have also provided evidence that Ba sits above ScO_x/W(100) [19, 20]. Naturally the degree of O saturation depends on oxygen availability, kinetics, and possible removal by ion impact. However, a more recent paper does not mention these conclusions [21].
Because of the stable rocksalt structure of the bilayer oxide BaO/ScO/W(100), as mentioned BaO/YO/W(100) and BaO/LaO/W(100) were also studied. The remarkable ϕ results are also shown in Table I, and details of the structure are contained in Fig. 1. The result for BaO/LaO/W(100) is not due to LaO alone, as LaO/W(100) has ϕ = 1.6 V.
Finally, as mentioned above and in Table 1, the rocksalt bilayer of 2 ML of BaO also has a very low LDA workfunction and one close to some that have been measured, suggesting this is the actual surface structure in the low ϕ surface areas.

These results indicate that it is indeed worthwhile to attempt a controlled synthesis and characterization of BaO/BaO/ and BaO/LaO/W(100) systems. While the former should be easy (deposit 2 ML of Ba, oxidize and anneal), the latter could be difficult. Because the Sc, Y, and La containing layers are all suboxides, it is possible that one cannot oxidize in steps, as a saturated oxide of these metals could have a significant kinetic barrier to reduction by Ba. However, reduction and finding the favored structure could occur upon annealing. A likely route would be to co-deposit ½ ML each of Ba and, say, La and then expose the surface to an oxygen plasma, followed by a final anneal. Other methods might also succeed.

The structure of the more complex oxide surfaces mentioned in the introduction, such as BSCO, are beyond the scope of this paper as their geometry is unknown. However, using established ionic radii, an attempt could be made to compute a Sc_2O_3/BaO/W(100) system. To understand these remarkable results and the failure of a simple dipole explanation, a further detailed theoretical analysis is indicated, including a study of the charge densities and local densities of states of the near surface atoms.

References

R. E. Thomas, J.W. Gibson, G.A. Haas and R.H. Abrams, IEEE Trans. Electr. Dev. **37** (1990) 850.
M. Saito, R. Suzuki, K. Fukuyama, K. Wantanabe, K. Sano, and H. Nakanishi,
IEEE Trans. Electron Dev. **37** (1990) 2605.

3. G. P. Gärtner, H. Giettner, H. Lydtin and A. Ritz, Appl. Surf. Sci. **111** (1997) 11.
4. K. R. Zavadil and D. B. King, to be published.

5. J. W. Gibson, G.A. Haas and R.E. Thomas, IEEE Trans. Electr. Dev. **36**, (1989) 209.

6. A. H. Beck, Proc. I.E.E. **106(B)** (1958) 372.

7. P. Hohenberg and W. Kohn, Phys. Rev. **136** (1964) B864; W. Kohn and L. J. Sham, Phys. Rev. **140** (1965) A1133.

8. J. Perdew and A. Zunger, Phys. Rev. B **23** (1981) 5048; D. M. Ceperley and B. J. Alder, Phys. Rev. Lett. **45** (1980) 566.

9. J. P. Perdew et al., Phys. Rev. B 46 (1992) 6671.

10. J. P. Perdew, K. Burke, and M. Ernzerhof, Phys. Rev. Letts. **77** (1996) 3865.

11. A. E. Mattsson and D. R. Jennison, Surf. Sci. **520** (2002) 611.

12. A. Bogicevic and D. R. Jennison, Phys. Rev. Letts. **82** (1999) 4050.

13. P.A. Schultz, unpublished; for a description of the method see P.J. Feibelman, Phys. Rev. B 35, 2626 (1987).

14. P.A. Schultz, Phys. Rev. B **60** (1999) 1551.

15. D. R. Hamann, Phys. Rev. B 40, 2980 (1989).

16. N. Troullier and J. L. Martins, Phys. Rev. B 43, 1993 (1991).

17. The SeqQuest home page is at www.cs.sandia.gov/~paschul/Quest/.

18. P.M. Zagwijn, J.W. M. Freken, U. van Slooten, and P.A. Duine, Appl. Surf. Sci. **11** (1997) 35.

19. G. Gartner, P. Geittner, D. Raasch and D.U. Wiechert, Appl. Surf. Sci. **146** (1999) 22.

20. G. Gartner, P. Geittner, D. Raasch, A. Ritz and D.U. Wiechert, Appl. Surf. Sci. 146 (1999) 12.

21. R. Cortenraad, A.W. Denier van der Gon, H.H. Brongersma, G. Gartner, D. Raasch, and A. Manenschijn, J. Appl. Phys. **89** (2001) 4354.

Table I

Workfunctions (ϕ) computed for a variety of surface layers on W(100) using LDA. Details are contained in the text.

System:	Ba(¼ML)	Ba(½ML)	BaO(1ML)	BaO/ScO	BaO/YO	BaO/LaO
ϕ (V):	1.68	1.72	1.70	2.40	1.73	1.25

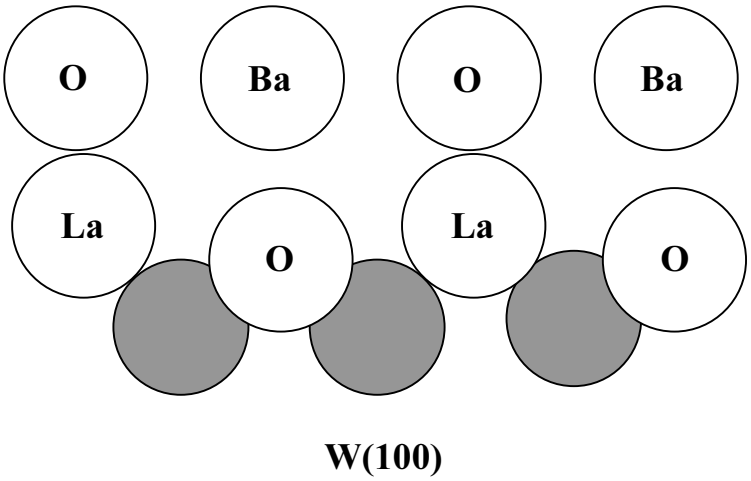

Figure 1 – A schematic drawing of a bi-oxide overlayer of W(100) that may have unusual stability. It is illustrated for the lowest workfunction material, BaO/LaO/, although ScO and YO produce the same structures. The LaO layer is substantially buckled, by 1.86 Å with La higher, with respect to W(100). The later is affected by the overlayers by a small buckling (maximal deviation 0.12 Å), but due to the attraction to the LaO the entire W surface layer relaxes outward with respect to bulk termination by 6% (vs. 2.5% inward for the clean surface). The BaO layer on top is always effectively planar (buckled 0.005 Å, with O lower). The YO and ScO materials relax and buckle quite similarly.

Distribution:

10	MS1136	Donald B. King	6872
2	MS0888	Kevin R. Zavadil	1832
2	MS1415	Dwight R. Jennison	1114
2	MS1411	Corbett C. Battaile	1834
1	MS9018	Central Technical File	8945-1
2	MS0899	Technical Library	9616
1	MS0188	D. Chavez, LDRD Office	1030